

## Chapter 3

# Scattering from a Large Transparent Sphere Based on Maxwell's Equations: Mie Scattering Theory

### 3.1 Introduction

We consider here Mie scattering theory. Incident electromagnetic waves are reflected from and refracted by a large, transparent sphere of uniform refractivity  $N$ , which is slightly different from the uniform refractivity of the surrounding medium. The ratio of the radius of the sphere to the wavelength of the incident waves,  $r_o / \lambda$ , is assumed to be sufficiently large so that certain asymptotic solutions to the Helmholtz equation are applicable. The refractivity difference across the boundary of the sphere is assumed to be sufficiently small (for our case,  $N \ll 0.001$ ). Therefore, the difference in the reflection coefficients from the Fresnel formulas for incident waves with in-plane polarization and with cross-plane polarization is negligible; for grazing conditions, this difference is of the order  $N$ .

In Fig. 3-1, an electromagnetic wave is characterized by its Poynting vector, which in Gaussian units is given by  $\mathbf{S} = c(\mathbf{E} \times \mathbf{H}) / 4\pi$ , where  $\mathbf{E}$  and  $\mathbf{H}$  are, respectively, the electric and magnetic field vectors of the wave. Here  $c$  is the velocity of light in a vacuum. The incoming plane waves and the scattered waves are characterized by  $\mathbf{S}^{(i)}$  and  $\mathbf{S}^{(s)}$ , respectively.  $\mathbf{S}$  provides the power of the wave passing through a perpendicular unit area. The scattered waves are assumed to include both reflected and refracted waves. The incoming wave is assumed to be planar and harmonic. In this case, the electric field may be written as  $\mathbf{E} = \hat{\mathbf{x}}E_o \exp[i(nkz - \omega t)]$ , where  $\hat{\mathbf{x}}$  is a unit vector directed in-plane

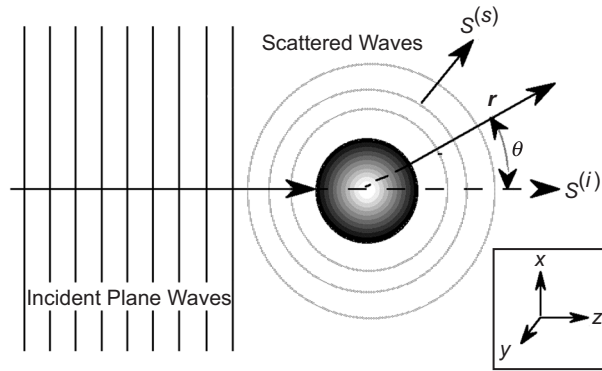


Fig. 3-1. Scattering of incident plane waves from a large refracting sphere.

and perpendicular to  $S^{(i)}$  (see inset in Fig. 3-1). Here  $k = 2\pi / \lambda = \omega / c$  is the wavenumber in a vacuum, where  $\omega$  is the angular frequency of the wave. The index of refraction in Gaussian units is given by  $n = \sqrt{\epsilon\mu}$ , where  $\epsilon$  is the permittivity (or dielectric coefficient) of the medium (assumed to be linear) and  $\mu$  is its magnetic permeability. In a vacuum,  $\epsilon = \mu = 1$ . We will assume a purely dielectric medium with zero charge and no current density throughout the medium. Also, we will assume zero magnetization, so that  $\mu = 1$  throughout the medium. Only  $\epsilon$  will change discontinuously by a small amount across the boundary of the sphere, and here it will be assumed to be otherwise invariant with  $n = 1$  in the surrounding medium and  $n = 1 + N$  inside. We will be interested in the amplitude and phase of the total electric field vector  $\mathbf{E}^{(i)} + \mathbf{E}^{(S)}$  in the vicinity of the low Earth orbiting (LEO) spacecraft.

Scattering from a conducting or a dielectric sphere is widely discussed in the classical electrodynamics literature [1–8]. Much of the material presented here is almost a hundred years old and has been discussed extensively in the past. We mostly follow the Mie formulation given in [8] in the ensuing discussion. This latter reference does not, however, deal with refracted and internally reflected components of scattered waves including rainbow caustics, nor with computational techniques and asymptotic forms. We have supplemented from other sources, mostly cited above, or from our own invention from time to time.

If much of the material in this chapter does involve old ground plowed over many times, why discuss it all? The mathematics of Mie scattering is surely ponderous, and its many asymptotic expansions are complicated, although computationally essential. Several considerations favor including the material. A principal goal here is to establish the mathematical infrastructure that is used in Chapter 5, which deals with discontinuities in the refraction model across a

spherical surface that is embedded in a refracting medium possessing a significant gradient. There, all of the Mie scattering apparatus is needed. Concepts from the “simpler,” pure Mie scattering problem, such as the spectral representation in basic wave theory, the formalism for representing incoming and outgoing spherical waves, the reflection and transmission spectral coefficients, asymptotic expansions, phasor representation, stationary-phase concepts, caustics, etc., all apply to the more difficult problem of an embedded discontinuity in a refracting medium.

A second motivation for the material presented in this chapter stems from the particular emphasis throughout this monograph on stationary-phase concepts. The stationary-phase technique is well known. It is often used to evaluate an integral along the real axis with an integrand comprised of a variable phasor multiplied by a relatively slowly varying real factor. It also is very useful as an aid to other integration techniques by identifying stationary or near-stationary-phase neighborhoods of the integration variable that provide the principal contributions to the integral. But stationary-phase concepts have a much broader relevance. Geometric optics is based on a second-order stationary-phase methodology applied to the phase delay integral along the ray path. The impact parameter associated with a given ray in fact provides a stationary value of the phase delay integral for that ray. In wave theory, the spectral integral representation of a wave involves a certain phasor generated from the scattering coefficients and related geometric delays. The spectral number providing a stationary value for that phasor shows a close correspondence to impact parameter in geometric optics. In fact, one can establish a duality between certain wave theoretic quantities evaluated at stationary-phase points in spectral number and their analogous concepts in geometric optics. Hence, Chapter 3 devotes considerable attention to developing a phasor-based spectral representation for wave theory that is applicable to real spectral numbers, and to developing this stationary-phase duality with geometric optics that was just mentioned. All of these concepts carry over to Chapter 5. Lest the classical approaches for evaluating scattering integrals be completely overlooked, this chapter and also Appendix G discuss briefly the use of the complex spectral number technique. There, a summation over spectral number on the real axis is transformed into a summation of residues from a related contour integral in the complex spectral number plane, which may result in a more rapid convergence of the summation.

A third motivation for the material in this chapter stems from the desire to assess the efficacy of the technique of using scalar diffraction theory applied to the thin phase screen model. The focus here is on the calculation of the LEO-observed scattered field from rays at nearly grazing conditions with the sphere. One of our tasks is to compare the scattering at nearly grazing angles from this sphere based on a solution to Maxwell’s equations with that predicted by the thin-screen technique. Specifically, we will compare Mie scattering results in

this chapter and modified Mie scattering results in Chapter 5 with Fresnel-diffracted wave forms obtained from applying scalar diffraction theory to a thin phase screen model. The thin-screen model serves as a proxy for the refracting/reflecting sphere, and it is defined in Chapter 2, Eqs. (2.5-1), (2.8-2), and (2.8-3). The thin-screen methodology is less complex than Mie scattering theory, and it offers a considerable computational advantage if its soundness can be established. When thin atmosphere conditions apply or, more specifically, when thin-screen caustics are avoided, the agreement between these two systems in LEO-observed phase and amplitude is good.

A fourth motivation is actually related to the first. Chapter 6 discusses the inverse problem of recovering the profile for the index of refraction from the phase and amplitude observations made by the LEO. For that purpose, we use the phasor-based spectral representation of the wave developed in Chapter 5.

To develop a wave theory approach to scattering, we use the general spectral series solutions to the Helmholtz equation for an electromagnetic field to develop the appropriate representations for incoming and outgoing waves and for reflected and transmitted waves. These are addressed in the next sections. We then consider the reflection and transmission coefficients across a planar dielectric surface based on geometric optics and the Fresnel formulas. Next we develop the analogous wave theory spectral coefficients for incident and scattered waves from a refracting sphere and the associated spectral series representations for waves transmitted through the sphere and reflected by it, which is Mie scattering theory. The problem of slow convergence of these spectral series for the scattered and transmitted waves from a large sphere ( $r_o \gg \lambda$ ) is reviewed. The asymptotic expressions for large spectral number and radial coordinate values needed for numerical evaluation are reviewed. Then we develop a phasor-based approach for solving these asymptotic spectral series aided by the stationary-phase technique. Along the way, we compare various stationary-phase concepts from wave theory with those from geometric optics and scalar diffraction theory. Numerical results based on Mie scattering theory for the phase and amplitude of a wave scattered from a large refracting sphere are presented and compared with results obtained from applying scalar diffraction theory to the thin phase screen model. Rainbows and caustics are addressed, and special limiting cases, such as scattering from a perfectly reflecting sphere and from an absorbing sphere, are discussed.

### 3.2 Scalar Potentials

For a harmonic wave in a homogeneous medium without charge and current densities, Maxwell's vector field equations for the time-independent part of the wave are given by

$$\left. \begin{aligned} \nabla \times \mathbf{E} &= ik\mu\mathbf{H} \\ \nabla \cdot \mathbf{E} &= 0 \\ \nabla \times \mathbf{H} &= -ik\epsilon\mathbf{E} \\ \nabla \cdot \mathbf{H} &= 0 \end{aligned} \right\} \quad (3.2-1a)$$

By forming  $\nabla \times (\nabla \times \mathbf{E})$  and  $\nabla \times (\nabla \times \mathbf{H})$ , and noting the identity  $\nabla \times (\nabla \times \mathbf{A}) = \nabla(\nabla \cdot \mathbf{A}) - \nabla^2 \mathbf{A}$ , Maxwell's equations can be converted into a pair of Helmholtz equations:

$$\left. \begin{aligned} \nabla^2 \mathbf{E} + \mu\epsilon k^2 \mathbf{E} &= 0 \\ \nabla^2 \mathbf{H} + \mu\epsilon k^2 \mathbf{H} &= 0 \end{aligned} \right\} \quad (3.2-1b)$$

The vector solutions to these electromagnetic field equations also can be obtained from a pair of linearly independent scalar solutions to the Helmholtz equation,

$$\nabla^2 \Pi + \mu\epsilon k^2 \Pi = 0 \quad (3.2-1c)$$

These scalar potential functions are denoted by  ${}^e\Pi(r, \theta, \phi)$  and  ${}^m\Pi(r, \theta, \phi)$ . Here  ${}^e\Pi$  and  ${}^m\Pi$  are the so-called "electric" and "magnetic" scalar potentials, respectively. The time-independent components,  $\mathbf{E}$  and  $\mathbf{H}$ , are obtained from vector calculus operations on a vector form ( $\Pi\mathbf{r}$ ) of these scalar potentials (due to Hertz). The field vectors are given by [8]

$$\left. \begin{aligned} \mathbf{E} &= \nabla \times \nabla \times ({}^e\Pi\mathbf{r}) + ik\mu\nabla \times ({}^m\Pi\mathbf{r}) \\ \mathbf{H} &= \nabla \times \nabla \times ({}^m\Pi\mathbf{r}) - ik\epsilon\nabla \times ({}^e\Pi\mathbf{r}) \end{aligned} \right\} \quad (3.2-2)$$

If one forms the curl and divergence of  $\mathbf{E}$  and  $\mathbf{H}$  as these fields are defined by Eq. (3.2-2), it may be shown using Eq. (3.2-1c) that these scalar potentials do indeed generate vector fields that satisfy Maxwell's equations for a harmonic wave, that is, Eq. (3.2-1a).

In our problem, these two scalar potentials essentially account for the two possible linear polarization modes of the electromagnetic field. Note that the vector  $\nabla \times (\Pi\mathbf{r})$  is orthogonal to  $\mathbf{r}$ , whereas in general  $\nabla \times \nabla \times (\Pi\mathbf{r})$  is not. Thus, the term  $-ik\epsilon\nabla \times ({}^e\Pi\mathbf{r})$  in Eq. (3.2-2) generates a magnetic field without a radial component, that is, a transverse magnetic field. Similarly,  $ik\mu\nabla \times ({}^m\Pi\mathbf{r})$  generates a transverse electric field. When the electromagnetic field is invariant in the cross-plane direction (along the y-axis in Fig. 3-1), that is, when  $\nabla\Pi \cdot \hat{\mathbf{y}} \equiv 0$ , the curl operation  $\nabla \times ({}^m\Pi\mathbf{r})$  generates the cross-plane

component of the field  $\mathbf{E}_\perp$ , and  $\nabla \times \nabla \times (\epsilon \Pi \mathbf{r})$  generates the in-plane component  $\mathbf{E}_\parallel$ .

The symmetry in Eqs. (3.2-1) and (3.2-2) for  $\mathbf{E}$  and  $\mathbf{H}$  should be noted. It is rooted in the space-time four-vector covariant form that Maxwell's equations take in the framework of Special Relativity. We have chosen Gaussian units to emphasize this point. Note that Maxwell's equations remain invariant when  $\mathbf{E}$  and  $-\mathbf{H}$ , and simultaneously  $\mu$  and  $\epsilon$ , are exchanged. With this symmetry we need deal with only one polarization mode. For example, if we know  $\mathbf{E}$  and  $\mathbf{H}$  for one mode, their forms for the other mode follow directly.

For plane waves in a homogeneous medium,  $H\sqrt{\mu} = E\sqrt{\epsilon}$ . Also,  $\mathbf{H}$  and  $\mathbf{E}$  are orthogonal and in-phase. We take the polar axis of the sphere  $\hat{z}$  to be directed parallel to the direction of propagation of the incident plane wave, that is, parallel to  $\mathbf{S}^{(i)}$  in Fig. 3-1. We choose the azimuthal orientation of our coordinate frame about the z-axis so that the in-plane polarization of the incident wave lies in the plane defined by  $\phi = 0$ .

### 3.2.1 Series Expansions for Scalar Potentials

The scalar potentials for incident plane waves of arbitrary polarization can be represented by a pair of series expansion solutions to the Helmholtz equation in spherical coordinates. The basis functions are the spherical Bessel functions for the radial coordinate  $r$  and the spherical harmonic functions for the angular coordinates. The harmonic functions are given by the Legendre polynomials for the angular coordinate  $\theta$  and the sinusoids for the azimuthal angle  $\phi$ . Here  $\theta$  is the angle between the z-axis, the direction of  $\mathbf{S}^{(i)}$ , and the radius vector  $\mathbf{r}$ , which points to the position at which we wish to evaluate the field. The azimuthal angle  $\phi$  lies in the xy-plane in Fig. 3-1 and is measured clockwise about the z-axis;  $\phi = 0$  along the x-axis.

The time-independent scalar component of a planar and harmonic wave of unit amplitude,  $\exp(ikz)$ , traveling in a non-conducting, homogeneous medium is given by a series expansion in terms of these basis functions by the form

$$\exp(ikz) = \frac{1}{kr} \sum_{l=0}^{\infty} i^l (2l+1) \psi_l(kr) P_l(\cos\theta), \quad z = r \cos\theta \quad (3.2-3)$$

This is Bauer's identity [9], which is derivable from a multipole series expansion of  $\exp(ikr \cos\theta)$  and by use of the addition theorem for spherical harmonic functions. This series is the analog of a Fourier decomposition; the spherical Bessel function,  $\psi_l(kr)$ , and the Legendre polynomial,  $P_l(\cos\theta)$ , provide a complete basis in  $r$  and  $\theta$  space for the series expansion. An individual term in the series multiplied by  $\cos\phi$ , that is,

$\psi_l(kr)P_l(\cos\theta)\cos\phi/kr$ , provides the functional form of the  $l$ th in-plane polarized spherical wavelet and is itself a solution to the Helmholtz equation.

Scalar potential solutions to the Helmholtz equation also can be written in terms of these basis functions. A general form for a scalar potential solution to the Helmholtz equation that is well behaved at the origin is given by the series

$$\Pi = \sum_{l=0}^{\infty} \sum_{m=0}^l (a_{lm} \cos(m\phi) + b_{lm} \sin(m\phi)) \frac{\psi_l(kr)}{kr} P_l^m(\cos\theta) \quad (3.2-4)$$

Here  $a_{lm}$  and  $b_{lm}$  are constant coefficients to be determined, and  $P_l^m(x)$  is the associated Legendre polynomial of degree  $m$  and order  $l$ . Using this general series, one forms the two vector curl operations in Eq. (3.2-2),  $\nabla \times (\Pi \mathbf{r})$  and  $\nabla \times \nabla \times (\Pi \mathbf{r})$ , and equates these expressions respectively (with  $n \equiv 1$ ) to the vector equivalent of Eq. (3.2-3) for a planar wave with in-plane polarization (with  $\mathbf{E}_o$  directed along the x-axis in Fig. 3-1). By equating the two expressions on a term-by-term basis, one can show that the coefficients  $a_{lm}$  and  $b_{lm}$  are forced to assume the values

$$\left. \begin{array}{l} a_{lm} = b_{lm} = 0, \quad m \neq l, \quad \text{or } l = 0 \\ \left\{ \begin{array}{l} a_{l1} = k^{-1} E_o i^{l-1} \frac{2l+1}{l(l+1)} \\ b_{l1} = 0 \end{array} \right\} \text{electric,} \quad \left\{ \begin{array}{l} a_{l1} = 0 \\ b_{l1} = k^{-1} E_o i^{l-1} \frac{2l+1}{l(l+1)} \end{array} \right\} \text{magnetic} \end{array} \right\} \quad (3.2-5)$$

The identity  $\nabla \times \nabla \times (\Pi \mathbf{r}) = (2 + \mathbf{r} \cdot \nabla) \nabla \Pi - \mathbf{r} \nabla^2 \Pi$ , the Helmholtz equation, and the differential equation defining the spherical Bessel function,  $d^2 \psi_l / dx^2 + (1 - l(l+1)/x^2) \psi_l = 0$ , are used to prove Eq. (3.2-5). It follows that the electric and magnetic scalar potentials for a plane wave in a uniform medium ( $n \equiv 1$ ) with an in-plane polarization of constant amplitude  $E_o$  are given by the series expansions

$$\left. \begin{array}{l} {}^e \Pi^{(i)} = \frac{E_o}{rk^2} \sum_{l=1}^{\infty} i^{l-1} \frac{2l+1}{l(l+1)} \psi_l(kr) P_l^1(\cos\theta) \cos\phi \\ {}^m \Pi^{(i)} = \frac{E_o}{rk^2} \sum_{l=1}^{\infty} i^{l-1} \frac{2l+1}{l(l+1)} \psi_l(kr) P_l^1(\cos\theta) \sin\phi \end{array} \right\} \quad (3.2-6)$$

From Eq. (3.2-2),  ${}^e \Pi$  generates the transverse magnetic, or TM, field, that is, the component of the  $\mathbf{H}$  field perpendicular to  $\mathbf{r}$ ;  ${}^m \Pi$  generates the transverse

electric, or TE, field and, therefore, the component of the  $\mathbf{E}$  field perpendicular to  $\mathbf{r}$ . Here  $P_l^1 = -\partial P_l / \partial \theta$ . In the azimuthal coordinate  $\phi$ , the vector components in the vector version of Bauer's identity only involve  $\sin \phi$  and  $\cos \phi$ ; thus,  $m$  in Eq. (3.2-5) can have only the values  $\pm 1$ . The function  $\psi_l(x)$  is related to the Bessel function of the first kind,  $J_{l+1/2}(x)$ , which is of fractional order  $l + 1/2$ , through the expression<sup>1</sup>

$$\psi_l(x) = \sqrt{\frac{\pi x}{2}} J_{l+1/2}(x) \quad (3.2-7)$$

The scattered waves also can be represented by scalar potentials expressed in a series expansion solution to the Helmholtz equation, except in this case the appropriate cylindrical functions to use in the series involve Hankel functions of the first and second kinds,  $H_{l+1/2}^+(x)$  and  $H_{l+1/2}^-(x)$ . Hankel functions behave asymptotically as  $\exp(\pm ikr) / \sqrt{kr}$  for large  $r$ , where the plus sign applies to the first kind and the negative sign to the second kind. We will show that the scalar potentials that use  $H_{l+1/2}^+(x)$  result in scattered waves that behave as  $\exp(ikr) / kr$ , as  $r \rightarrow \infty$ , which matches the spherical form that the scattered wave front must assume at large distances from the scattering source. We will need the spherical Hankel functions  $\xi_l^\pm(x)$ , which are defined in terms of  $H_{l+1/2}^\pm(x)$  by

$$\left. \begin{aligned} \xi_l^+(x) &= \sqrt{\frac{\pi x}{2}} H_{l+1/2}^+(x) = \sqrt{\frac{\pi x}{2}} \left( J_{l+1/2}(x) + iY_{l+1/2}(x) \right) \\ \xi_l^-(x) &= \sqrt{\frac{\pi x}{2}} H_{l+1/2}^-(x) = \sqrt{\frac{\pi x}{2}} \left( J_{l+1/2}(x) - iY_{l+1/2}(x) \right) \end{aligned} \right\} \quad (3.2-8)$$

where  $Y_{l+1/2}(x)$  is the Neumann function of order  $l + 1/2$  and it is the second solution to the Bessel equation, linearly independent of  $J_{l+1/2}(x)$ . These outgoing and incoming wave forms are discussed further in Chapters 4 and 5.

---

<sup>1</sup> We define the spherical Bessel functions  $\psi_l$  and  $\chi_l$  in terms of the integer Bessel functions by  $\psi_l(x) = (\pi x / 2)^{1/2} J_{l+1/2}(x)$ ,  $\chi_l(x) = (\pi x / 2)^{1/2} Y_{l+1/2}(x)$ , where  $J_\nu(x)$  and  $Y_\nu(x)$  are the  $\nu$ th-order Bessel functions of the first and second kind; [8] uses these forms for  $\psi_l$  and  $\chi_l$ , but in most references they are divided by  $x$ .

### 3.3 Multiple Internal Reflections

In the case of a sphere that is not strongly absorbing, scattered waves arise from external reflections from the surface of the sphere, and also from refracted waves that pass through the interior of the sphere. We also have to account for refracted rays that exit the sphere after one or more internal reflections; this mechanism can give rise to rainbow effects. This has been shown in a geometric optics context in Fig. 3-2.

Internal to the sphere, standing waves are established that include both incoming and outgoing waves. The outgoing waves must involve Hankel functions of the first kind because of the asymptotic boundary conditions with large  $r$  cited above. However, the Hankel functions involve the Neumann function, which is unbounded at the origin. Hence, the appropriate cylindrical function for the aggregate incoming and outgoing series for internal standing waves must be a purely spherical Bessel function, i.e., of the form provided by the  $\psi_l(x)$  functions given in Eq. (3.2-7), which are well-behaved at the origin. This can be accomplished by noting from Eq. (3.2-8) that

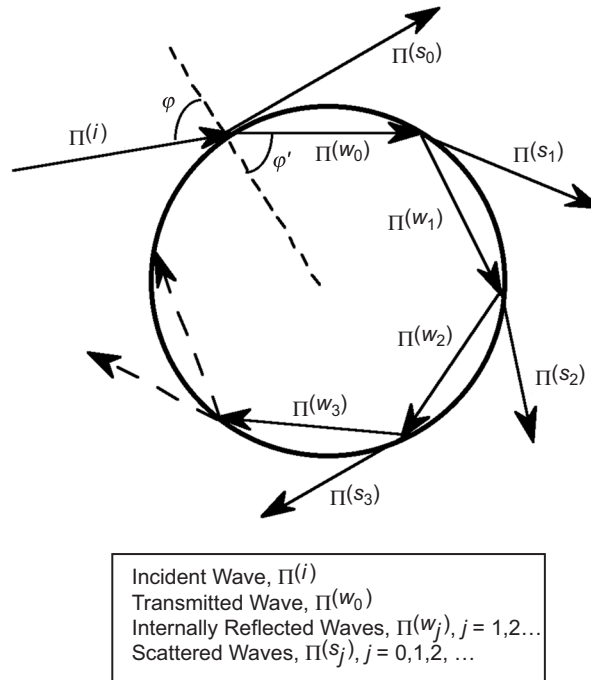


Fig. 3-2. Scattering schematic from a weakly absorbing sphere.

$$\psi_l(x) = \frac{1}{2} \xi_l^+(x) + \frac{1}{2} \xi_l^-(x) \quad (3.3-1)$$

Therefore, we express the scalar potential series for the outgoing internal waves in terms of spherical Hankel functions of the first kind using  $\xi_l^+(x)$ , and the incoming internal waves by spherical Hankel functions of the second kind using  $\xi_l^-(x)$ . If these two series are equally weighted, their sum gives an equivalent series in  $\psi_l(x)$ .

We define the scattered waves in total as comprising those waves that are reflected from the external surface of the sphere as a result of the incident plane wave and also all waves that have passed into the sphere and subsequently escaped from it after zero or more internal reflections. The scalar potential series for the different degrees of scattered waves are defined by

$$\left\{ \begin{array}{l} {}^e\Pi^{(s_j)} = \frac{E_o}{rk^2} \sum_{l=1}^{\infty} {}^e b_l^{(j)} \xi_l^+(kr) P_l^1(\cos\theta) \cos\phi \\ {}^m\Pi^{(s_j)} = \frac{E_o}{rk^2} \sum_{l=1}^{\infty} {}^m b_l^{(j)} \xi_l^+(kr) P_l^1(\cos\theta) \sin\phi \end{array} \right\}, j = 0, 1, 2, \dots; r \geq r_o \quad (3.3-2)$$

The expansion in degree is limited to  $m = 1$  because of the form for the incident wave in Eq. (3.2-6) and because of the continuity conditions in electrodynamics [see Eq. (3.5-1)]. The scattered waves being outgoing, their scalar potentials must use  $\xi_l^+(x)$ . The scattering coefficients  $({}^e b_l^{(j)}, {}^m b_l^{(j)})$ ,  $j = 0, 1, 2, \dots$ , are to be determined from the boundary conditions at the surface of the sphere, which will be discussed later. The scattering coefficients  $({}^e b_l^{(0)}, {}^m b_l^{(0)})$  apply to the zeroth-degree scattered waves, which are those components of the incident plane wave that undergo only an external reflection from the surface of the sphere. For an opaque or an absorbing sphere, only these scattering coefficients would be relevant to our scattering problem. The scattering coefficients  $({}^e b_l^{(j)}, {}^m b_l^{(j)})$ ,  $j = 1, 2, \dots$ , correspond to those components of the incident plane wave that have been transmitted inward and refracted across the surface of the sphere and then have undergone  $j - 1$  internal reflections within the sphere before escaping from it after being refracted again.

What about the standing waves inside the sphere? Their scalar potentials satisfy Eq. (3.2-1c) inside where  $n \neq 1$ ; they are of the form

$$\left. \begin{aligned} e\Pi^{(w_j)} &= \frac{E_o}{rn^2k^2} \sum_{l=1}^{\infty} e a_l^{(j)} \psi_l(nkr) P_l^1(\cos\theta) \cos\phi \\ m\Pi^{(w_j)} &= \frac{E_o}{rnk^2} \sum_{l=1}^{\infty} m a_l^{(j)} \psi_l(nkr) P_l^1(\cos\theta) \sin\phi \end{aligned} \right\}, j = 0, 1, 2, \dots; r \leq r_o \quad (3.3-3)$$

The  $\psi_l(x)$  functions are used to avoid a singularity at the origin. The coefficients  $(e a_l^{(j)}, m a_l^{(j)})$  apply to those waves internal to the sphere that have undergone  $j$  internal reflections. These coefficients also are to be determined from the boundary conditions at the surface of the sphere. However, we must distinguish between incoming waves and outgoing waves. For incoming internal waves that have been transmitted across the boundary surface, or reflected from its inner side, we use in the scalar potential series the form  $a_l^{(j)} \xi_l^-(nkr) / 2$ . For outgoing internal waves that are about to be either reflected from the inner side of the boundary surface or transmitted across it, we use the form  $a_l^{(j)} \xi_l^+(nkr) / 2$ . We show that with this formalism in place for the internal waves, the incident external plane wave also will partition naturally into its incoming component where the Hankel functions of the second kind will apply. The other incident component, the “ongoing” waves, so to speak, that effectively do not interact with the sphere at all, must be represented in terms of Hankel functions of the first kind in order to match the asymptotic boundary conditions as  $r \rightarrow \infty$ .

### 3.4 Fresnel Formulas for Reflection and Transmission Amplitudes

How many internal reflections do we have to take into account for a given accuracy? We should answer this question before taking up the determination of the transmission and scattering coefficients. Guidance can be obtained from the Fresnel formulas in geometric optics for the transmission across and reflection from a dielectric surface. Maxwell’s equations require that both tangential components of  $\mathbf{E}$  and of  $\mathbf{H}$  must be continuous across any surface that is devoid of free charges and surface currents. Also, the normal components of  $\epsilon\mathbf{E}$  and  $\mu\mathbf{H}$  must be continuous. When these conditions are applied to waves impinging on a plane surface of infinite extent, one obtains the Fresnel formulas [8], which provide the ratios of the transmission and reflection amplitudes relative to the incident amplitude at the boundary. For an incident wave with in-plane polarization of the  $\mathbf{E}$  field, these ratios are denoted by  $T_{\parallel} / I_{\parallel}$  and  $R_{\parallel} / I_{\parallel}$ , where  $I_{\parallel}$  is the amplitude of the incident ray. For a cross-plane polarization, they are denoted by  $T_{\perp} / I_{\perp}$  and  $R_{\perp} / I_{\perp}$ . These ratios are

$$\left. \begin{aligned} T_{\parallel} &= \frac{2n_1 \cos \varphi_1}{n_2 \cos \varphi_1 + n_1 \cos \varphi_2} I_{\parallel} = \frac{2 \sin \varphi_2 \cos \varphi_1}{\cos(\varphi_1 - \varphi_2) \cdot \sin(\varphi_1 + \varphi_2)} I_{\parallel} \\ R_{\parallel} &= \frac{n_2 \cos \varphi_1 - n_1 \cos \varphi_2}{n_2 \cos \varphi_1 + n_1 \cos \varphi_2} I_{\parallel} = \frac{\tan(\varphi_1 - \varphi_2)}{\tan(\varphi_1 + \varphi_2)} I_{\parallel} \end{aligned} \right\} \quad (3.4-1a)$$

and

$$\left. \begin{aligned} T_{\perp} &= \frac{2n_1 \cos \varphi_1}{n_1 \cos \varphi_1 + n_2 \cos \varphi_2} I_{\perp} = \frac{2 \sin \varphi_2 \cos \varphi_1}{\sin(\varphi_1 + \varphi_2)} I_{\perp} \\ R_{\perp} &= \frac{n_1 \cos \varphi_1 - n_2 \cos \varphi_2}{n_1 \cos \varphi_1 + n_2 \cos \varphi_2} I_{\perp} = -\frac{\sin(\varphi_1 - \varphi_2)}{\sin(\varphi_1 + \varphi_2)} I_{\perp} \end{aligned} \right\} \quad (3.4-1b)$$

where the subscript “1” denotes the medium on the (left) incident side of the boundary and the subscript “2” denotes the transmitted side (see Fig. 3-3). The angle of incidence  $\varphi_1$  is related to the refracted angle  $\varphi_2$  through Snell’s law,  $n_1 \sin \varphi_1 = n_2 \sin \varphi_2$ , and the second set of equalities in Eqs. (3.3-1a) and (3.3-1b) are obtained by applying Snell’s law. Here the magnetic permeability of the sphere is assumed to be the same as that of the surrounding medium, which is assumed to be a vacuum.

One can easily show from Eqs. (3.4-1a) and (3.4-1b) that  $T_{\perp} / T_{\parallel} = \cos(\varphi_1 - \varphi_2) = 1 + O[n_2 - n_1]$  (with  $I_{\perp} = I_{\parallel} = 1$ ), and similarly for  $R_{\perp} / R_{\parallel}$ , one obtains  $R_{\perp} / R_{\parallel} = -\cos(\varphi_1 + \varphi_2) / \cos(\varphi_1 - \varphi_2)$ . For near-grazing conditions and  $N \ll 1$ ,  $R_{\perp} / R_{\parallel}$  also is essentially unity. Therefore, we consider in the sequel only the in-plane Fresnel coefficients and we set  $I_{\parallel} \equiv 1$ .

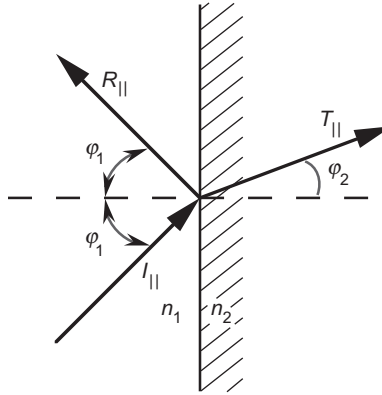


**Fig. 3-3.** Incident, reflected, and transmitted waves across a planar boundary.

The reflection coefficient  $R_{||}$  will be negative if  $n_2 > n_1$  when  $\varphi_1$  exceeds the Brewster angle, that is, when  $\varphi_1 + \varphi_2 > \pi/2$ . This is to be interpreted as a reversal in phase of the reflected ray of  $\pi$  radians relative to the phase of the incident ray. In our radio occultation problem, a ray at a near-grazing angle at a boundary ensures that  $\varphi_1 + \varphi_2 \approx \pi$  and, therefore, that a phase reversal always occurs for reflections from the incident side when  $n_1 < n_2$ , that is, the external reflection.

Figure 3-4 is a plot of the in-plane coefficients as a function of the impact parameter or impact distance of the ray, which in this case is the penetration depth  $h$  of the undeflected ray into the surface of the sphere (for a sphere,  $\varphi \equiv \pi - \theta$ ) and given by

$$h = r_o(1 - \sin\theta), \quad \varphi = \pi - \theta, \quad \pi/2 \leq \theta \leq \pi \quad (3.4-2)$$

One concludes from Fig. 3-4 that the transition from total external reflection to nearly total transmission is completed within a very short impact distance when  $Nr_o$  is small. For  $N = 1.2 \times 10^{-6}$  and  $r_o = 6400$  km, the equivalent impact distance for this figure is less than 10 m, which is far smaller than the first Fresnel zone,  $(\lambda D)^{1/2} \approx 1$  km. Figure 3-4 and, in fact, the concept of ‘‘impact distance’’ apply to the LEO observables only where  $Nr_o \gg (\lambda D)^{1/2}$ , or for a LEO using Global Positioning System (GPS) signals, when  $N \gg 10^{-4}$ . In our examples to follow,  $N \ll 10^{-4}$ , so the first Fresnel zone acts like a

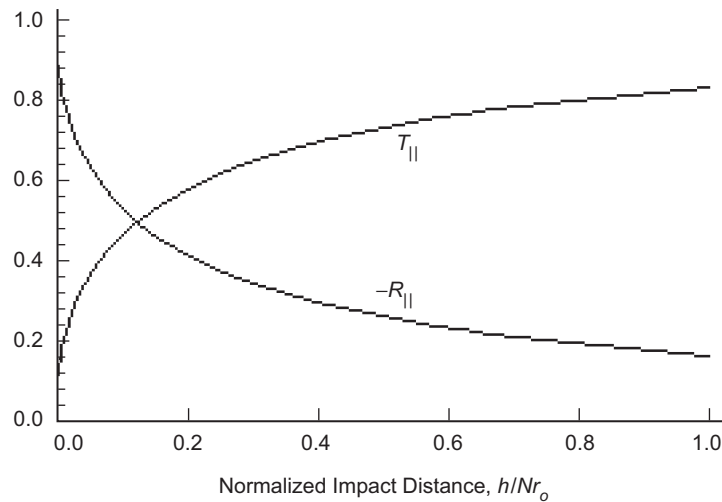


Fig. 3-4. Transmission and reflection ratios for an external wave impinging on a sphere of radius  $r_o$  and uniform refractivity  $N$ .

“smoothing” filter, blurring the variability implied by Fig. 3-4 that otherwise would be observed by the LEO.

We note from Eq. (3.4-1a) that

$$n_2 T_{\parallel} = n_1 (1 + R_{\parallel}) \quad (3.4-3)$$

which will be useful later in evaluating the coefficients in Mie scattering theory.

### 3.4.1 Conservation Principle

Let  $R[\varphi, n]$  and  $T[\varphi, n]$  denote the reflection and transmission ratios, respectively, for an external wave with either in-plane or cross-plane polarization impinging on the outer surface at an angle of incidence  $\varphi$  (see Fig 3-3) and with  $n = n_2 / n_1$ . Similarly,  $R[\varphi', n^{-1}]$  and  $T[\varphi', n^{-1}]$  are the reflection and transmission ratios for an internal wave impinging on the inner side of the boundary surface at an angle of incidence  $\varphi'$ , which is given from Snell's law by  $\varphi' = \arcsin(n^{-1} \sin \varphi)$ .

Let  $A^{(j)}$  be the amplitude of the scattered ray of  $j$ th degree at the surface of the sphere (disregarding space losses and using a geometric optics approach). Then, it follows for a perfectly transparent sphere that  $A^{(j)}$  is given by

$$\left. \begin{aligned} A^{(0)} &= R[\varphi, n] \\ A^{(j)} &= T[\varphi, n] \left( R[\varphi', n^{-1}] \right)^{j-1} T[\varphi', n^{-1}], \quad j = 1, 2, \dots \end{aligned} \right\} \quad (3.4-4)$$

From Poynting's vector, the radiant power per unit area carried by an incident wave striking a boundary is given by  $-\hat{\mathbf{r}} \cdot \mathbf{S}^{(i)}$ , where  $\hat{\mathbf{r}}$  is the outward unit normal vector to the tangent plane at the point of impact of the ray with the boundary surface. This quantity must be conserved in a non-absorbing medium. Therefore, the total radiant power carried away by the reflected and transmitted waves at the boundary must equal the incident power; that is,

$$\hat{\mathbf{r}} \cdot \mathbf{S}^{(i)} + \hat{\mathbf{r}} \cdot \mathbf{S}^{(R)} - \hat{\mathbf{r}} \cdot \mathbf{S}^{(T)} = 0 \quad (3.4-5)$$

$\mathbf{S}^{(R)}$  and  $\mathbf{S}^{(T)}$  are the Poynting vectors for the reflected and transmitted waves. From Snell's law and the Poynting vector for plane waves ( $|\mathbf{S}| = c\sqrt{\epsilon/\mu}E^2/4\pi$ ), it can be shown for an incident ray at both the external and internal sides of the boundary that the conservation constraint for power given in Eq. (3.4-5) results in the conditions

$$\left. \begin{aligned} (R[\varphi, n])^2 + (T[\varphi, n])^2 \frac{\tan \varphi}{\tan \varphi'} &= 1 \\ (R[\varphi', n^{-1}])^2 + (T[\varphi', n^{-1}])^2 \frac{\tan \varphi'}{\tan \varphi} &= 1 \end{aligned} \right\} \quad (3.4-6)$$

From Eqs. (3.4-4) and (3.4-6), it follows that

$$\sum_{j=0}^{\infty} (A^{(j)})^2 = 1 \quad (3.4-7)$$

Thus,  $(A^{(j)})^2$  can be considered as the relative intensity of the  $j$ th scattered component.

### 3.4.2 Scattering Angles and Intensities

The scattering angle  $\Psi^{(j)}(\varphi, n)$  that the  $j$ th degree ray undergoes upon departing from the sphere after  $j-1$  internal reflections is easily obtained from Snell's law and ray tracing through the sphere (see Fig. 3-2); this angle is given by

$$\left. \begin{aligned} \Psi^{(j)} &= (\pi - 2\varphi)(j-1) + 2j(\varphi - \varphi') \\ \varphi' &= \sin^{-1}(n^{-1} \sin \varphi), \quad j = 0, 1, 2, \dots \end{aligned} \right\} \quad (3.4-8)$$

where  $\Psi^{(j)}(\varphi, n)$  is measured clockwise from the positive z-axis (see Fig. 3-1). Thus,  $\Psi^{(0)}$  is the scattering angle for the external reflected wave (and, therefore, negative);  $\Psi^{(1)}$  is the angle for the "primary" ray, which passes through the sphere without reflection and is doubly refracted. The scattering angle  $\Psi^{(2)}$  is for a ray that is internally reflected once and refracted twice. When  $\Psi^{(2)}$  assumes its stationary value with respect to the incident angle  $\varphi$  of the incoming ray, that is, when a caustic surface is formed (see Appendix B), that value of  $\Psi^{(2)}$  marks the scattering angle of the primary rainbow from a raindrop. Similarly, the stationary value of  $\Psi^{(3)}$  marks the direction of the secondary rainbow.

We can evaluate the relative importance of the higher-degree scattered rays to our diffraction problem by plotting both  $\Psi^{(j)}$  and  $A^{(j)}$  versus incident angle  $\varphi$  or, equivalently, the impact distance of the ray [Eq. (3.3-2)], which is measured positive downward from the surface at  $r = r_o$ .

Figure 3-5 displays the normalized scattering angle  $\Psi^{(j)}(h)/(2N)^{1/2}$  versus  $h/(Nr_o)$  for various scattering degrees. In Fig. 3-5(a), the  $j = 0$  curve is

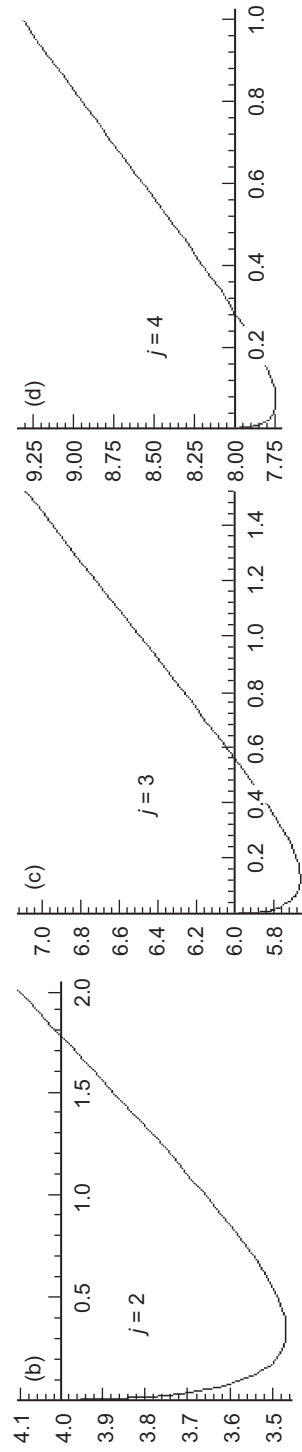
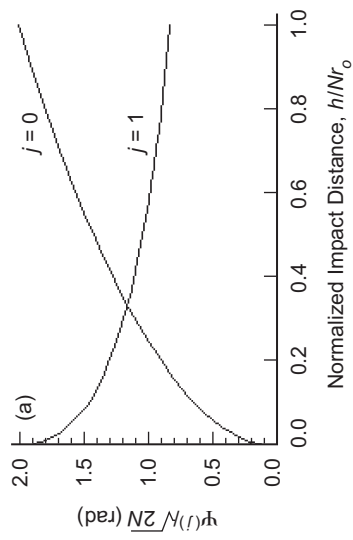


Fig. 3-5. Normalized scattering angle profiles for different  $j$  values: (a) external reflected wave and refracted wave, no internal reflection, and scattering angle for waves with (b) one, (c) two, and (d) three internal reflections.

for  $-\Psi^{(0)}(2N)^{-1/2}$ . In Fig. 3-5(b), rainbow caustics occur where  $\partial\Psi^{(j)}/\partial h = 0$ ; the impact distance giving this stationary value is defined by  $h = h_*^{(j)}$ . We will show in Mie scattering theory (see Section 3.16 and Fig. 3-29) that when  $N$  exceeds a threshold limit,  $N > \sim (\lambda/r_o)^{2/3}$ ,  $\approx 10^{-5}$ , the scattering intensity will become prominent at a scattering angle near  $2(6N)^{1/2}$  for  $j = 2$ . Below this threshold, the rainbow effects, particularly when seen at LEO distances, will be largely washed out. We are dealing with a single sphere [in contrast to an ensemble of raindrops, all refracting and reflecting coherently, and an ensemble whose extent subtends an angle at the observer that is much larger than that subtended by the first Fresnel zone  $(\lambda/D)^{1/2}$ ]. Consequently, the rainbow effects from the single sphere that are seen by the LEO will be mostly washed out if  $h_* \ll (\lambda D)^{1/2}$ .

For near-grazing ray path conditions ( $\varphi \approx \pi/2$ ), the stationary value of the scattering angle with respect to impact distance is given by

$$\Psi_{\min}^{(j)} \doteq \frac{2}{n} \sqrt{\frac{n^2-1}{j^2-1}} (j^2-n) = 2 \left[ 2N(j^2-1) \right]^{1/2} + O[N^2] \quad (3.4-9)$$

Moreover, the impact distance providing that stationary value is given by

$$h_*^{(j)} \doteq r_o \left( 1 - \sqrt{\frac{j^2-n^2}{j^2-1}} \right) = \frac{Nr_o}{j^2-1} + O[N^2] \quad (3.4-10)$$

Figure 3-6 shows the relative amplitudes of the scattered waves  $A^{(j)}(h)$ . It can be shown that the value  $A_*^{(j)}$  at the stationary scattering angle is given by

$$A_*^{(j)} = \frac{4j}{(j+1)^2} \left( \frac{j-1}{j+1} \right)^{j-1} \quad (3.4-11)$$

which approaches  $4/(je^2)$  for large values of  $j$ . Appreciable intensities occur in scattering for degrees  $j \geq 2$  because the near-grazing angles of incidence result in significant internal reflections.

Figure 3-7 shows that as the impact distance  $h \rightarrow 0^+$ , an infinite number of quasi-evanescent waves are generated (see Fig. 3-2). These waves follow chords in the sphere; as the impact distance  $h \rightarrow 0^+$ , the angle that these chords make at their vertices with respect to the normal vector to the surface approaches the critical reflection angle  $\arcsin(1/n)$ . These boundary waves spin off scattered waves like a fireworks pinwheel. The Fresnel formulas can be used to figure out the damping rate. When the refractivity is such that a

rotational commensurability exists, that is, when there is an exact integer number of chords spanning the sphere after one revolution ( $\pi(2N)^{-1/2} = \text{an integer}$ ), a kind of resonance occurs at these scattering points. This has an analog in complex angular momentum theory of sub-atomic particles in high-energy physics involving scattering resonances for selected impact parameter/energy values of the bombarding particles.

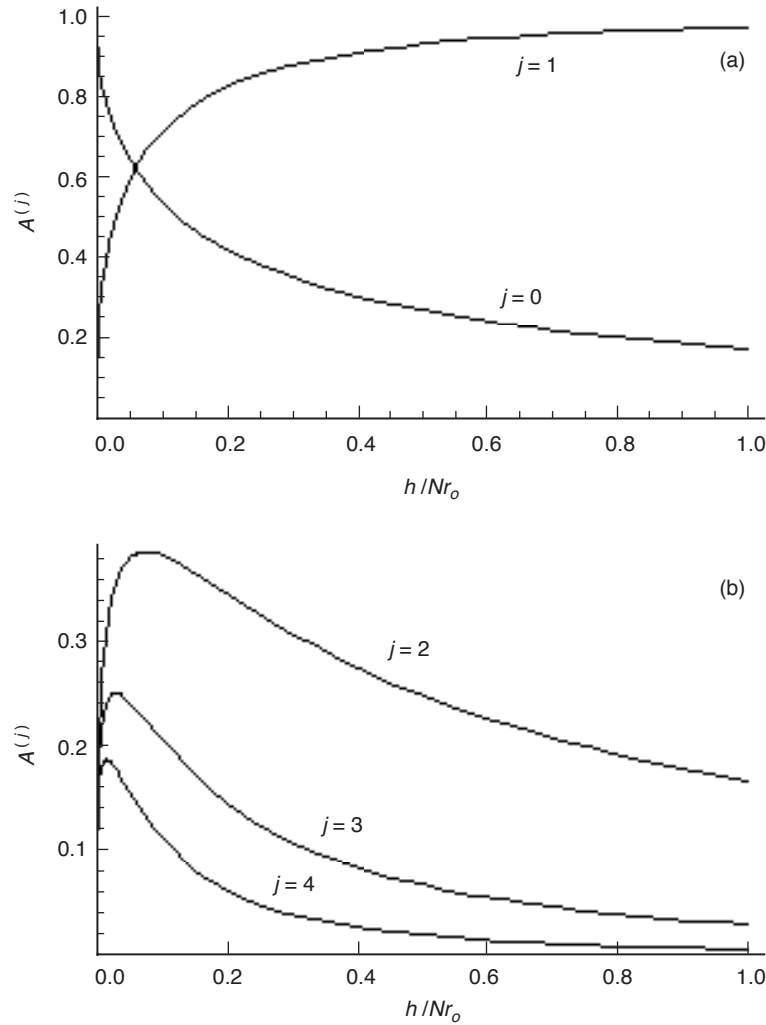


**Fig. 3-6.** Relative intensities of scattered waves: (a) external reflected wave, and refracted wave with no internal reflection, and (b) refracted waves with one, two, and three internal reflections.

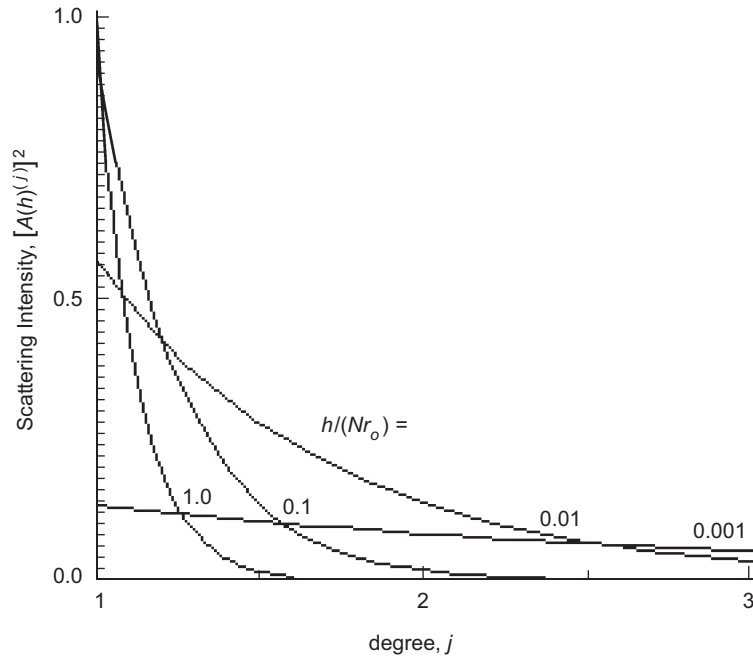


Fig. 3-7. Scattering intensity versus scattering degree shown parametrically with impact distance.

### 3.4.3 Caustics

Another measure of the contributions of the higher-degree scattered waves is to examine their “intensity density.” The impact distances of the ray paths of the incident plane waves will be equally distributed. Therefore, the scattered waves will “pile up” at a scattering angle that has a stationary value with respect to the impact distance of the impinging external ray, that is, at an impact distance where  $\partial\Psi^{(j)}/\partial h = 0$ . This defines the neighborhood where a caustic surface is formed by the ray system inside the sphere; one example of this is manifested by the rainbow in scattering from a raindrop. We define “intensity density” as  $(A^{(j)})^2(\partial\Psi^{(j)}/\partial h)^{-1}$ , which has been shown in Fig. 3-8 for the low-degree scattering. Caustic resonances occur for all scattering degrees when  $j \geq 2$ , but with rapidly diminishing effect with increasing  $j$  [see Eq. (3.4-11)].

We note that geometric optics predicts an infinite intensity density at the caustic resonances. Geometric optics is based on second-order stationary-phase theory, which breaks down at caustics. A third-order treatment leads to more realistic predictions. However, Mie scattering theory yields the correct predictions for these difficult points. Even without Mie scattering theory, we

can see early on from this purely geometric optics-based discussion that the thin-screen model will not account for the scattering at degrees higher than 1 without further enhancement.<sup>2</sup> We will show that Mie scattering theory yields resonances at these scattering angles near  $2(2N(j^2 - 1))^{1/2}$ . We should also expect to see interference fringes at a scattering angle slightly above the stationary point that arise from incident plane waves arriving at the sphere with their ray paths at slightly offset impact distances above and below the point providing the stationary scattering angle. Therefore, scattered rays that arrive at the LEO from these separate impact points will have followed slightly different paths, which will have slightly different optical lengths. These unequal optical lengths result in phase offsets in the arriving rays at the LEO and, hence, phase interference will result. This interference has its analog in supernumerary arcs seen sometimes on the bright side of the primary rainbow, which were first explained by Thomas Young in the early 19th century in terms of his wave theory for light. For scattering higher than degree  $j = 2$ , these effects are diminished [see Eq. (3.4-11)] and also the scattering angles are larger, increasing essentially linearly with increasing degree [see Eq. (3.4-9)].

For the LEO, which is at a distance  $D$  from the limb, this resonance occurs when  $\partial\Psi^{(j)}/\partial h = D^{-1} \approx 0$ . For the degree  $j = 2$  caustic, this occurs at an epoch  $\sim 2 \times 10^3 (2N)^{1/2}$  sec after first passing into the geometric shadow zone. Thus,

---

<sup>2</sup> We could, however, embed the thin-screen model with a modified phase and amplitude profile that attempts to account for the multi-degree scattering. Let  $E^{(j)}(h_{\text{LG}}) \exp[i\vartheta^{(j)}(h_{\text{LG}})]$  denote the amplitude and phase of the  $j$ th degree scattered ray that is observed by the LEO, which is located at a perpendicular distance  $D$  from the thin screen and at an altitude  $h_{\text{LG}}$  relative to the altitude of the zero impact point, i.e., at  $r = r_o, \theta = \pi/2$ . Using the thin-screen model, and expressing distances in phase units, the Rayleigh–Sommerfeld integral becomes

$$E^{(j)} \exp[i\vartheta^{(j)}] = \sqrt{\frac{1}{\pi D} \left( \frac{1}{\pi D} \right)} \frac{1}{1+i} \int_0^\infty A^{(j)}(h_s) \exp \left[ i \frac{(h_s - h_{\text{LG}})^2}{D} + i\varepsilon^{(j)}(h_s) \right] dh_s, j = 0, 1, \dots$$

where  $\varepsilon^{(j)}(h_s)$  is the phase embedded in the thin screen at an impact distance  $h_s$  due to the  $j$ th scatterer, and  $A^{(j)}(h_s)$  is its relative amplitude. For each value of  $j$ , the scattered ray must satisfy the stationary-phase condition; therefore,  $d\varepsilon^{(j)}/dh_s = -k\Psi^{(j)}$ , where  $\Psi^{(j)}(h_s)$  is given from Eqs. (3.4-2) and (3.4-8). The relative amplitude  $A^{(j)}(h_s)$  is given from Eq. (3.4-4). Fresnel diffraction effects from the  $j$ th-degree scattering principally would be evident at scattering angles that are in the neighborhood of the  $j$ th rainbow caustic, i.e., where  $d\Psi^{(j)}(h_s)/dh_s = 1/D \approx 0$ . In this modified form, the combined electric field observed by the LEO would be given by summing the weighted phasors for all degrees,  $j = 0, 1, 2, \dots$

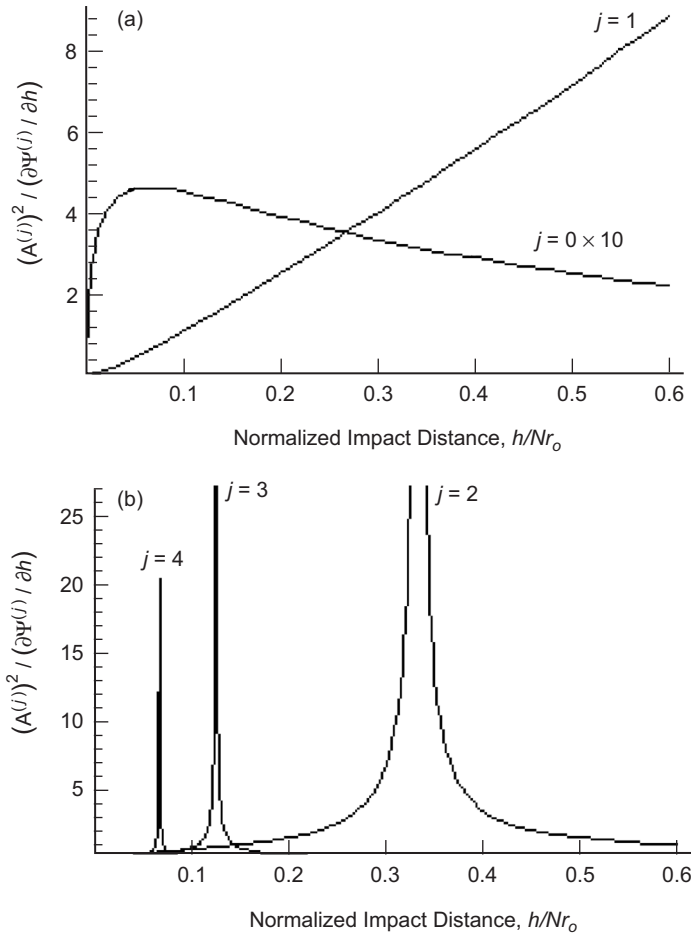


**Fig. 3-8. Intensity densities for scattered waves: (a) external reflected wave, and refracted wave with no internal reflection, and (b) refracted waves with one, two, and three internal reflections.**

from a super-refracting marine layer with a near hard discontinuity of  $N$  across its upper boundary, we might expect to “see” these rainbow effects of degree  $j = 2$  as the LEO descends deeper into the refracted shadow zone. In our case, the orbital velocity of a LEO at an orbital radius of  $1.1r_0$  is of the order of 1 mrad/ms. So, even when the deceleration of the rate of decent of the impact parameter of the ray from defocusing in the lower troposphere is taken into account, transient rainbow boundary phenomena are completed within seconds (see Fig. 3-29 for  $j = 2$  and  $j = 3$  effects).

To fully account for the scattering exactly at the shadow zone boundary, one needs to keep a large number of scattering terms. Even Mie theory may have computational difficulty on such boundaries when  $N$  is large. The boundary (or more precisely, the chords at the critical internal reflection angle) of our spherical model is a caustic surface, which presents a singular situation.

It is ironic that our seemingly simple, transparent sphere would present such complications. An opaque sphere is easier.

### 3.5 Mie Scattering Theory: Obtaining the Scattering Coefficients at a Boundary

To obtain the relationships between the scattering and transmission coefficients, we again use the conditions from Maxwell's equations that the tangential components of  $\mathbf{E}$  and  $\mathbf{H}$  must be continuous across a charge and current-free boundary that bears a discontinuity in  $\epsilon$  and/or  $\mu$ :  $\mathbf{E}_{\text{tan}}^{(i)} + \mathbf{E}_{\text{tan}}^{(S)} = \mathbf{E}_{\text{tan}}^{(w)}$ ;  $\mathbf{H}_{\text{tan}}^{(i)} + \mathbf{H}_{\text{tan}}^{(S)} = \mathbf{H}_{\text{tan}}^{(w)}$ . In addition, Maxwell's equations also require that the radial components of  $\epsilon\mathbf{E}$  and  $\mu\mathbf{H}$  be continuous across the boundary. These conditions were used earlier to obtain the Fresnel formulas. It follows that a correspondence between these coefficients and the Fresnel ratios should exist, which will be established.

#### 3.5.1 Transmission and Reflection Coefficients for Incident External Waves

First we will deal with the incident external wave and its reflection and transmission at the boundary surface. As the incident external wave is an incoming one at the boundary, its scalar potential series in Eq. (3.2-6) will naturally partition into a series where  $\xi_l^-(x)$  is used for the incident component, and into a series for the "ongoing" component where  $\xi_l^+(x)$  is used. Why is this plausible? There are two reasons. In the limit as  $N \rightarrow 0$  the incoming external waves must match the incoming internal waves at the boundary, which involves only  $\xi_l^-(x)$ . The second reason, as we will show shortly, is that when we calculate the scattering coefficients ( ${}^e b_l^{(0)}, {}^m b_l^{(0)}$ ) that arise from the incident external waves, they cancel completely the  $\xi_l^+(x)$  component of that incident field.

The continuity conditions on the components of  $\mathbf{E}$  and  $\mathbf{H}$ , which were mentioned above, are given in terms of an equivalent set of continuity conditions on the scalar potentials for these waves,  ${}^e \Pi r$  and  ${}^m \Pi r$ , and also on the radial components of their gradients across the surface of the sphere [8]. These are given by

$$\left. \begin{aligned}
\frac{\partial}{\partial r} [r(e\Pi^{(i)} + e\Pi^{(s_o)})]_{r=r_o^+} &= \frac{\partial}{\partial r} [r(e\Pi^{-(w_o)})]_{r=r_o^-} \\
\frac{\partial}{\partial r} [r(m\Pi^{(i)} + m\Pi^{(s_o)})]_{r=r_o^+} &= \frac{\partial}{\partial r} [r(m\Pi^{-(w_o)})]_{r=r_o^-} \\
[r(e\Pi^{(i)} + e\Pi^{(s_o)})]_{r=r_o^+} &= n^2 [r(e\Pi^{-(w_o)})]_{r=r_o^-} \\
[r(m\Pi^{(i)} + m\Pi^{(s_o)})]_{r=r_o^+} &= [r(m\Pi^{-(w_o)})]_{r=r_o^-}
\end{aligned} \right\} \quad (3.5-1)$$

Here  $\Pi^{-(w_o)}$  denotes the partitioned component of the scalar potential for the interior wave that has just crossed the boundary, and, therefore, it corresponds to an incoming wave. In general, the partitioned scalar potential series for interior incoming (-) and outgoing (+) waves are given from Eqs. (3.3-1) and (3.3-3) by

$$\left. \begin{aligned}
e\Pi^{\pm(w_j)} &= \frac{E_o}{2rn^2k^2} \sum_{l=1}^{\infty} e a_l^{(j)} \xi_l^{\pm}(nkr) P_l^1(\cos\theta) \cos\phi \\
m\Pi^{\pm(w_j)} &= \frac{E_o}{2rnk^2} \sum_{l=1}^{\infty} m a_l^{(j)} \xi_l^{\pm}(nkr) P_l^1(\cos\theta) \sin\phi
\end{aligned} \right\}, j = 0, 1, \dots; r \leq r_o \quad (3.5-2)$$

We apply the continuity conditions in Eq. (3.5-1) at all points on the surface of the sphere to the series expansions to the scalar potentials for the incident plane wave in Eq. (3.2-6) and to the zeroth-degree scattering and transmitted components in Eqs. (3.3-2) and (3.5-2). Using the orthogonality properties of the spherical harmonics, we obtain for each integer value of spectral number the transfer equations required by the continuity conditions:

$$\left. \begin{aligned}
e b_l^{(0)} \xi_l^{+'}(x_o) + i^{l-1} \frac{2l+1}{l(l+1)} \psi_l'(x_o) &= \frac{1}{2n} e a_l^{(0)} \xi_l^{-'}(nx_o) \\
m b_l^{(0)} \xi_l^{+'}(x_o) + i^{l-1} \frac{2l+1}{l(l+1)} \psi_l'(x_o) &= \frac{1}{2} m a_l^{(0)} \xi_l^{-'}(nx_o) \\
e b_l^{(0)} \xi_l^{+}(x_o) + i^{l-1} \frac{2l+1}{l(l+1)} \psi_l(x_o) &= \frac{1}{2} e a_l^{(0)} \xi_l^{-}(nx_o) \\
m b_l^{(0)} \xi_l^{+}(x_o) + i^{l-1} \frac{2l+1}{l(l+1)} \psi_l(x_o) &= \frac{1}{2n} m a_l^{(0)} \xi_l^{-}(nx_o)
\end{aligned} \right\} l = 1, 2, \dots \quad (3.5-3)$$

where  $\xi_l^\pm(x)$  is the derivative of  $\xi_l^\pm$  with respect to  $x$ . We define the dimensionless radial coordinate

$$x = kr, \quad x_o = kr_o \quad (3.5-4)$$

Thus,  $x_o = 2.1 \times 10^8$  for the L1 GPS carrier when  $r_o = 6400$  km; “ $x$ ” here should not be confused with the “up” spatial coordinate shown in Fig. 3-1. Unless otherwise noted, the definition given in Eq. (3.5-4) will apply henceforth.

Solving the system of linear equations in Eq. (3.5-3) and using the relationship between spherical Bessel functions and spherical Hankel functions given in Eq. (3.3-1), we obtain for the scattering and transmission coefficients of zeroth degree

$$\left. \begin{aligned} {}^e b_l^{(0)} &= -i^{l-1} \frac{2l+1}{l(l+1)} \left[ \frac{1}{2} + \frac{1}{2} \frac{\xi_l^-(x_o) \xi_l'^-(nx_o) - n \xi_l'^-(x_o) \xi_l^-(nx_o)}{\xi_l^+(x_o) \xi_l'^-(nx_o) - n \xi_l'^+(x_o) \xi_l^-(nx_o)} \right] \\ {}^m b_l^{(0)} &= -i^{l-1} \frac{2l+1}{l(l+1)} \left[ \frac{1}{2} + \frac{1}{2} \frac{n \xi_l^-(x_o) \xi_l'^-(nx_o) - \xi_l'^-(x_o) \xi_l^-(nx_o)}{n \xi_l^+(x_o) \xi_l'^-(nx_o) - \xi_l'^+(x_o) \xi_l^-(nx_o)} \right] \\ {}^e a_l^{(0)} &= i^{l-1} \frac{2l+1}{l(l+1)} \left[ \frac{-2i}{\xi_l^+(x_o) \xi_l'^-(nx_o) - n \xi_l'^+(x_o) \xi_l^-(nx_o)} \right] n \\ {}^m a_l^{(0)} &= i^{l-1} \frac{2l+1}{l(l+1)} \left[ \frac{-2i}{n \xi_l^+(x_o) \xi_l'^-(nx_o) - \xi_l'^+(x_o) \xi_l^-(nx_o)} \right] n \end{aligned} \right\} \quad (3.5-5)$$

Here, the Wronskian of the spherical Hankel functions,

$$\mathcal{W}[\xi_l^+(x), \xi_l^-(x)] = \xi_l^+(x) \xi_l'^-(x) - \xi_l'^+(x) \xi_l^-(x) = -2i \quad (3.5-6)$$

has been used to obtain the transmission coefficients. If we insert these expressions for the external reflection coefficients ( ${}^e b_l^{(0)}$ ,  ${}^m b_l^{(0)}$ ) into Eq. (3.3-2) for the zeroth-degree scattered wave, we note that the term  $-i^{l-1}(2l+1)/(2l(l+1))$  in that series just cancels exactly the  $\xi_l^+(x)$  component of the scalar potential series for the incident external plane wave given in Eq. (3.2-6). In other words, the  $\xi_l^+(x)$  component in the spectral representation of the incident plane wave never makes it across the boundary of the sphere. Therefore, we can ignore it in calculating all transmission and reflection coefficients, if for ( ${}^e b_l^{(0)}$ ,  ${}^m b_l^{(0)}$ ) we also eliminate the  $-i^{l-1}(2l+1)/2l(l+1)$  term in Eq. (3.5-5), the so-called “-1/2” term.

Also, the “electric” coefficients ( ${}^e a_l^{(0)}$ ,  ${}^e b_l^{(0)}$ ) and the “magnetic” coefficients ( ${}^m a_l^{(0)}$ ,  ${}^m b_l^{(0)}$ ) differ from each other’s counterpart by a small quantity of order  $N$  when near-grazing conditions are assumed. We will focus primarily on the electric potential and in-plane ( $\phi = 0$ ) observations in future sections.

We define

$$\left\{ \begin{matrix} e \\ m \end{matrix} \right\} \tilde{b}_l^{(0)} = \left\{ \begin{matrix} e \\ m \end{matrix} \right\} b_l^{(0)} + i^{l-1} \frac{2l+1}{2l(l+1)} \quad (3.5-7)$$

Thus, ( ${}^e \tilde{b}_l^{(0)}$ ,  ${}^m \tilde{b}_l^{(0)}$ ) are the zeroth-degree scattering terms that result from the partitioned scalar potential series for incoming external waves that is comprised of  $\xi_l^-(x)$  terms only. We note from Eq. (3.5-5) that

$$\left\{ \begin{matrix} e \\ m \end{matrix} \right\} \tilde{b}_l^{(0)} 2 \frac{\xi_l^+(x_o)}{\xi_l^-(x_o)} + 1 = \left\{ \begin{matrix} e \\ m \end{matrix} \right\} a_l^{(0)} \frac{\xi_l^-(nx_o)}{\xi_l^-(x_o)} \quad (3.5-8)$$

The similarity to Eq. (3.4-3) for the relationship between the Fresnel ratios should be noted. If we establish the following correspondence:

$$2 \frac{\xi_l^+(x_o)}{\xi_l^-(x_o)} \tilde{b}_l^{(0)} \leftrightarrow R[\varphi, n], \quad n^{-1} \frac{\xi_l^-(nx_o)}{\xi_l^-(x_o)} a_l^{(0)} \leftrightarrow T[\varphi, n] \quad (3.5-9)$$

we would expect the reflection and transmission coefficients,  $a_l^{(j)}$  and  $\tilde{b}_l^{(j)}$ ,  $j \geq 1$ , for the interior standing waves and escaping waves to adhere to the form given for the amplitude ratios  $A^{(j)}$  given in Eq. (3.4-4). In this case, the Fresnel ratios are complex and dependent on the spectral number  $l$ . The ratio  $\xi_l^+(x_o)/\xi_l^-(x_o)$  provides phase information. Note that  $\xi_l^-(x)$  is the complex conjugate of  $\xi_l^+(x)$  when  $x$  is real. Let  $2\Omega^{(0)}$  be the phase of this ratio; it follows that  $\text{Exp}[i2\Omega^{(0)}] = \xi_l^+(x_o)/\xi_l^-(x_o)$ .

### 3.5.2 Transmission and Reflection Coefficients for Incident Interior Waves

For interior waves reflecting from the inner boundary or escaping across it, the continuity conditions from electrodynamics require

$$\left. \begin{aligned} \frac{\partial}{\partial r} \left[ r \left( {}^e \Pi^{+(w_{j-1})} + {}^e \Pi^{-(w_j)} \right) \right]_{r=r_o^-} &= \frac{\partial}{\partial r} \left[ r \left( {}^e \Pi^{(s_j)} \right) \right]_{r=r_o^+} \\ n^2 \left[ r \left( {}^e \Pi^{+(w_{j-1})} + {}^e \Pi^{-(w_j)} \right) \right]_{r=r_o^-} &= \left[ r \left( {}^e \Pi^{(s_j)} \right) \right]_{r=r_o^+} \\ \frac{\partial}{\partial r} \left[ r \left( {}^m \Pi^{+(w_{j-1})} + {}^m \Pi^{-(w_j)} \right) \right]_{r=r_o^-} &= \frac{\partial}{\partial r} \left[ r \left( {}^m \Pi^{(s_j)} \right) \right]_{r=r_o^+} \\ \left[ r \left( {}^m \Pi^{+(w_{j-1})} + {}^m \Pi^{-(w_j)} \right) \right]_{r=r_o^-} &= \left[ r \left( {}^m \Pi^{(s_j)} \right) \right]_{r=r_o^+} \quad j = 1, 2, \dots \end{aligned} \right\} \quad (3.5-10)$$

Here  $\left\{ \begin{smallmatrix} e \\ m \end{smallmatrix} \right\} \Pi^{+(w_{j-1})}$  represents the outgoing component of the internal standing wave that impinges on the inner surface of the sphere after having undergone  $j-1$  prior internal reflections. Thus,  $\left\{ \begin{smallmatrix} e \\ m \end{smallmatrix} \right\} a_l^{(j-1)}$ , which has been determined already from the  $j-1$ st encounter with the boundary where it was a reflection coefficient (for  $j \geq 2$ ), assumes the “incident wave” role in the  $j$ th encounter. On the other hand,  $\left\{ \begin{smallmatrix} e \\ m \end{smallmatrix} \right\} \Pi^{-(w_j)}$  represents the reflected and, therefore, incoming wave just after its  $j$ th internal reflection. The series forms for  $\left\{ \begin{smallmatrix} e \\ m \end{smallmatrix} \right\} \Pi^{+(w_{j-1})}$  and  $\left\{ \begin{smallmatrix} e \\ m \end{smallmatrix} \right\} \Pi^{-(w_j)}$  are the partitioned forms of Eq. (3.3-3) and are given in Eq. (3.5-2). The scalar potential in the right-hand side (RHS) of Eq. (3.5-10) represents the outgoing transmitted waves, which are the scattered waves of  $j$ th degree, and is given by Eq. (3.3-2). Here  $\left\{ \begin{smallmatrix} e \\ m \end{smallmatrix} \right\} b_l^{(j)}$  acts as a transmission coefficient at this  $j$ th internal encounter with the boundary. Applying the continuity conditions in Eq. (3.5-10) to all interior points on the surface of the sphere, one obtains the recurrence relations for  $\left\{ \begin{smallmatrix} e \\ m \end{smallmatrix} \right\} a_l^{(j)}$  and  $\left\{ \begin{smallmatrix} e \\ m \end{smallmatrix} \right\} b_l^{(j)}$  :

$$\left. \begin{aligned}
\left\{ \begin{matrix} e \\ m \end{matrix} \right\} b_l^{(0)} &= -\frac{1}{2} i^{l-1} \frac{2l+1}{l(l+1)} \left( 1 + \frac{\left\{ \begin{matrix} e \\ m \end{matrix} \right\} \mathcal{W}_l^-}{\left\{ \begin{matrix} e \\ m \end{matrix} \right\} \mathcal{W}_l} \right), \\
\left\{ \begin{matrix} e \\ m \end{matrix} \right\} a_l^{(0)} &= i^{l-1} \frac{2l+1}{l(l+1)} \left( \frac{-2i}{\left\{ \begin{matrix} e \\ m \end{matrix} \right\} \mathcal{W}_l} \right) n, \\
\left\{ \begin{matrix} e \\ m \end{matrix} \right\} b_l^{(j)} &= -i \frac{\left\{ \begin{matrix} e \\ m \end{matrix} \right\} a_l^{(j-1)}}{\left\{ \begin{matrix} e \\ m \end{matrix} \right\} \mathcal{W}_l} = -i \frac{\left\{ \begin{matrix} e \\ m \end{matrix} \right\} a_l^{(j-1)} \left( -\frac{\left\{ \begin{matrix} e \\ m \end{matrix} \right\} \mathcal{W}_l^+}{\left\{ \begin{matrix} e \\ m \end{matrix} \right\} \mathcal{W}_l} \right)^{j-1}}{\left\{ \begin{matrix} e \\ m \end{matrix} \right\} \mathcal{W}_l} \\
&= \frac{1}{2} i^{l-1} \frac{2l+1}{l(l+1)} n \left[ \left( \frac{-2i}{\left\{ \begin{matrix} e \\ m \end{matrix} \right\} \mathcal{W}_l} \right) \left( -\frac{\left\{ \begin{matrix} e \\ m \end{matrix} \right\} \mathcal{W}_l^+}{\left\{ \begin{matrix} e \\ m \end{matrix} \right\} \mathcal{W}_l} \right)^{j-1} \left( \frac{-2i}{\left\{ \begin{matrix} e \\ m \end{matrix} \right\} \mathcal{W}_l} \right) \right], \\
\left\{ \begin{matrix} e \\ m \end{matrix} \right\} a_l^{(j)} &= -\left\{ \begin{matrix} e \\ m \end{matrix} \right\} a_l^{(j-1)} \frac{\left\{ \begin{matrix} e \\ m \end{matrix} \right\} \mathcal{W}_l^+}{\left\{ \begin{matrix} e \\ m \end{matrix} \right\} \mathcal{W}_l} = \left\{ \begin{matrix} e \\ m \end{matrix} \right\} a_l^{(0)} \left( -\frac{\left\{ \begin{matrix} e \\ m \end{matrix} \right\} \mathcal{W}_l^+}{\left\{ \begin{matrix} e \\ m \end{matrix} \right\} \mathcal{W}_l} \right)^j \\
&= i^{l-1} \frac{2l+1}{l(l+1)} n \left[ \left( \frac{-2i}{\left\{ \begin{matrix} e \\ m \end{matrix} \right\} \mathcal{W}_l} \right) \left( -\frac{\left\{ \begin{matrix} e \\ m \end{matrix} \right\} \mathcal{W}_l^+}{\left\{ \begin{matrix} e \\ m \end{matrix} \right\} \mathcal{W}_l} \right)^j \right], \\
{}^e \mathcal{W}_l^\pm &= \xi_l^\pm(x_o) \xi_l^{\pm'}(nx_o) - n \xi_l^{\pm'}(x_o) \xi_l^\pm(nx_o), \\
{}^m \mathcal{W}_l^\pm &= n \xi_l^\pm(x_o) \xi_l^{\pm'}(nx_o) - \xi_l^{\pm'}(x_o) \xi_l^\pm(nx_o), \\
{}^e \mathcal{W}_l &= \xi_l^+(x_o) \xi_l^{-'}(nx_o) - n \xi_l^{-'}(x_o) \xi_l^-(nx_o), \\
{}^m \mathcal{W}_l &= n \xi_l^+(x_o) \xi_l^{-'}(nx_o) - \xi_l^{-'}(x_o) \xi_l^-(nx_o), \\
l &= 1, 2, \dots
\end{aligned} \right\}, j = 1, 2, \dots \quad (3.5-11)$$

Comparing the form of the scattering coefficients  $b_l^{(j)}$  with the form for the amplitudes  $A^{(j)}$  from geometric optics given in Eq. (3.4-4) for the  $j$ th-degree scattered wave, we see the correspondence

$$\left. \begin{aligned}
-\frac{{}^e \mathcal{W}_l^+ \xi_l^-(nx_o)}{{}^e \mathcal{W}_l \xi_l^+(nx_o)} &\Leftrightarrow R[\varphi', n^{-1}] \\
-\frac{2i \xi_l^+(nx_o)}{{}^e \mathcal{W}_l \xi_l^+(x_o)} &\Leftrightarrow n^{-1} T[\varphi', n^{-1}]
\end{aligned} \right\} \quad (3.5-12a)$$

Here we have the relation

$$R[\varphi', n^{-1}] + 1 = n^{-1}T[\varphi', n^{-1}] \quad (3.5-12b)$$

which, using Eqs. (3.5-11) and (3.5-6), is readily shown to hold.

### 3.5.3 Aggregate Scattering

The total field (scattered plus incident) outside of the sphere is given by

$$\left\{ \begin{matrix} e \\ m \end{matrix} \right\} \Pi_{\text{Total}} = \left\{ \begin{matrix} e \\ m \end{matrix} \right\} \Pi^{(i)} + \left\{ \begin{matrix} e \\ m \end{matrix} \right\} \Pi^{(s)} = \left\{ \begin{matrix} e \\ m \end{matrix} \right\} \Pi^{(i)} + \sum_{j=0}^{\infty} \left\{ \begin{matrix} e \\ m \end{matrix} \right\} \Pi^{(s_j)}, \quad r \geq r_o \quad (3.5-13)$$

where the coefficients  $b_l^{(j)}$ ,  $j = 0, 1, 2, \dots$ , are obtained from Eq. (3.5-11), and  $\Pi^{(i)}$  and  $\Pi^{(s_j)}$  are given by Eqs. (3.2-6) and (3.3-2), respectively. Carrying out the summation in Eq. (3.5-13) and using the form for the scattering coefficients given in Eq. (3.5-11), one obtains for the aggregate scattering

$$\begin{aligned} \left\{ \begin{matrix} e \\ m \end{matrix} \right\} \Pi^{(s)} &= \sum_{j=0}^{\infty} \left\{ \begin{matrix} e \\ m \end{matrix} \right\} \Pi^{(s_j)} = -\frac{E_o}{rk^2} \begin{Bmatrix} \cos \phi \\ \sin \phi \end{Bmatrix} \\ &\times \sum_{l=1}^{\infty} \left\{ \begin{matrix} e \\ m \end{matrix} \right\} S_l i^{l-1} \frac{2l+1}{l(l+1)} \xi_l^+(kr) P_l^1(\cos \theta), \quad r \geq r_o \end{aligned} \quad (3.5-14)$$

where the aggregate scattering coefficient  $S_l$  is

$$\begin{aligned} \left\{ \begin{matrix} e \\ m \end{matrix} \right\} S_l &= \left( i^{l-1} \frac{2l+1}{l(l+1)} \right)^{-1} \sum_{j=0}^{\infty} \left\{ \begin{matrix} e \\ m \end{matrix} \right\} b_l^{(j)} \\ &= - \left[ \frac{2n}{\left\{ \begin{matrix} e \\ m \end{matrix} \right\} \mathcal{W}_l^+ \left\{ \begin{matrix} e \\ m \end{matrix} \right\} \mathcal{W}_l^+} + \frac{\left\{ \begin{matrix} e \\ m \end{matrix} \right\} \mathcal{W}_l^+ \left\{ \begin{matrix} e \\ m \end{matrix} \right\} \mathcal{W}_l^-}{2} \right] \left( \frac{1}{\left\{ \begin{matrix} e \\ m \end{matrix} \right\} \mathcal{W}_l} \right) \end{aligned} \quad (3.5-15a)$$

This form includes the “ $-1/2$ ” contribution from the  $b_l^{(0)}$  term, which completely cancels the  $\xi_l^+(kr)$  component of the scalar potential series [Eq. (3.2-6)] for the incident plane wave, leaving only the  $\xi_l^-(kr)$  component in that series. Equation (3.5-15a) can be simplified somewhat by using the Wronskian forms in Eqs. (3.5-6) and (3.5-11). It becomes

$$2^{\{e\}} S_l + 1 = - \frac{\{e\} \tilde{\mathcal{W}}_l + \{e\} \mathcal{W}_l^-}{\{e\} \mathcal{W}_l + \{e\} \mathcal{W}_l^+} \quad (3.5-15b)$$

where  $\tilde{\mathcal{W}}_l$  is given by

$$\left. \begin{aligned} {}^e \tilde{\mathcal{W}}_l &= \xi_l^-(x_o) \xi_l^+(nx_o) - n \xi_l^-(x_o) \xi_l^+(nx_o) \\ {}^m \tilde{\mathcal{W}}_l &= n \xi_l^-(x_o) \xi_l^+(nx_o) - \xi_l^-(x_o) \xi_l^+(nx_o) \end{aligned} \right\} \quad (3.5-16)$$

$\tilde{\mathcal{W}}_l$  is the complex conjugate of  $\mathcal{W}_l$  when  $x$  and  $l$  are real.

As a credibility check, first let us determine the limiting form of  $\Pi^{(s)}$  as  $nx_o \rightarrow x_o$ . In this case,  $\mathcal{W}_l^\pm \rightarrow 0$  and  $\mathcal{W}_l \rightarrow -2i$ . Therefore,  $S_l \rightarrow 0$  and  $\Pi^{(s)} \rightarrow 0$ . What about the individual scattering coefficients? The non-zero coefficients have the limiting forms  $b_l^{(0)} \rightarrow -(1/2)i^{l-1}(2l+1)/l(l+1)$ ,  $a_l^{(0)} \rightarrow i^{l-1}(2l+1)/l(l+1)$ , and  $b_l^{(1)} \rightarrow (1/2)i^{l-1}(2l+1)/l(l+1)$ . Thus,  $b_l^{(0)}$  and  $b_l^{(1)}$  cancel each other and  $a_l^{(0)}$  assumes the form of the coefficient for the incident plane wave, as expected. A second check is for  $n \rightarrow \infty$ . Here  ${}^e b_l^{(0)} \rightarrow -[\psi_l'(x_o)/\xi_l^+(x_o)]i^{l-1}(2l+1)/l(l+1)$ ,  ${}^m b_l^{(0)} \rightarrow -[\psi_l(x_o)/\xi_l^+(x_o)]i^{l-1}(2l+1)/l(l+1)$ , and all other coefficients approach zero, which is as expected for an in-plane polarized wave scattered from a perfectly reflecting sphere [8]. If one introduces absorption into the sphere but with a finite refractivity, then  $n$  would become complex and  $\xi_l^\pm(nx_o)$  must be expressed in terms of modified Bessel and Neumann functions. It will be shown in this case that the enormity of  $x_o$  forces all coefficients to zero except  $b_l^{(0)}$  when only a minuscule absorption coefficient is introduced.

Because the differences in the electric and magnetic scattering coefficients are small when  $N \ll 1$ , and to simplify the notation, we will suppress the superscripts “e” and “m” on the scattering coefficients; we retain only the electric coefficients in the following sections. The magnetic coefficients can easily be reconstituted. GPS signals are principally right-hand circular polarized; therefore, to study polarization effects from the refracting sphere, we also would need the scattering terms for cross-plane polarization. To obtain the scattered wave from a cross-plane polarized incident wave, we use the  $\mathbf{H}$  field from the in-plane case and the symmetry in Maxwell’s equations mentioned earlier, in which the definitions of the field and its medium parameters are exchanged:  $(\mathbf{E}, \mathbf{H}, \varepsilon, \mu) \Leftrightarrow (-\mathbf{H}, \mathbf{E}, \mu, \varepsilon)$ .

### 3.6 The Problem of Slow Convergence

The series in Eqs. (3.2-4), (3.3-2), and (3.5-14) converge rapidly only when  $kr$  is small or moderate; but in our problem,  $kr_o \sim 10^8$ , so in this case another technique must be used to evaluate these series rather than direct summation. When  $l \ll x$ , it is easily shown for large  $x$  that [10]

$$\psi_l(x) \rightarrow \sin(x - l\pi/2), \quad l \ll x \quad (3.6-1)$$

This is easily seen from the differential equation for  $\psi_l(x) = (\pi x/2)^{1/2} J_{l+1/2}(x)$ , which is given from Bessel's equation by

$$\psi_l'' + \left(1 - \frac{l(l+1)}{x^2}\right) \psi_l = 0 \quad (3.6-2)$$

Because  $x \gg 1$ , we can linearize Eq. (3.6-2) by writing  $x = kr_o + y$ , where  $y$  is to be considered as a relatively small excursion of  $x$  from its nominal value of  $x_o = kr_o$ . Equation (3.6-2) becomes

$$\left. \begin{aligned} \psi_l'' + (K_l + M_l y) \psi_l &= 0 \\ K_l &= 1 - \frac{l(l+1)}{x_o^2} \\ M_l &= \frac{2l(l+1)}{x_o^3} \end{aligned} \right\} \quad (3.6-3)$$

For  $l \ll x_o$ ,  $\psi_l(y)$  behaves sinusoidally with  $y$ . For  $l \gg x_o$ ,  $\psi_l(y)$  behaves exponentially. For  $l = x_o$ ,  $K_l = 0$ , and the solutions to Eq. (3.6-2) are the Airy functions of the first and second kind. In the neighborhood where  $K_l + M_l y \approx 0$ ,  $\psi_l(y)$  undergoes a transition from a sinusoidal behavior to an exponential one. The Wentzel-Kramer-Brillouin (WKB) method [11] provides a useful technique for evaluating the asymptotic solutions to this equation.

It follows that for  $l \ll x_o$  the coefficients in the series for the incident and scattered waves in Eqs. (3.2-6) and (3.3-2) chatter wildly throughout this regime. Using the asymptotic forms for the Hankel functions,  $\xi_l^\pm(x) \sim (\mp i)^{l+1} \exp(\pm ix)$ , which apply when  $l \ll x_o = kr_o \gg 1$ , we find that the Wronskian-like terms  $\mathcal{W}_l^\pm$  and  $\mathcal{W}_l$  behave as  $\mathcal{W}_l^\pm \rightarrow 0$  and  $\mathcal{W}_l \rightarrow -2i \exp(-iNx_o)$ . Therefore, the aggregate scattering coefficient  $S_l$  becomes

$$2S_l \rightarrow \exp(2iNx_o) - 1, \quad l \ll x_o = kr_o \gg 1 \quad (3.6-4)$$

Let the partial sum for a scalar potential series,  $\Pi_{l^*}$ , be given by

$$\Pi_{l^*} = \sum_{l=1}^{l^*} f(x, \theta, \phi, l) \quad (3.6-5)$$

where  $f$  stands for the summand in any one of the series representations for the incident or scattered waves. It follows that the scalar potential for the spectral components of the scattered wave in the regime where  $l \ll x_o$  asymptotically approaches

$$\Pi_{l^*}^{(s)} \sim \frac{1}{2} \Pi_{l^*}^{(i)} (\exp(2iNx_o) - 1), \quad l^* \ll x_o \quad (3.6-6)$$

Without much restriction (because  $x_o$  is so large), we may choose  $N$  so that  $Nx_o$  equals an integer multiple of  $\pi$ , thereby nulling out completely the contribution from this asymptotic component.

When  $l \gg x$ , it can be shown (see, for example, [10]) that

$$\xi_l^\pm(x) \rightarrow \sqrt{\frac{x}{l}} \left[ \frac{1}{2} \left( \frac{ex}{2l} \right)^l \mp i \left( \frac{2l}{ex} \right)^l \right], \quad l \gg x \quad (3.6-7)$$

Thus, the contributions from the scattering coefficients to the series in Eq. (3.3-2) attenuate rapidly with increasing  $l$  when  $l > x_o$ . We will show that the principal contributions to these series come from that regime where  $l \approx x_o$ .

### 3.7 The Sommerfeld–Watson Transformation

A conventional method for solving such slowly converging series is to use a transformation due principally to Arnold Sommerfeld [3,12]. This transformation converts a sum, such as that in Eq. (3.5-14), into an equivalent but perhaps a more rapidly converging sum in the complex plane. Here the sum is first converted into a closed-contour integral representation in the complex  $l$ -space plane. An example of this is shown in Fig. 3-9(a); the closed contour is the path  $L_1$ , which lies near the positive real axis. When this contour integration is evaluated in terms of the sum of the residues around the poles of the integrand on the real axis, it yields the original sum to be evaluated (assuming that the  $f$  function in Fig. 3-9(a) has no poles of its own on the real axis).

This contour  $L_1$  then is deformed into another closed contour  $L_2$  that excludes the poles on the real axis as interior points but encloses the poles of the integrand located elsewhere in the complex plane; in Fig. 3-9(b), these poles are shown at  $l_0, l_1, l_2, \dots$ . If the integrand is properly constituted, i.e., symmetric

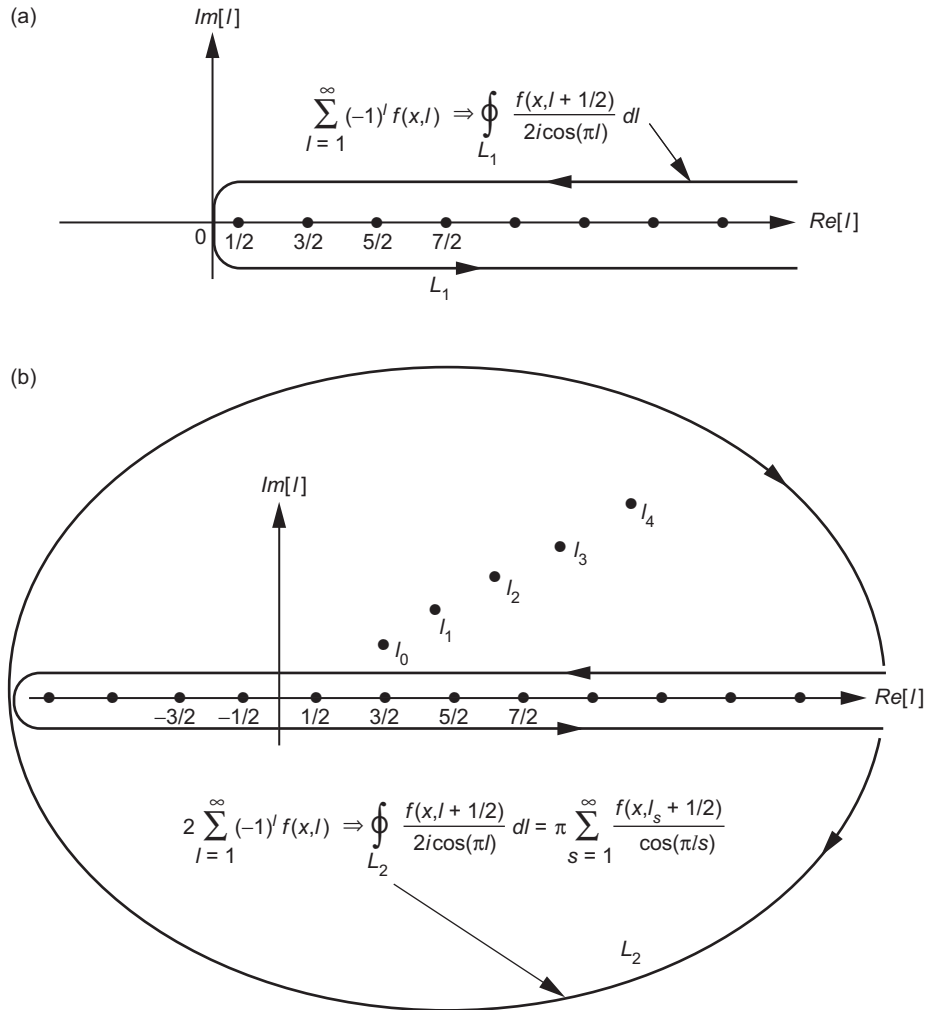


Fig. 3-9. Contour integration in the complex spectral number plane to evaluate the spectral series by summing the residues of the poles in the plane: (a) residues of the simple poles interior to the path  $L_1$  at the 1/2-integer points along the real axis are summed, and (b) equivalent contour integration around  $L_2$ , which is evaluated by summing the residues at the interior poles at  $l_0, l_1, l_2, \dots$  in the upper complex plane.

about the origin on the real axis (for this example), then the residue series from its off-real-axis poles in the complex plane may converge rapidly under certain conditions. For example, if the residues at the poles in the complex plane diminish rapidly with altitude or the number of poles is limited, then convergence by summing in the complex spectral number plane may be more efficient than summing over integer spectral number on the positive real axis. Thus, one replaces a spectral distribution of partial wavelets in real-integer  $l$

spectral number space by an equivalent sum of residue wavelets in complex  $l$ -space. This technique has been very useful in radio propagation problems [13] because the residues from the poles of the integrand located in the complex plane away from the real axis diminish rapidly for certain geometrical configurations of the emitter and receiver. The Hankel functions of the first kind, appearing in the series expressions for the scattered wave [see Eq. (3.3-2)], vanish exponentially with increasing positive altitude in complex  $l$ -space above the real axis. This approach has been used in the study of scattering and rainbow effects from spherical objects and also in resonance studies in high-energy physics (Regge poles). Appendix G provides a brief discussion of this technique.

### 3.8 Evaluating Scattering Coefficients with Asymptotic Expansions

In our problem, the situation is simpler because of the small discontinuity in refractivity that is assumed here. Moreover, the enormity of  $x_o$  allows us to use asymptotic expressions for the Bessel and Neumann functions (due to Hankel) and for the Legendre polynomials, which are relatively simple, becoming more accurate with increasing  $x_o$ . We will use a numerical integration technique aided by the stationary-phase technique to evaluate the scattering coefficients. In addition, the method of stationary phase will be used for interpretation. Use of stationary-phase concepts is instructive because the asymptotic forms for the Hankel functions and Legendre polynomials explicitly reveal the correspondence between the Mie solution to scattering from a sphere and the scalar diffraction integral formulation of the thin-screen model. They also reveal the correspondence between wave theory and geometric optics.

For large values of  $\nu = l + 1/2$ , the Hankel functions are given by asymptotic expansions in terms of the Airy functions and their derivatives [10]. Airy functions themselves are expressible in terms of Bessel functions of fractional order  $1/3$ . Inasmuch as the significant scattering coefficients arise for spectral numbers only in the neighborhood near  $\nu \approx x_o$  and because  $x_o \gg 1$ , we can truncate the asymptotic expansions for the Hankel functions, retaining only the leading term in each expression. These are given by

$$H_{\nu}^{\pm}(x) = \left( \frac{4y}{\nu^2 - x^2} \right)^{1/4} (\text{Ai}[y] \mp i \text{Bi}[y]) + O[\nu^{-5/3}] \quad (3.8-1)$$

The derivatives of the Hankel functions with respect to  $x$  are given by

$$H_{\nu}^{\pm}(x) = -\frac{2}{x} \left( \frac{\nu^2 - x^2}{4y} \right)^{1/4} (\text{Ai}'[y] \mp i \text{Bi}'[y]) + O[\nu^{-4/3}] \quad (3.8-2)$$

Here  $\text{Ai}[y]$  and  $\text{Bi}[y]$  are the Airy functions of the first and second kind, and their argument  $y$  is given by

$$y = \nu^{2/3} \xi \left[ \frac{\nu}{x} \right] \quad (3.8-3)$$

The function  $\xi[\mu]$ , which is defined to be real when  $\mu = \nu/x$  is real and positive, is given by

$$\left. \begin{aligned} \frac{2}{3} (\xi[\mu])^{3/2} &= \int_1^\mu \frac{\sqrt{w^2 - 1}}{w^2} dw = \log(\mu + \sqrt{\mu^2 - 1}) - \frac{\sqrt{\mu^2 - 1}}{\mu}, \quad \mu \geq 1 \\ \text{or} \\ \frac{2}{3} (-\xi[\mu])^{3/2} &= \int_\mu^1 \frac{\sqrt{1 - w^2}}{w^2} dw = \frac{\sqrt{1 - \mu^2}}{\mu} - \cos^{-1} \mu, \quad \mu \leq 1 \end{aligned} \right\} \quad (3.8-4)$$

Useful series expansions for  $\xi[\mu]$  and  $y$  are given by

$$\left. \begin{aligned} \xi &= \frac{\mu^2 - 1}{\mu^2} \left( \frac{3\mu^2}{2} \sum_{k=0}^{\infty} \frac{(1 - \mu^{-2})^k}{2k + 3} \right)^{2/3} \quad |\mu|^2 \geq \frac{1}{2} \\ y &= \frac{1}{4} \left( \frac{2}{\nu} \right)^{4/3} (\nu^2 - x^2) \left( 1 + \frac{2}{5} \cdot \frac{\nu^2 - x^2}{\nu^2} + \dots \right) \end{aligned} \right\} \quad (3.8-5)$$

When  $x \gg 1$ , a near-linear relationship exists between  $y$  and  $(\nu - x)$ . By expanding Eq. (3.8-4), one can show that

$$\left. \begin{aligned} y &= \left( \frac{2}{x} \right)^{1/3} (\nu - x) \left( 1 - \frac{\nu - x}{30x} + \dots \right), \\ \nu - x &= \left( \frac{x}{2} \right)^{1/3} y \left( 1 + \left( \frac{x}{2} \right)^{1/3} \frac{y}{30x} + \dots \right) \end{aligned} \right\} \quad (3.8-6)$$

These truncated series for  $y$  and  $\nu$  are very accurate when  $x \gg 1$  and  $\nu$  is in the vicinity of  $x$ .

The Airy function  $\text{Ai}[y]$  is oscillatory for negative real  $y$  and rapidly damps to zero for positive real  $y$  [see Fig. 3-10(a)].  $\text{Bi}[y]$  is also oscillatory for negative  $y$ , but it grows rapidly with positive  $y$  [see Fig. 3-10(b)]. The asymptotic forms for the Airy functions [10] applicable also for complex arguments  $z$  are given by

$$\left. \begin{aligned} \text{Ai}[-z] &\rightarrow \pi^{-1/2} z^{-1/4} \left[ \sin X - \frac{5}{48} z^{-3/2} \cos X + O[z^{-3}] \right], \quad |\text{Arg}[z]| < \frac{2\pi}{3} \\ \text{Ai}'[-z] &\rightarrow \pi^{-1/2} z^{1/4} \left[ -\cos X + \frac{7}{48} z^{-3/2} \sin X + O[z^{-3}] \right], \quad |\text{Arg}[z]| < \frac{2\pi}{3} \\ \text{Bi}[-z] &\rightarrow \pi^{-1/2} z^{-1/4} \left[ \cos X + \frac{5}{48} z^{-3/2} \sin X + O[z^{-3}] \right], \quad |\text{Arg}[z]| < \frac{2\pi}{3} \\ \text{Bi}'[-z] &\rightarrow \pi^{-1/2} z^{1/4} \left[ \sin X + \frac{7}{48} z^{-3/2} \cos X + O[z^{-3}] \right], \quad |\text{Arg}[z]| < \frac{2\pi}{3} \end{aligned} \right\} \quad (3.8-7)$$

where  $X = 2z^{3/2} / 3 + \pi / 4$ . Also,

$$\left. \begin{aligned} \text{Ai}[z] &\rightarrow \frac{\pi^{-1/2}}{2} z^{-1/4} \left[ \exp\left[-\frac{2}{3} z^{3/2}\right] \left( 1 - \frac{5}{48} z^{-3/2} + O[z^{-3}] \right) \right], \quad |\text{Arg}[z]| < \pi \\ \text{Ai}'[z] &\rightarrow \frac{-\pi^{-1/2}}{2} z^{1/4} \left[ \exp\left[-\frac{2}{3} z^{3/2}\right] \left( 1 + \frac{7}{48} z^{-3/2} + O[z^{-3}] \right) \right], \quad |\text{Arg}[z]| < \pi \\ \text{Bi}[z] &\rightarrow \pi^{-1/2} z^{-1/4} \left[ \exp\left[\frac{2}{3} z^{3/2}\right] \left( 1 + \frac{5}{48} z^{-3/2} + O[z^{-3}] \right) \right], \quad |\text{Arg}[z]| < \frac{\pi}{3} \\ \text{Bi}'[z] &\rightarrow \pi^{-1/2} z^{1/4} \left[ \exp\left[\frac{2}{3} z^{3/2}\right] \left( 1 - \frac{7}{48} z^{-3/2} + O[z^{-3}] \right) \right], \quad |\text{Arg}[z]| < \frac{\pi}{3} \end{aligned} \right\} \quad (3.8-8)$$

Equation (3.8-7) applies in particular to negative real values of  $y$ , the argument of the Airy functions. Equation (3.8-8) also applies to positive real values of  $y$ . For  $v \approx x_o$ , Eq. (3.8-6) shows that  $y \doteq (v - x_o)(2/x_o)^{1/3}$ , which is very accurate for  $x_o \gg 1$ . The Airy functions rapidly assume their respective asymptotic forms on the real axis when  $|y| > 2$ . At  $|y| = 2$ , the relative accuracy of these asymptotic forms is about 1 percent; at  $|y| = 3$ , it is 0.2 percent.

From Eqs. (3.2-8), (3.8-1), (3.8-2), and (3.8-5), it follows that when  $l \approx x$  the spherical Hankel functions may be written in terms of the Airy functions in the form

$$\left. \begin{aligned} \xi_l^\pm(x) &\sim \sqrt{\pi K_x} \left( 1 - \frac{y}{15K_x^2} + O[x^{-5/3}] \right) (\text{Ai}[y] \mp i \text{Bi}[y]) \\ \xi_l^{\pm'}(x) &\sim -\sqrt{\frac{\pi}{K_x}} \left( 1 + \frac{y}{15K_x^2} + O[x^{-5/3}] \right) (\text{Ai}'[y] \mp i \text{Bi}'[y]) \\ K_x &= \left( \frac{x}{2} \right)^{1/3}, \nu = l + 1/2 \end{aligned} \right\} \quad (3.8-9)$$

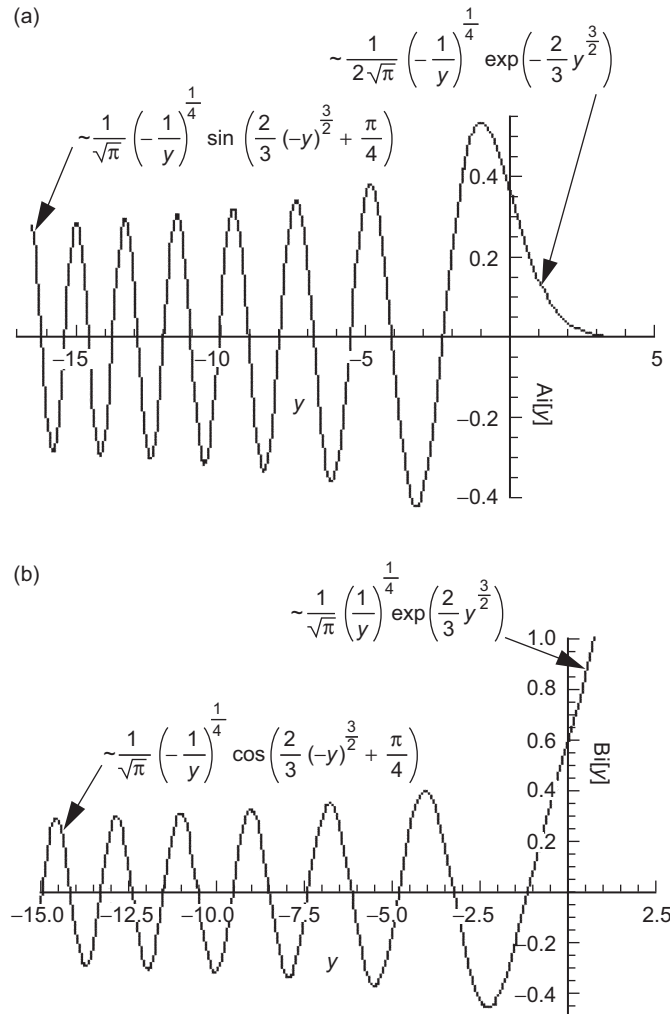


**Fig. 3-10. Airy functions and asymptotic forms: (a) Airy function of the first kind and (b) Airy function of the second kind.**

The quantity  $K_x$  appears often throughout the wave theory parts of this monograph. When  $x$  is expressed in phase units, then  $K_x$  provides the scale factor between  $y$ -space and spectral number or impact parameter space. It is a large quantity for our problem ( $K_x \sim 500$ ). In most scattering problems, the principal contributions to the synthesis of the wave come from the spectral neighborhood where  $l \approx x$ . Therefore,  $K_x$  is essentially constant over that neighborhood. When  $|l-x|/x \ll 1$ , we may drop the  $y/K_x^2$  terms in Eq. (3.8-9).

We will be interested in the asymptotic forms of the scattering coefficient quantities  $\mathcal{W}_l^\pm$  and  $\mathcal{W}_l'$ , particularly for negative  $y$  values. From Eq. (3.8-7), it follows that the negative-argument asymptotic forms for the spherical Hankel functions become

$$\left. \begin{aligned} \left\{ \begin{aligned} \xi_l^\pm(x) &\rightarrow \mp i \left( \frac{x^2}{x^2 - \nu^2} \right)^{1/4} \exp(\pm iX), \\ \xi_l^{\pm'}(x) &\rightarrow \left( \frac{x^2 - \nu^2}{x^2} \right)^{1/4} \exp(\pm iX) \end{aligned} \right\}, \quad \nu \ll x \\ X &= \sqrt{x^2 - \nu^2} - \nu \cos^{-1} \left( \frac{\nu}{x} \right) + \frac{\pi}{4}, \quad \nu = l + 1/2 \end{aligned} \right\} \quad (3.8-10)$$

or in terms of the argument  $y$  (provided that  $l \approx x$  so that  $y = K_x^{-1}(\nu - x)$  from Eq. (3.6-6) is a valid approximation) they become

$$\left. \begin{aligned} \left\{ \begin{aligned} \xi_l^\pm(x) &\rightarrow \mp i \left( \frac{K_x^2}{-y} \right)^{1/4} \exp(\pm iX), \\ \xi_l^{\pm'}(x) &\rightarrow \left( \frac{-y}{K_x^2} \right)^{1/4} \exp(\pm iX) \end{aligned} \right\}, \quad y < 0 \\ X &= \frac{2}{3}(-y)^{3/2} + \frac{\pi}{4}, \quad y = \nu^{2/3} \xi[\nu/x] \end{aligned} \right\} \quad (3.8-11)$$

For the scattering coefficients, it follows that

$$\left. \begin{aligned}
\frac{\mathcal{W}_l^\pm}{\mathcal{W}_l} &\rightarrow \left\{ \begin{aligned}
&\pm \frac{n^2(x_o^2 - \nu^2)^{1/2} - (n^2x_o^2 - \nu^2)^{1/2}}{n^2(x_o^2 - \nu^2)^{1/2} + (n^2x_o^2 - \nu^2)^{1/2}} e^{2i \begin{Bmatrix} +\hat{X} \\ -X \end{Bmatrix}}, \nu < x_o \\
&-1, \nu > x_o
\end{aligned} \right\} \\
\text{or} \\
\frac{\mathcal{W}_l^\pm}{\mathcal{W}_l} &\rightarrow \pm \frac{(-\hat{y})^{1/2} - (-y)^{1/2}}{(-\hat{y})^{1/2} + (-y)^{1/2}} e^{2i \begin{Bmatrix} +\hat{X} \\ -X \end{Bmatrix}}, y < 0
\end{aligned} \right\} \quad (3.8-12)$$

Also,

$$\left. \begin{aligned}
\mathcal{W}_l &\rightarrow \left\{ \begin{aligned}
&-i \left[ \left( \frac{n^2(x_o^2 - \nu^2)}{n^2x_o^2 - \nu^2} \right)^{1/4} + \left( \frac{n^2(x_o^2 - \nu^2)}{n^2x_o^2 - \nu^2} \right)^{-1/4} \right] e^{i(X - \hat{X})}, \nu < x_o \\
&\infty, \nu > x_o,
\end{aligned} \right\} \\
\text{or} \\
\mathcal{W}_l &\rightarrow -i \left[ \left( \frac{\hat{y}}{y} \right)^{1/4} + \left( \frac{\hat{y}}{y} \right)^{-1/4} \right] e^{i(X - \hat{X})}, y < 0
\end{aligned} \right\} \quad (3.8-13)$$

where

$$\left. \begin{aligned}
y &= \nu^{2/3} \zeta \left( \frac{\nu}{x} \right), \quad \hat{y} = \nu^{2/3} \zeta \left( \frac{\nu}{nx} \right) = y - 2NK_{x_o}^2 (1 + O[x_o^{-1}]), \\
X &= \frac{2}{3}(-y)^{3/2} + \frac{\pi}{4}, \quad \hat{X} = \frac{2}{3}(-\hat{y})^{3/2} + \frac{\pi}{4}, \quad y, \hat{y} < 0
\end{aligned} \right\} \quad (3.8-14)$$

To estimate the number of scattering terms required for  $\nu > x_o$  in the spectral summations for the field, we note from Fig. 3-10(a) that  $\text{Ai}[y]$  damps to zero rapidly for  $\nu > x_o$  and that  $\text{Bi}[y]$  grows large ( $\sim \exp(2y^{3/2}/3)$ ). We note from Eqs. (3.5-11), (3.5-15), and (3.8-13) that the rapid growth in  $\text{Bi}[y]$  for  $\nu > x_o$  drives  $|S_l|$  to zero. In fact, for  $\nu > x_o + 3(x_o/2)^{1/3}$ ,  $|S_l|$  becomes less than 0.001. Therefore, the number of spectral terms  $\Delta\nu$  greater than  $x_o$  that are required to reach  $|S_l| = 0.001$  is about 1500 in our case ( $x_o \approx 2 \times 10^8$ ) in order to achieve better than 0.1 percent accuracy. That the scattering coefficients rapidly damp to zero for  $l > x_o$  was first established 90 years ago [2]. A physical rationale of this damping in terms of spectral caustics in geometric optics is given in Section 3.11.

For  $\nu < x_o$ , the asymptotic forms for the Airy functions rapidly become sinusoidal [see Eq. (3.8-7)], which by choosing  $N$  so that  $\sin(2Nx_o) = 0$ , we know from Eq. (3.6-4) assures a zero contribution for  $\nu \ll x_o$ . However, the slight difference in arguments in the spherical Hankel functions in the  $\mathcal{W}_l$  functions in Eq. (3.5-11), which arise because of the refractivity  $N$ , creates a variable phase difference in these scattering functions that only slowly damps out for  $\nu < x_o$  (see Fig. 3-13). Much of the following discussion is concerned with the contribution of this phase difference to the computation of scattering effects. The stationary-phase technique will be used to isolate the appropriate neighborhoods in spectral number that significantly contribute to the spectral summations for the field.

### 3.9 Expressing Scattering Coefficients in Terms of Phasors

From Eqs. (3.4-3) through (3.4-7), (3.5-9), (3.5-11), (3.5-12), and (3.5-15a), or directly from Eq. (3.5-15b), it can be shown that

$$|2S_l + 1| = \left| \left( \frac{4n}{\mathcal{W}_l + \mathcal{W}_l^+} + \mathcal{W}_l^- \right) \frac{1}{\mathcal{W}_l} \right| = \left| \frac{\tilde{\mathcal{W}}_l + \mathcal{W}_l^-}{\mathcal{W}_l + \mathcal{W}_l^+} \right| = 1 \quad (3.9-1)$$

for all real values of  $l$  and  $x$ . This is a manifestation of the conservation of energy principle; all incident radiation must be scattered. We know the asymptotic form [see Eq. (3.6-4)] that  $S_l$  assumes for  $\nu \ll x_o$ . Accordingly, for real values of  $l$  and  $x$  we define the scattering phase  $\Omega^{(s)} = \Omega^{(s)}(N, x_o, \nu)$  in terms of the aggregate scattering coefficient  $S_l$  [see Eqs. (3.5-15a), (3.5-15b), and (3.5-16)] by

$$\exp(i2\Omega^{(s)}) = 2S_l + 1 = -\frac{\tilde{\mathcal{W}}_l + \mathcal{W}_l^-}{\mathcal{W}_l + \mathcal{W}_l^+} \quad (3.9-2)$$

where, in this definition,  $\Omega^{(s)}(N, x_o, \nu)$  is a real function for all real  $x$  and  $\nu = l + 1/2$ , but one has to account for its phase windup with diminishing  $\nu$ . For  $\nu > x_o$ , one concludes, using Eq. (3.8-13) and noting that  $\text{Bi}[y]$  grows exponentially large with positive  $y$ , that  $\Omega^{(s)}(N, x_o, \nu) \rightarrow 0$  as  $\nu$  exceeds  $x_o$ ; so,  $S_l \rightarrow 0$  rapidly for  $\nu > x_o$ . We also know from Eq. (3.6-4) that  $\Omega^{(s)}(N, x_o, \nu) \rightarrow Nx_o$  for  $\nu \ll x_o$ . Figure 3-11(a) shows  $\Omega^{(s)}(N, x_o, \nu)$  over its entire range. For this example,  $Nx_o$  has been set to the value  $83\pi$  exactly

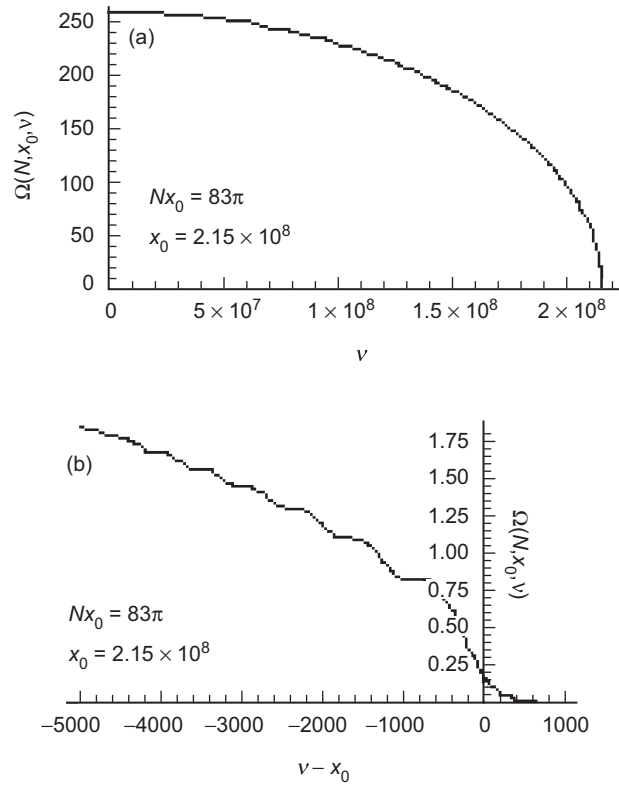


**Fig. 3-11. Scattering phase  $\Omega^{(S)}(N, x_0, \nu)$  versus spectral number: (a) variation over the entire range  $0 \leq \nu \leq x_0$  and (b) variation near  $\nu = x_0$ .**

( $N \approx 1.2 \times 10^{-6}$ ), so that the scattering coefficients ( $S_l$  and also all of the individual coefficients  $b_l^{(j)}$ ) decay to exactly zero with decreasing  $\nu$ . Figure 3-11(b) displays  $\Omega^{(S)}(N, x_0, \nu)$  in the vicinity of  $x_0$  and shows the diminishing undulations with decreasing  $\nu$  below  $x_0$ . We will see that these undulations result in additional points of stationary phase in the series summation of the scattering coefficients for a certain range of angular positions of the LEO.

Similarly, we can define  $\Omega^{(j)}(N, x_0, \nu)$  as the phase associated with the individual  $j$ th scattering coefficient  $b_l^{(j)}$ ,  $j = 0, 1, 2, \dots$ . From Eq. (3.5-11) we have

$$\left. \begin{aligned} a^{(0)} \left( i^{l-1} n \frac{2l+1}{l(l+1)} \right)^{-1} \Delta = \rho e^{i\Omega} = -\frac{2i}{\mathcal{W}_l}, \\ 2S_l^{(0)} + 1 = 2b_l^{(0)} \left( i^{l-1} \frac{2l+1}{l(l+1)} \right)^{-1} + 1 = \rho^{(0)} e^{i2\Omega^{(0)}} = -\frac{\mathcal{W}_l^-}{\mathcal{W}_l}, \\ 2S_l^{(j)} = 2b_l^{(j)} \left( i^{l-1} \frac{2l+1}{l(l+1)} \right)^{-1} \Delta = \rho^{(j)} e^{i2\Omega^{(j)}} = n \left( -\frac{\mathcal{W}_l^+}{\mathcal{W}_l} \right)^{j-1} \rho^2 e^{i\Omega} \end{aligned} \right\} (3.9-3)$$

Here the modulus  $\rho = \rho(N, x_o, \nu)$  on the transmission coefficient is variable with spectral number. It follows from Eq. (3.8-13) that

$$\rho = \left| \frac{-2i}{\mathcal{W}_l} \right| \rightarrow 2 \left( \left( \frac{\hat{y}}{y} \right)^{1/4} + \left( \frac{y}{\hat{y}} \right)^{1/4} \right)^{-1} \rightarrow 1, \quad \Omega \rightarrow \hat{X} - X, \quad y < 0 \quad (3.9-4)$$

Thus,  $\rho \rightarrow 1$  for  $\nu \ll x_o$ , and  $\rho \rightarrow 0$  for  $\nu \gg x_o$  (see Fig. 3-12). Similarly, for the external reflection it can be shown from Eq. (3.8-12) that

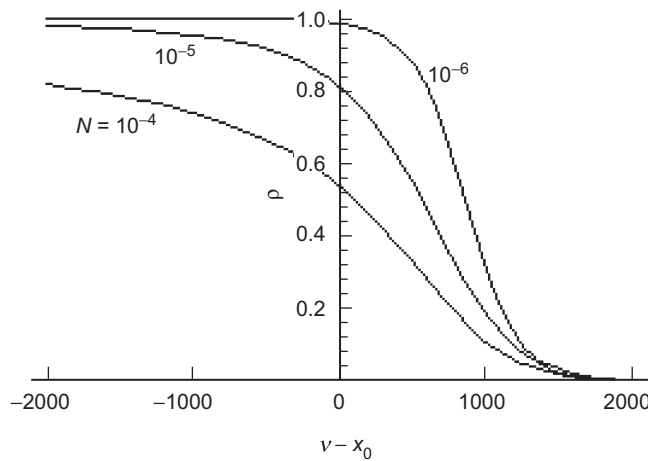


Fig. 3-12. Modulus  $\rho(N, x_0, \nu)$  of  $(2i/\mathcal{W}_l)$ .

$$\left. \begin{aligned}
 & \left\{ \begin{aligned}
 & 2i\Omega^{(0)} = \log\left(\frac{\xi_l^-(x_o)}{\xi_l^+(x_o)}\right) \rightarrow 2iX \\
 & \rho^{(0)} = \frac{|\mathcal{W}_l^-|}{|\mathcal{W}_l^+|} \rightarrow \frac{n^2(x_o^2 - v^2)^{1/2} - (n^2x_o^2 - v^2)^{1/2}}{n^2(x_o^2 - v^2)^{1/2} + (n^2x_o^2 - v^2)^{1/2}}, \quad v < x_o
 \end{aligned} \right\} \\
 & \text{or} \\
 & \rho^{(0)} \rightarrow \begin{cases} \frac{|(-\hat{y})^{1/2} - (-y)^{1/2}|}{(-\hat{y})^{1/2} + (-y)^{1/2}}, & y, \hat{y} < 0 \\ 1, & y, \hat{y} > 0 \end{cases}
 \end{aligned} \right\} \quad (3.9-5)$$

The degree  $j=0$  modulus  $\rho^{(0)}$  of the ratio  $(\mathcal{W}_l^- / \mathcal{W}_l^+)$  is reminiscent of the Fresnel reflection formulas in Eq. (3.4-1a), except that it varies in  $v$ -space rather than in impact parameter space. It rapidly approaches zero (for  $N \ll 1$ ) with decreasing  $v$  below  $x_o$ , and it rapidly approaches 1 for  $v > x_o$  (see also Fig. 3-4). Also,  $2\Omega^{(0)}$  is simply the phase difference between the incident and external reflected components of spectral number  $l$ . These scattering phasors will prove to be relevant in our stationary-phase treatment to follow.

For the aggregate scattering coefficient  $S_l$ , or its phase  $\Omega^{(s)}$ , we have the following asymptotic forms. For  $v > x_o$ , we have already noted that both  $S_l$  and  $\Omega^{(s)}$  damp to zero rapidly. For  $v < x_o$ , it follows from Eq. (3.8-12) that  $\mathcal{W}_l^\pm \rightarrow 0$  with decreasing  $v$ . Therefore, it follows from Eq. (3.8-10) that  $\text{Exp}[i2\Omega^{(s)}] = 2S_l + 1 \rightarrow -\tilde{\mathcal{W}}_l / \mathcal{W}_l$  for decreasing  $v < x_o$ . From Eq. (3.8-13), it then follows that  $\Omega^{(s)}$  becomes

$$e^{i2\Omega^{(s)}} \rightarrow -\frac{\tilde{\mathcal{W}}_l}{\mathcal{W}_l} \rightarrow e^{i2(\hat{X}-X)} = e^{i2\Omega_A}, \quad v < x_o \quad (3.9-6)$$

For  $v < x_o$ ,  $\Omega_A(N, x_o, v)$ , which is the asymptotic form of  $\Omega^{(s)}$ , is given by

$$\Omega_A = \frac{2v}{3} \left( \left( -\xi \left[ \frac{v}{nx_o} \right] \right)^{3/2} - \left( -\xi \left[ \frac{v}{x_o} \right] \right)^{3/2} \right) + O[y^{-5/2}], \quad v < x_o \quad (3.9-7)$$

or upon using the form for  $\xi[v/x_o]$  given in Eq. (3.8-4) and expanding in powers of  $N$ , one obtains

$$\Omega_A = \begin{cases} \frac{2\sqrt{2}}{3} \left[ ((1+N)x_o - \nu)^{3/2} - (x_o - \nu)^{3/2} \right], & \nu \approx \leq x_o \\ N\sqrt{x_o^2 - \nu^2} + \nu \cdot O\left[ (N\nu/x_o)^2 \right], & \nu \ll x_o \end{cases} \quad (3.9-8)$$

The value of  $2\Omega_A$  at  $\nu = x_o$  should be noted. It is  $2x_o(2N)^{3/2}/3$ , which is exactly equal to the zero point term in the expression for the phase delay  $\varepsilon(h^*)$  in the thin-screen model for the uniform refracting sphere, as given in Chapter 2, Eq. (2.8-3). We will see that  $\Omega^{(s)}$ , which corresponds to a phase retardation of the  $\nu$ th spectral component of the scattered wave, plays an important role in the correspondence between Mie scattering theory and the thin-screen model. It can be shown using Eqs. (3.8-12), (3.8-13), and (3.9-2) that  $\Omega$ ,  $\Omega^{(s)}$ , and  $\Omega^{(1)}$  converge to the same asymptotic form when  $\nu < x_o$ , that is, to  $\Omega_A$ .

Figure 3-13 displays the difference between  $\Omega^{(s)}$  and  $\Omega_A$ . The source of these undulations is due to the ratio  $(W_l^\pm / W_l)$ , which Eq. (3.8-12) shows to vanish with decreasing spectral number and with  $\nu < x_o$ . Equation (3.9-8) shows that  $\Omega_A$  and, therefore,  $\Omega^{(s)}$  approach  $Nx_o$  quadratically with decreasing  $\nu$ , as shown in Fig. 3-11(a).

Setting  $Nx_o - \Omega^{(s)} = 0.001$  to achieve a 0.1 percent accuracy level, one obtains from Eq. (3.9-8) as a lower bound  $\nu_L = \sqrt{0.002x_o/N} \approx 6 \times 10^6$  (with  $N = 1.2 \times 10^{-6}$  and  $x_o = 2.1 \times 10^8$ ). However, the range between the lower bound  $\nu_L$  and the upper bound  $x_o + \sim 1500$  is still formidable for a summation.

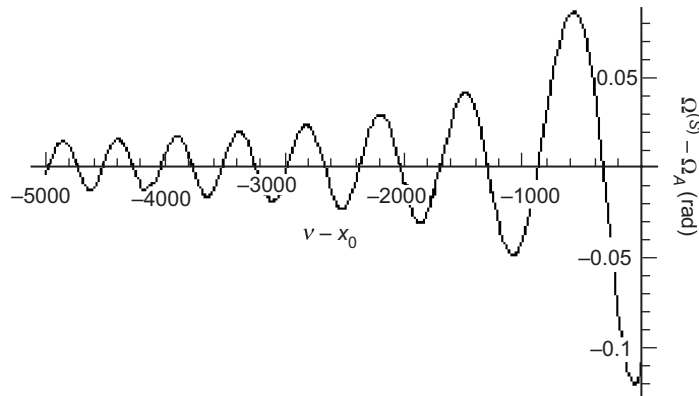


Fig. 3-13.  $\Omega^{(s)}(N, x_o, \nu) - \Omega_A(N, x_o, \nu)$  versus spectral number below  $x_o$ . The same conditions as used in Fig. 3-11.

### 3.10 Asymptotic Forms for the Hankel and Legendre Functions Evaluated at the LEO

To evaluate the spectral summations, we also need the asymptotic forms for the Hankel functions and the Legendre polynomials that are valid for large spectral numbers but evaluated at the coordinates of the LEO. The asymptotic form for the Hankel function of the first kind,  $H_\nu^+(x)$ , is given in terms of the Airy functions through Eq. (3.8-1); in this case, the radial distance of the LEO is  $x \approx 1.1x_0$ . Therefore, the argument of the Airy functions for spectral numbers near  $x_0$  is given by  $Y = \nu^{2/3}\zeta[\nu/1.1x_0] \approx -4 \times 10^4$ . Therefore, the higher-order terms in the asymptotic expansions for the Airy functions in Eq. (3.8-7) may be ignored. When  $0 \ll \nu \ll x$ , it follows from Eq. (3.8-7) that  $\xi_l^\pm(x)$  is given by

$$\left. \begin{aligned} \xi_l^\pm(x) &= \sqrt{\frac{\pi x}{2}} H_\nu^+(x) \sim \mp i \left( \frac{x^2}{x^2 - \nu^2} \right)^{1/4} \exp(\pm iY), \\ Y &= \frac{2}{3} \nu (-\zeta[\nu/x])^{3/2} + \frac{\pi}{4}, \quad \nu = l + \frac{1}{2} \end{aligned} \right\} \quad (3.10-1)$$

When  $x \gg \nu$  (as would be the case if one were observing a rainbow), it follows from Eq. (3.8-4) that  $Y \rightarrow x - \pi\nu/2$ . Then,  $\xi_l^\pm(x) \rightarrow (\mp i)^{l+1} \exp(\pm ix)$ . In our problem, however, the geocentric radial distance of the LEO is only about 10 percent larger than the radius of the refracting sphere, that is,  $x = kr \doteq 1.1kr_0$ .

From Eq. (3.8-4) it follows that  $Y$  can be written as

$$Y = \begin{cases} \sqrt{x^2 - \nu^2} - \nu \cos^{-1}\left(\frac{\nu}{x}\right) + \frac{\pi}{4}, & \nu \leq x \\ \nu \operatorname{sech}^{-1}\left(\frac{x}{\nu}\right) - \sqrt{\nu^2 - x^2} + \frac{\pi}{4}, & \nu \geq x \end{cases} \quad (3.10-2)$$

At the radial distance of the LEO, the scattering coefficients essentially will be zero for  $\nu \geq x \approx 1.1x_0$ , so we need only the expression for  $Y$  when  $\nu \leq x$ . Referring to Fig. 3-14, we see from Eq. (3.10-2) that  $Y$  may be written as

$$Y = D_\nu - \nu \left( \frac{\pi}{2} - \theta_\nu \right) + \frac{\pi}{4}, \quad \theta_\nu = \sin^{-1}\left(\frac{\nu}{x}\right), \quad D_\nu = \sqrt{x^2 - \nu^2} \quad (3.10-3)$$

where  $D_\nu$  is the distance (in phase units) of the LEO from the limb of a sphere of radius  $\nu$ , and  $\theta_\nu$  is the angle that the radius vector of length  $x$  from the

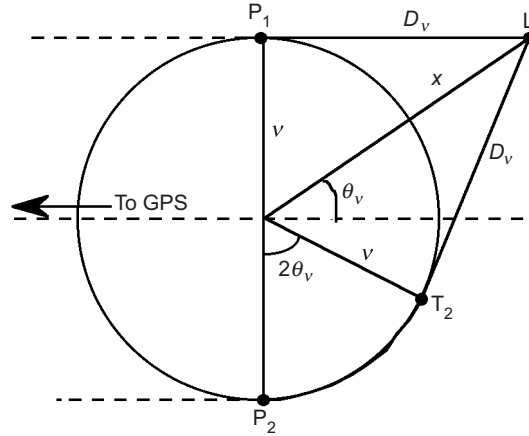


Fig. 3-14. Direct and retrograde wave geometry in spectral number space.

center of this sphere subtends. Since  $x > v > 0$ , it follows that  $0 < \theta_v < \pi/2$ . When  $v = x_o$ , we have from Eq. (3.10-3)

$$D_{x_o} = D = \sqrt{x^2 - x_o^2} = kr \cos \theta_{x_o}, \quad \theta_{x_o} = \theta_o = \sin^{-1} \left( \frac{x_o}{x} \right) \quad (3.10-4)$$

The angle  $\theta$  is the geocentric angle of the LEO position vector relative to the polar axis (the z-axis in Fig. 3-1). When  $\theta = \theta_o$ , the straight line path from the occulting GPS satellite to the LEO just grazes the surface of the sphere of radius  $r_o$ . In other words, the LEO is located on the shadow boundary of the sphere. The quantity  $D_{x_o}$  is just the distance in phase units of the LEO from the Earth's limb. Thus,  $D_{x_o}$  is the extra geometric phase term relative to the center line at  $\theta = \pi/2$  accumulated by the scattered wave upon arrival at the LEO located at  $(r, \theta_o)$ .

The asymptotic form of the Legendre polynomial for large spectral numbers is given by [10]

$$P_l^m(\cos \theta) = \frac{\Gamma[l+1]}{\Gamma[l-m+1]} \sqrt{\frac{2}{\pi l \sin \theta}} \sin \left( \nu \theta + \frac{\pi}{4} - \frac{\pi m}{2} \right) \left( 1 + O \left[ \frac{m^2}{l} \right] \right) \quad (3.10-5)$$

$m \ll l, \quad \nu = l + 1/2$

Here  $\Gamma[z]$  is the Gamma function. Equation (3.10-5) is valid except near  $\theta = 0, \pi$ . For our problem, the LEO is located at  $r = 1.1r_o$ ,  $\theta \approx 65 \text{ deg}$ , and

$\phi = 0$  during the occultation. We assume that the orbit of the LEO is circular and remains essentially invariant during the occultation. Over the few seconds of time over a shadow boundary transition,  $\theta$  will change by only several milliradians.

### 3.11 Geometric Optics Interpretation of Mie Scattering Theory

From Eqs. (3.5-14) and (3.9-2), we see that the phase of the  $l$ th spectral component of the scalar potential for the scattered wave at the LEO equals the sum of the phase  $2\Omega^{(s)}$  of the scattering coefficient  $S_l$  plus the phase of the product  $i^{l-1}\xi_l^+(x)P_l^1(\cos\theta)$ . This product pertains to the geometry of the LEO relative to the scattering sphere. It follows from Section 3.10 that this product  $i^{l-1}\xi_l^+(x)P_l^1(\cos\theta)$  contains the phasor  $i^{1/2}\exp[i\Phi^\pm(x, x_o, \nu)]$  [see Eq. (3.12-1)], where the phase function  $\Phi^\pm$  is given by

$$\Phi^\pm = D_\nu + \nu(\theta_\nu \pm \theta) + (1 \pm 1)\frac{\pi}{4} \quad (3.11-1)$$

Since  $\nu$  will be near  $x_o$  and  $\theta$  will be near  $\theta_o$ , we let  $\theta = \theta_\nu + \Delta\theta_\nu$ , where  $\Delta\theta_\nu$  marks the small departure of the angular position of the LEO from  $\theta_\nu$  during the occultation; thus,  $\nu\Delta\theta_\nu$  is the extra phase due to the displacement of  $\theta$  from  $\theta_\nu$  (see Fig. 3-15). Over the occultation region of interest, the maximum value of the magnitude of  $\Delta\theta_\nu$  never exceeds a few milliradians for  $\nu$  near  $x_o$ . Equation (3.11-1) may be written as

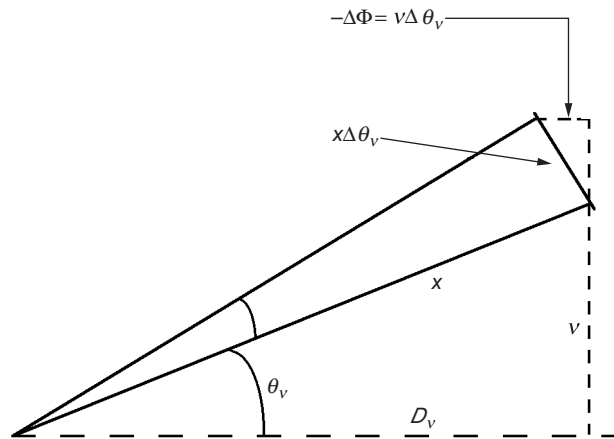


Fig. 3-15. Extra phase delay  $\Delta\Phi$  due to  $\Delta\theta_\nu$ .

$$\left. \begin{aligned} \Phi^+ &= D_\nu + 2\nu\theta_\nu + \nu\Delta\theta_\nu + \pi/2 \\ \Phi^- &= D_\nu - \nu\Delta\theta_\nu, \quad \Delta\theta_\nu = \theta - \theta_\nu \end{aligned} \right\} \quad (3.11-2)$$

Referring to Fig. 3-14, we see that  $\Phi^+$  is the phase accumulated by a wave that in a geometric optics context has traveled to the LEO, having departed tangentially from the *far* side of the sphere of radius  $\nu$ . On the other hand,  $\Phi^-$  is the phase accumulation associated with the wave that arrives from the tangent point on the near side of the sphere. Thus, the sphere of radius  $\nu$  represents in a geometric optics context a caustic surface for rays originating from the GPS satellite, dividing the region accessible to the rays ( $\nu' \geq \nu$ ) from the region that is inaccessible ( $\nu' < \nu$ ). If  $\nu > x_o$ , then no partial waves (in a geometric optics sense) with these spectral number values can interact with the surface of a sphere of radius  $x_o$ . Depicting the sphere of radius  $\nu$  as a caustic surface for partial waves of spectral number  $\nu$  provides a physical explanation for the rapid falloff in the magnitude of the scattering coefficients for  $\nu > x_o$ .

Equation (3.11-2) shows that Mie scattering theory encompasses the geometric optics concept of two partial waves traveling to the LEO: a direct wave and a retrograde wave. The line  $P_1L$  in Fig. 3-14 denotes the direct path. The line and arc labeled  $P_2T_2L$  denote the far-side ray path that arrives from the GPS satellite and tangentially impacts the sphere of radius  $\nu$  at  $P_2$ , follows a meridian arc  $P_2T_2$  of the sphere as an evanescent wave, and then departs tangentially from the sphere at  $T_2$  along a straight-line path toward the LEO. The wave also can make multiple revolutions around the sphere and then depart tangentially at  $T_2$  along the straight-line path toward the LEO. Moreover, the direct wave can make multiple revolutions as an evanescent wave and then depart at  $P_1$  for the LEO. In geometric optics, these ray paths follow Fermat's principle.

There is a body of literature [14] that uses Fermat's principle and geometric optics to calculate diffraction effects from three-dimensional objects such as a sphere. A semi-empirical parameter in this approach is the rate of decay of the amplitude of the evanescent wave as it travels circumferentially along the surface of the scattering object, spinning off tangential rays as it progresses. When the decay parameter is properly chosen, close agreement between this geometric optics approach and scattering theory based on electrodynamics usually is attained for a variety of scattering objects in addition to spheres.



Since the significant terms in the summation in Eq. (3.12-1) come from  $\nu$ -values near  $x_o$  and because  $x_o \gg 1$ , we can replace the sum with an integral. Equation (3.12-1) for the electric potential  $\Pi^{(s)}(x, \theta, \phi)$  becomes

$$\Pi^{(s)} = \frac{2E_o}{xk} \sqrt{\frac{i}{2\pi \sin \theta}} \int_0^\infty S_l(\nu \cos \theta_\nu)^{-(1/2)} (e^{i\Phi^+} - e^{i\Phi^-}) d\nu \cos \phi \quad (3.12-2)$$

where  $\cos \theta_\nu = (x^2 - \nu^2)^{1/2} / x$ . We know that  $S_l$  becomes essentially zero for  $\nu - nx_o > \sim 3(x_o / 2)^{1/3} \approx 1500$  and for  $\nu < 0.01x_o$ ; so, the limits on the integration are rather arbitrary so long as they exceed these bounds. For convenience we set them equal to 0 and  $\infty$ .

One can make a similar conversion of the series for the scattered electric field into an integral form. One applies the curl operations given in Eq. (3.2-2),  $\nabla \times \nabla \times ({}^e \Pi \mathbf{r}) = (2 + \mathbf{r} \cdot \nabla) \nabla {}^e \Pi - \mathbf{r} \nabla^2 ({}^e \Pi)$  for a TM wave to the scalar potential series in Eq. (3.5-14) for the scattered wave evaluated at the LEO. One obtains for the radial component in the plane  $\phi = 0$  and at the point  $(r, \theta)$

$$E_r^{(s)} = \frac{E_o}{x^2} \sum_{l=1}^\infty S_l i^{l-1} (2l+1) \xi_l^+(x) P_l^1(\cos \theta) + O[N] \quad (3.12-3)$$

and for the in-plane transverse component

$$E_\theta^{(s)} = -\frac{E_o}{x} \sum_{l=1}^\infty i^{l-1} \frac{2l+1}{l(l+1)} \left. \begin{aligned} & \times \left( {}^e S_l \xi_l^{l'+} (x) P_l^{l'}(\cos \theta) \sin \theta - {}^m S_l i \xi_l^{l'+} (x) \frac{P_l^1(\cos \theta)}{\sin \theta} \right) + O[N] \end{aligned} \right\} \quad (3.12-4)$$

For Legendre polynomials of high order, it is readily shown that  $|P_\nu''| \sim \nu |P_\nu'| \sim \nu^2 |P_\nu|$ . Since  $\nu \sim x_o \gg 1$ , Eq. (3.12-4) can be simplified by dropping the lower derivative term and, therefore, the contributions from the magnetic terms.

Assembling all of the asymptotic forms for these series and converting from a sum to an integral, we obtain for the radial component  $E_r^{(s)}(r, \theta)$  of the scattered wave

$$E_r^{(s)} = E_o \sqrt{\frac{1}{2\pi i x \sin \theta}} \int_0^\infty S_l \left( \frac{\sin^3 \theta_\nu}{\cos \theta_\nu} \right)^{1/2} 2(e^{i\Phi^+} - e^{i\Phi^-}) d\nu \quad (3.12-5)$$

and for the  $\hat{\theta}$  component  $E_\theta^{(s)}(r, \theta)$

$$E_{\theta}^{(s)} = E_o \sqrt{\frac{1}{2\pi i x \sin \theta}} \int_0^{\infty} S_l (2 \sin 2\theta_v)^{1/2} (e^{i\Phi^+} + e^{i\Phi^-}) d\nu \quad (3.12-6)$$

Equations (3.12-5) and (3.12-6) provide the basic spectral representation of the scattered wave. We use these forms extensively in the subsequent discussions. Since the significant scattering contributions to the integrals in Eqs. (3.12-5) and (3.12-6) come mostly from where  $\nu \approx x_o$  and  $\theta_v \approx \theta_o$ , it follows to a first approximation that  $E_{\theta}^{(s)} \approx E_r^{(s)} \cot \theta_o$ , which corresponds to a plane wave directed along the z-axis at the LEO position of  $(r, \theta)$ . It is the small deviations in which we are interested. We can replace  $S_l$  in these integrals with  $S_l^{(j)}$  from Eq. (3.9-3) to obtain the expressions for the  $j$ th-degree scattered wave.

### 3.13 Interpreting Scattering Using the Stationary-Phase Technique

We shall evaluate the integrals in Eqs. (3.12-5) and (3.12-6) as a function of the position of the LEO by numerical integration aided by the stationary-phase technique, and we outline in Appendix G how these integrals can be calculated by using the Sommerfeld–Watson transformation. However, the stationary-phase concept provides valuable insights and enables a comparison with the thin-screen model for Fresnel diffraction.

#### 3.13.1 Stationary Phase

Contributions to the scattering integrals in Eqs. (3.12-5) and (3.12-6) come from neighborhoods where their aggregate phasor is stationary. Let  $\Psi^{(S)} = \Psi^{(S)}(x, \theta, N, x_o, \nu)$  be the aggregate phase, defined by

$$\Psi^{(S)} = 2\Omega^{(S)} + \Phi^- \quad (3.13-1)$$

where the scattering phase  $2\Omega^{(S)}$  is defined by Eq. (3.9-2) and the geometric phase delay  $\Phi^-$  is given by Eq. (3.11-1). Similarly, we can define  $\Psi^{(j)} = 2\Omega^{(j)} + \Phi^-$  as the phase associated with the  $j$ th-degree scattered wave, where  $\Omega^{(j)}$  is defined in Eq. (3.9-3). We note again that  $\Phi^-$  is just the extra phase accumulated by a wave arriving at the LEO from the near-side tangent point of the sphere of radius  $\nu$ , whilst  $\Phi^+$  is the phase accumulated by the wave from the far-side tangent point  $(+\pi/2)$ . For limb sounders, we can dispense with the  $\Phi^+$  component because when  $x_o$  is very large it never yields stationary-phase points. In  $\Phi^+$ , the angles  $\theta$  and  $\theta_v$  add [see Eq. (3.11-1)], resulting in an enormously large rate of phase change with changing  $\nu$  and, therefore, a negligible contribution to the scattering integrals. Whereas for  $\Phi^-$ ,

which involves the difference in these angles, stationary-phase points for  $\Psi^{(S)}$  or for  $\Psi^{(j)}$  are realizable.

The integrals in Eqs. (3.12-5) and (3.12-6) involve a convolution of the phasor  $\exp(i\Phi^-)$  with a kernel of the form  $(\exp(2i\Omega)-1)$  times a slowly varying factor,  $(\sin\theta_v \cos\theta_v)^{1/2}$  for  $E_\theta^{(s)}$ , and  $(\sin^3\theta_v / \cos\theta_v)^{1/2}$  for  $E_r^{(s)}$ . These phasor terms may be written as the difference:  $2S_l \exp(i\Phi^-) = \exp[i(2\Omega^{(S)} + \Phi^-)] - \exp(i\Phi^-)$ . Here the first integral uses the phasor  $\exp(i\Psi^{(S)})$ , and the second integral uses only the phasor  $\exp(i\Phi^-)$ . The latter integral involving only  $\exp(i\Phi^-)$  (that is, the “-1” part of  $2S_l$  [see Eq. (3.9-2)] and, therefore, the part that is independent of the scattering) is easily evaluated. We see that the phasor in the integrand will be stationary when  $\partial\Phi^- / \partial v = 0$ . Using Eq. (3.11-1), one can show that

$$\left. \begin{aligned} \frac{\partial\Phi^-}{\partial v} &= \theta_v - \theta \\ \frac{\partial^2\Phi^-}{\partial v^2} &= \frac{1}{D_v} \end{aligned} \right\} \quad (3.13-2)$$

It follows that  $\partial\Phi^- / \partial v = 0$  when  $\theta_v = \theta$ , that is, when  $v = v^* = x \sin\theta$ ; at this stationary-phase point,  $D_v = D_{v^*} = x \cos\theta$  and  $\Phi^- = \Phi_{v^*}^-$ , which is the result to be expected from a geometric optics point of view. If  $\Phi^-$  is expanded in a quadratic Taylor series about  $v = v^*$ , one obtains  $\Phi^- \doteq \Phi_{v^*}^- + (v - v^*)^2 / 2D_{v^*}$ . In the stationary-phase technique, the quantities varying slowly with spectral number are evaluated at the stationary-phase point and moved outside of the integral, which leaves only the quadratic term. It follows that the contribution to the scattering integral for  $E_\theta^{(s)}$  in Eq. (3.12-6) from only the phasor  $\text{Exp}[i\Phi^-]$  may be written in terms of a Fresnel integral in the form

$$\left. \begin{aligned} E_o \sqrt{\frac{1}{2\pi i x \sin\theta}} \int_0^\infty (\sin\theta_v \cos\theta_v)^{1/2} \exp(i\Phi^-) dv &\doteq \\ E_o \sqrt{\frac{\sin\theta_{v^*} \cos\theta_{v^*}}{2\pi i x \sin\theta}} e^{iD_{v^*}} \int_0^\infty \exp\left(i \frac{(v - v^*)^2}{2D_{v^*}}\right) dv &= \\ \frac{E_o}{\sqrt{2i}} \cos\theta e^{ix \cos\theta} \times \int_{w^* \approx -\infty}^\infty \exp\left(i\pi \frac{w^2}{2}\right) dw &= E_o \cos\theta e^{ix \cos\theta} \end{aligned} \right\} \quad (3.13-3)$$

The lower limit  $w^* = -v^* / (\pi D_{v^*})^{1/2}$  in the last integral is sufficiently large ( $\approx -10^4$ ) that one effectively obtains a complete complex Fresnel integral, which equals  $1+i = (2i)^{1/2}$ . The contribution of  $\exp(i\Phi^-)$  in Eq. (3.12-5) to  $E_r^{(s)}$  is

$$E_o \sqrt{\frac{1}{2\pi i x \sin \theta}} \int_0^\infty \left( \frac{\sin^3 \theta_v}{\cos \theta_v} \right)^{1/2} e^{i\Phi^-} dv \doteq E_o \sin \theta e^{ix \cos \theta} \quad (3.13-4)$$

The forms in Eqs. (3.13-3) and (3.13-4) are exactly the components for the phase and amplitude that one obtains in the absence of the scattering sphere for a plane harmonic wave traveling in a vacuum along the positive z-axis,<sup>3</sup> i.e., along  $z = r \cos \theta$ .

It follows that the total electric field (scattered plus incident,  $\mathbf{E}^{(i)} + \mathbf{E}^{(s)}$ ) is given from Eqs. (3.12-5) and (3.12-6) with  $2S_l$  replaced by the phasor  $\exp(i2\Omega^{(s)})$ ; that is, we drop the “-1” part of  $2S_l$  in calculating the total field at  $(r, \theta)$ . We recall from Eqs. (3.9-1) and (3.9-2) that the aggregate scattering coefficient can be written in terms of its phasor as  $2S_l = \exp(i2\Omega^{(s)}) - 1$ . Dropping the -1 term (and dropping the  $\Phi^+$  term), it follows that the total field at the LEO can be written as

$$\left. \begin{aligned} E_r^{(i)} + E_r^{(s)} &= E_o \sqrt{\frac{1}{2\pi i x \sin \theta}} \int_0^\infty \left( \frac{\sin^3 \theta_v}{\cos \theta_v} \right)^{1/2} e^{i(2\Omega^{(s)} + \Phi^-)} dv \\ E_\theta^{(i)} + E_\theta^{(s)} &= E_o \sqrt{\frac{1}{2\pi i x \sin \theta}} \int_0^\infty \left( \frac{\sin 2\theta_v}{2} \right)^{1/2} e^{i(2\Omega^{(s)} + \Phi^-)} dv \end{aligned} \right\} \quad (3.13-5)$$

Here  $\Omega^{(s)}$  is given in Eq. (3.9-2) or Eq. (3.9-3), and  $\Phi^-$  is given in Eq. (3.11-1);  $\theta_v$  is defined in Eq. (3.10-3) and also shown in Fig. 3-14.

<sup>3</sup> This can also be seen by substituting the asymptotic forms for  $\xi_l^\pm$  and  $P_l(\cos \theta)$  into Bauer's identity in Eq. (3.2-3) for the incident plane wave. Converting this series into an integral and retaining only phasor terms for which stationary values are physically realizable (i.e.,  $\theta_v$  must be in the range  $0 \leq \theta_v \leq \pi/2$  because the spectral number must be positive,  $0 < v \leq x_o \approx x/1.1$ ), one obtains

$$\exp(ikz) \doteq (2\pi i x \sin \theta)^{-1/2} \int_0^\infty \sqrt{\tan \theta_v} \exp\left[i\left(x \cos \theta_v - v(\theta_v - \theta)\right)\right] dv$$

Upon applying the stationary-phase technique to this integral, one obtains  $\exp(ikz) \doteq \exp(ix \cos \theta)$ . Only the  $\xi^+$  term in Eq. (3.2-3) [see Eq. (3.3-1)] provides a stationary-phase contribution when  $0 \ll \theta \ll \pi/2$  (i.e.,  $\theta$  is well into the first quadrant); only the  $\xi^-$  term contributes when  $\pi/2 \ll \theta \ll \pi$ .

### 3.13.2 Comparison with Diffraction from a Knife-Edge

It will be useful for comparison with thin-screen results to rewrite the scattering integrals in Eqs. (3.12-5) and (3.12-6) (dropping  $\Phi^+$ ) in the form

$$\begin{Bmatrix} E_r^{(s)} \\ E_\theta^{(s)} \end{Bmatrix} = \begin{Bmatrix} I_r + J_r \\ I_\theta + J_\theta \end{Bmatrix} \quad (3.13-6)$$

$$\begin{Bmatrix} I_r \\ I_\theta \end{Bmatrix} = E_o \sqrt{\frac{1}{2\pi i x \sin \theta}} \left[ \int_0^{x_o} \begin{Bmatrix} (\sin^2 \theta_v \tan \theta_v)^{1/2} \\ (\sin \theta_v \cos \theta_v)^{1/2} \end{Bmatrix} e^{i\Psi^{(s)}} dv \right. \\ \left. + \int_{x_o}^{\infty} \begin{Bmatrix} (\sin^3 \theta_v / \cos \theta_v)^{1/2} \\ (\sin \theta_v \cos \theta_v)^{1/2} \end{Bmatrix} dv (e^{i\Psi^{(s)}} - e^{i\Phi^-}) \right] \quad (3.13-7)$$

and

$$\begin{Bmatrix} J_r \\ J_\theta \end{Bmatrix} = -E_o \sqrt{\frac{1}{2\pi i x \sin \theta}} \left[ \int_0^{x_o} \begin{Bmatrix} (\sin^2 \theta_v \tan \theta_v)^{1/2} \\ (\sin \theta_v \cos \theta_v)^{1/2} \end{Bmatrix} e^{i\Phi^-} dv \right] \quad (3.13-8)$$

The  $J$  integrals in Eq. (3.13-8) essentially provide the scattering that one would obtain from a knife-edge, a result that Arnold Sommerfeld obtained 100 years ago [15]. This can be seen by evaluating Eq. (3.13-8) using the stationary-phase technique in the same manner as was used to obtain Eq. (3.13-3); thus, we obtain

$$\begin{Bmatrix} J_r \\ J_\theta \end{Bmatrix} \doteq -E_o \exp(ix \cos \theta) \begin{Bmatrix} \sin \theta \\ \cos \theta \end{Bmatrix} \left. \begin{Bmatrix} \frac{1}{1+i} \int_{\tilde{w}}^{\infty} \exp\left(i \frac{\pi}{2} w^2\right) dw, \\ \tilde{w} \doteq (\theta - \theta_o) \sqrt{x \cos \theta / \pi} \end{Bmatrix} \right\} \quad (3.13-9)$$

On the other hand, consider the Fresnel diffraction from a semi-infinite plane mounted perpendicular to the  $z$ -axis and at a horizontal distance (in phase units)  $D = x \cos \theta$  from the LEO (see Fig. 3-16). The upper boundary of the plane is located at a distance  $x_o$  above the  $z$ -axis. From the Rayleigh–Sommerfeld formulation of Fresnel diffraction for this knife-edge (see Chapter 2, Eq. (2.5-1), where now  $D$ ,  $h$ , and  $h_{LG}$  are in phase units), we have

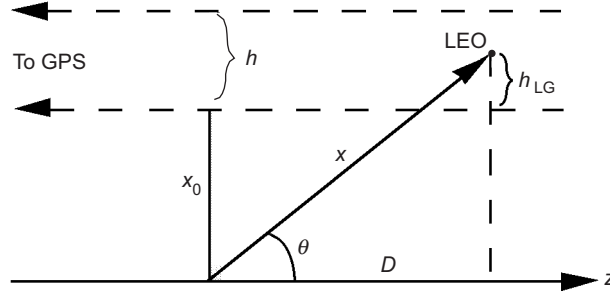


Fig. 3-16. Thin-screen geometry for a knife-edge mounted perpendicular to  $\hat{z}$ . A GPS satellite at infinite distance in the negative  $\hat{z}$ -direction.

$$\begin{Bmatrix} E_r^{(S)} \\ E_\theta^{(S)} \end{Bmatrix}_{\text{knife-edge}} = E_o \begin{Bmatrix} \sin \theta \\ \cos \theta \end{Bmatrix} \sqrt{\frac{1}{2\pi i D}} \int_0^\infty \exp\left(i\left(D + \frac{(h - h_{\text{LG}})^2}{2D}\right)\right) dh \quad (3.13-10)$$

Noting from Fig. 3-16 that  $h_{\text{LG}} = x(\sin \theta - \sin \theta_o) \doteq x(\theta - \theta_o) \cos \theta$  and that  $D = x \cos \theta = D_{v^*}$ , we convert the integral in Eq. (3.13-10) into a Fresnel integral to obtain the identity between Eqs. (3.13-9) and (3.13-10). In certain specific examples to follow, the difference between Mie scattering from a sphere and the diffraction from the thin-screen knife-edge are borne by the  $I$  integrals in Eq. (3.13-7).

### 3.13.3 Stationary-Phase Points for the Scattering Integrals

For the contribution to the scattering integrals in Eq. (3.13-5) from the phasor  $\text{Exp}[i\Psi^{(S)}]$ , the main contributions come from neighborhoods around points in spectral number space where  $\partial\Psi^{(S)}/\partial\nu = 2\partial\Omega^{(S)}/\partial\nu + \partial\Phi^-/\partial\nu = 0$ . To compute  $\partial\Psi/\partial\nu$ , we will need explicit forms for  $\partial\xi_v^\pm/\partial\nu$ . Recalling that  $\nu = \mu x$  in the asymptotic forms for  $\xi_v^\pm(x)$  [Eqs. (3.2-8), (3.8-1), and (3.8-2)], we have

$$\begin{aligned} \xi_v^\pm &\equiv \left( \frac{\partial \xi_v^\pm}{\partial x} \right)_\nu = \left( \frac{\partial \xi_v^\pm}{\partial \mu} \right)_\nu \left( \frac{\partial \mu}{\partial x} \right)_\nu \\ \left( \frac{\partial \xi_v^\pm}{\partial \nu} \right)_x &= \left( \frac{\partial \xi_v^\pm}{\partial \mu} \right)_\nu \left( \frac{\partial \mu}{\partial \nu} \right)_x + \left( \frac{\partial \xi_v^\pm}{\partial \nu} \right)_\mu \end{aligned} \quad (3.13-11)$$

where  $\mu = \nu/x$ . From the asymptotic forms in Eqs. (3.8-1) and (3.8-2), it follows that

$$\left(\frac{\partial \xi_{\nu}^{\pm}}{\partial \nu}\right)_x = -F(\mu) \left(\frac{\partial \xi_{\nu}^{\pm}}{\partial x}\right)_{\nu} + O[x^{-1}] \quad (3.13-12)$$

where  $F(\mu)$  is defined by

$$F(\mu) = \frac{\tan^{-1}\left(\sqrt{\mu^{-2} - 1}\right)}{\sqrt{1 - \mu^2}} \quad (3.13-13)$$

Note that  $F(\mu)$  also is real for  $\mu > 1$ . Similarly, one obtains

$$\left(\frac{\partial \xi_{\nu}^{\pm'}}{\partial \nu}\right)_x = \frac{\partial^2 \xi_{\nu}^{\pm}}{\partial x \partial \nu} = G(\mu) \xi_{\nu}^{\pm} + O[x^{-1}] \quad (3.13-14)$$

where

$$G(\mu) = \sqrt{1 - \mu^2} \tan^{-1}\left(\sqrt{\mu^{-2} - 1}\right) \quad (3.13-15)$$

Here  $G(\mu)$  also is real for  $\mu > 1$ .

From these expressions, it follows from Eq. (3.5-11) that the partial derivatives of the Wronskian forms are given by

$$\begin{aligned} \left(\frac{\partial \mathcal{W}_{\nu}}{\partial \nu}\right)_x = N \left[ (F(\mu) + \mu F'(\mu)) \xi_{\nu}^{+}(x_o) \xi_{\nu}^{-}(nx_o) \right. \\ \left. + (\mu G'(\mu) - G(\mu)) \xi_{\nu}^{+}(x_o) \xi_{\nu}^{-}(nx_o) \right] + O[(N\mu)^2] \end{aligned} \quad (3.13-16)$$

and similarly for  $(\partial \mathcal{W}_{\nu}^{\pm} / \partial \nu)_x$ . Here  $\mu_o = 1$ . With these partial derivatives for the Wronskian forms, it is possible to write an explicit expression for  $\partial \Omega^{(S)} / \partial \nu$  and also for any one of the individual  $j$ th-degree scattering phases  $\partial \Omega^{(S_j)} / \partial \nu$ ,  $j = 0, 1, 2, \dots$ , as given by Eqs. (3.9-2) and (3.9-3). Thus, we have all the parts assembled to study the behavior of  $\partial \Psi^{(S)} / \partial \nu$  and  $\partial \Psi^{(S_j)} / \partial \nu$ .

Figure 3-17 shows the variation of  $\Psi^{(S)}(N, x, \theta, x_o, \nu)$  with spectral number for specific values of the LEO angular coordinate  $\theta_o - \theta$ . These correspond to orbital positions ranging from 1.5 to 7 km into the geometric shadow of the sphere of radius  $r_o$ . Two different refractivity values,  $Nx_o = 83\pi$  and

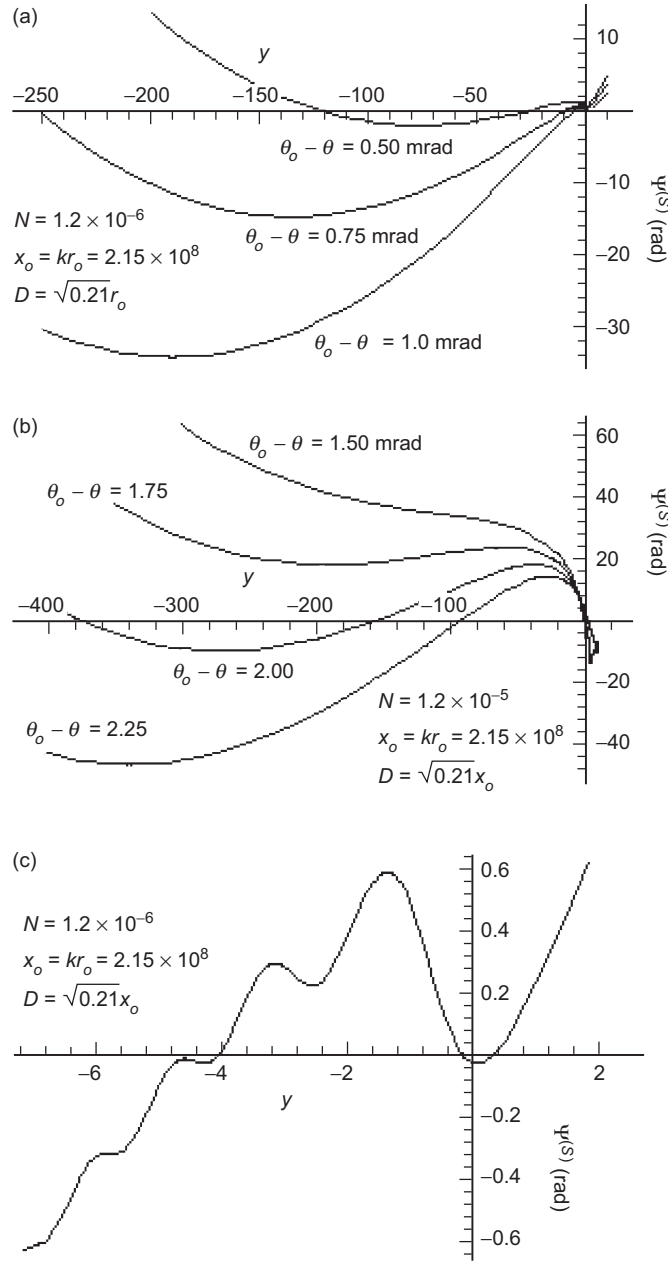


**Fig. 3-17. Scattering phase function versus spectral number for different LEO orbital positions: (a) in the asymptotic regime with  $Nx_0 = 83\pi$ , (b) in the asymptotic regime with  $Nx_0 = 830\pi$ , and (c) near  $x_0$  with  $Nx_0 = 83\pi$ ,  $\theta - \theta_0 = -1.0$ .**

$Nx_o = 830\pi$ , are used in Figs. 3-17(a) and 3-17(b). The abscissa is given in terms of the “dimensionless” spectral number difference  $y$ , which is the argument of the Airy functions and which in turn is given in terms of the difference between the spectral number  $\nu$  and radial coordinate  $x_o$ . For small values of  $y$ , it follows from Eq. (3.8-6) that

$$y \doteq K_{x_o}^{-1}(\nu - x_o), \quad \nu \doteq x_o + K_{x_o} y, \quad K_{x_o} = \left(\frac{x_o}{2}\right)^{1/3} \quad (3.13-17)$$

For  $\theta - \theta_o < 0$ , we will show later that the locations of the principal stationary-phase points lying in the regime where the negative-argument asymptotic forms for the Airy functions apply are given by the positive real roots to the cubic polynomial  $P[\xi]$

$$\left. \begin{aligned} \xi^3 + K_{x_o}^{-1} D(\theta - \theta_o) \xi + 2DN + O[N^2] &= 0, \\ y = -\xi^2, \quad D = kr \cos \theta_o \end{aligned} \right\} \quad (3.13-18)$$

For example, Fig. 3-17(a) shows that the stationary values of  $\Psi^{(S)}$  with  $Nx_o = 83\pi$  and  $\theta - \theta_o = -1$  mrad are located at  $y \cong -190$  and  $y \cong -1.5$ . The more negative point is located near where the  $-\partial\Phi^-/\partial\nu$  curve crosses zero. We also will show later that these points yield the phase delay and bending predicted by geometric optics for the degree  $j=1$  scattered wave (see Fig. 3-2), without accounting for rays arising from external or internal reflections. Figure 3-17(b) shows  $\Psi^{(S)}$  for  $Nx_o = 830\pi$ ; the stationary points occur deeper into the geometric shadow because the refractivity is larger and the refractive bending greater. The contribution of the more negative stationary-phase point dwarfs (for the magnitudes of  $Nx_o$  used in these figures) the combined contribution from the less negative point as well as the contributions from higher-degree scattered waves. Their effect is shown in Fig. 3-17(c), which displays  $\Psi^{(S)}$  versus spectral number in the vicinity of  $x_o$  for the same conditions used in Fig. 3-17(a) with  $\theta - \theta_o = -1$  mrad. We see that the predicted stationary-phase point here ( $y \cong -1.5$ ) based on asymptotic theory [Eq. (3.13-18)] is located among a complex of such points. This complex arises because the Airy functions depart significantly from their negative argument asymptotic forms in this region.

Figure 3-18 shows the points for spectral numbers in the vicinity of  $x_o$  where  $\partial\Psi^{(S)}/\partial\nu = 0$ . These are the intersections of the  $2\partial\Omega^{(S)}/\partial\nu$  curve with the  $-\partial\Phi^-/\partial\nu$  curve [the very slightly negatively sloped line denoted as

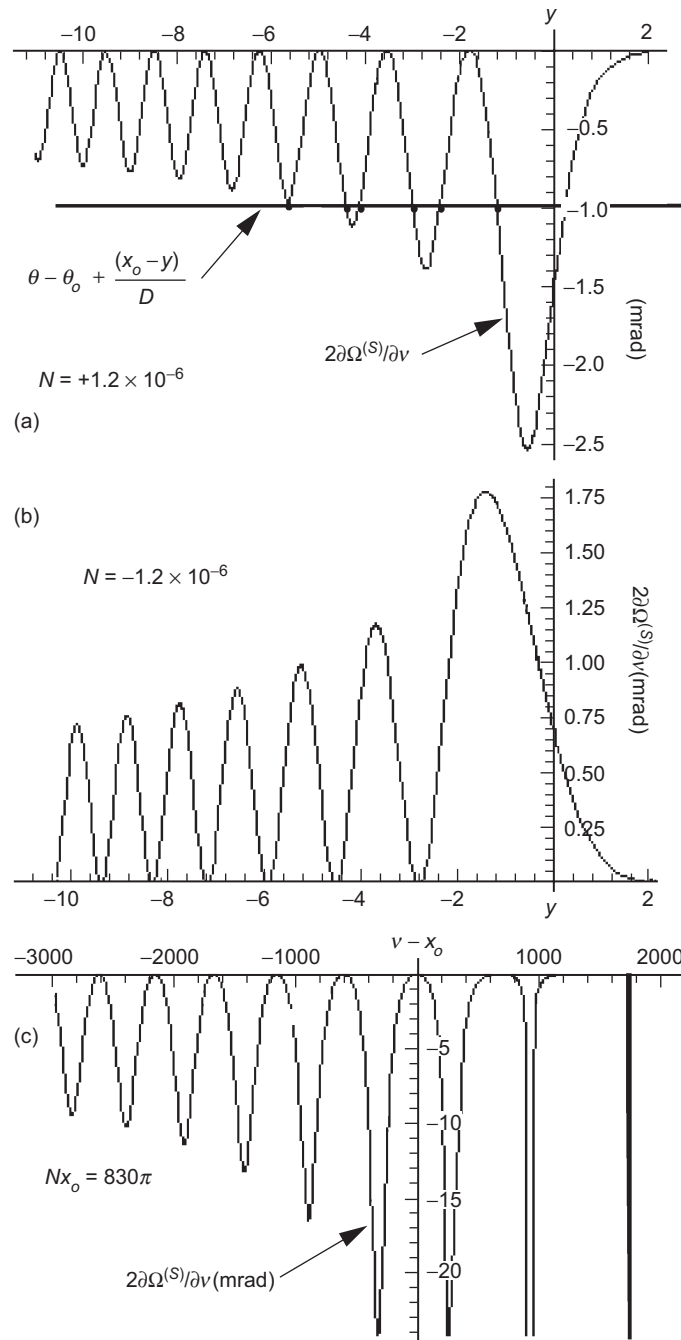


**Fig. 3-18. Stationary phase points for the total scattering integral near  $\nu = x_0$ :** (a)  $Nx_0 = +83\pi$ , (b) near  $Nx_0 = -83\pi$ , and (c)  $Nx_0 = 830\pi$ . Points occur at intersections of the  $2\partial\Omega^{(S)}/\partial\nu$  and  $\partial\Phi^-/\partial\nu$  curves.

$\theta - \theta_o + (x_o - \nu)/D$  in Fig. 3-18(a)]. The contributions to the scattering integral from the stationary points in the immediate vicinity of  $x_o$  (and shown in Fig. 3-18) are the vestigial effects (because  $N$  is so small) from higher-degree scattering; their contribution is very small compared to that from the degree  $j=1$  wave. The dominant stationary-phase point providing most of the contribution to the scattering integral is off-scale in this figure ( $y \approx -190$ ). As the occultation evolves in time, the near-horizontal line in Fig. 3-18(a) will migrate downward (for an immersion) at a rate of roughly 1 mrad/s. For  $\theta - \theta_o > 0$ , no stationary-phase points occur, but near-stationary points will become more pronounced as the LEO enters the geometric shadow zone and  $\theta - \theta_o$  becomes more negative; the neighborhoods in  $\nu$ -space about these near-stationary points will contribute to the scattering integrals. The asymptotic form for the  $2\partial\Omega^{(S)}/\partial\nu$  curve is easily obtained from Eqs. (3.8-12) and (3.9-2).

Figure 3-18(b) is similar to Fig. 3-18(a) except that the refractivity is negative and the  $-\partial\Phi^-/\partial\nu$  curve has been omitted. For  $N > 0$ , Fig. 3-18(a) shows that diffraction effects will begin rather abruptly as  $\theta - \theta_o \rightarrow 0^+$  and that they taper off more gradually as  $\theta - \theta_o$  becomes more negative. The reverse is true in Fig. 3-18(b), where  $N < 0$ . One sees these same characteristics in the scalar diffraction/thin-screen model. (For examples, see Chapter 2, Fig. 2-11.) The extent in  $\theta$ -space over which the principal diffraction effects will prevail is about 3 mrad for  $N = +1.2 \times 10^{-6}$  and about 2 mrad for  $N = -1.2 \times 10^{-6}$ , the former being close to the extent shown in Chapter 2, Figs. 2-17 and 2-18, for the Fresnel effects in phase and amplitude, as predicted by the thin-screen model for the same values of the parameters  $N$ ,  $r_o$ , and  $\lambda$ . When  $\theta - \theta_o = 0$  exactly, it marks the edge of the geometric shadow zone, and we can see from Fig. 3-18 that results from Mie scattering theory will depend on the curvature in the  $\partial\Phi^-/\partial\nu$  curve to avoid numerical integration difficulty here due to slow convergence with decreasing spectral number.

### 3.13.4 Vestigial Rainbow Effects

What has become of the rainbow effects in Mie scattering theory? For degree  $j=2$ , these are predicted by geometric optics to be most pronounced around  $\theta - \theta_o = -3.5\sqrt{2N}$  [see Eq. (3.4-9)] or at about  $-5.4$  mrad for  $N = 83\pi / x_o = 1.2 \times 10^{-6}$ . Figure 3-17 shows that they and the other higher-degree caustics have been almost completely washed out when all of the scattering degrees are summed up. This is due to the relatively small size of  $N(r_o/\lambda)^{2/3}$  [ $\sim 0.1$  in Fig. 3-17(a) and  $\sim 1$  in Fig. 3-17(b)] and the relatively large size of the first Fresnel zone. The caustic surfaces within the sphere for

$j \geq 2$  are all crowded into a region below the surface of the sphere that is only a few meters thick, much smaller than the first Fresnel zone and, therefore, washed out when observed at a distance by the LEO. By contrast, for a raindrop observed in the visual spectrum,  $N(r_o/\lambda)^{2/3} \sim 100$ . Moreover, rainbows are observed from afar spread over a cloud of coherently scattering raindrops, which has a spatial extent that is much larger than the first Fresnel zone.

Figures 3-19(a) and 3-19(b) show  $\partial\Omega^{(S_j)}/\partial\nu$  versus  $\nu - x_o$  for the individual scattered wave of degree  $j = 2$  for  $Nx_o = 83\pi$  and  $Nx_o = 830\pi$ . The stationary points in these figures define points where  $\partial^2\Psi^{(S_2)}/\partial\nu^2 = 0$ , the analog of a caustic surface but in  $\nu$ -space rather than  $h$ -space. These figures show the potential for brightening when  $\theta - \theta_o \approx -3.5\sqrt{2N}$ , which these figures place at roughly the correct scattering angle [ $-6$  to  $-8$  mrad in Fig. 3-19(a)]. However, the situation is more complicated because two caustics rather than one occur in  $\nu$ -space in Mie scattering theory, and the rays at these caustic contact points interfere with each other. Moreover, these contributions tend to be swamped by the effects of the dominant scattering coefficients  $b^{(0)}$  and  $b^{(1)}$  when  $N$  is small. As  $N$  grows larger, the caustic features at  $\partial^2\Psi^{(S_2)}/\partial\nu^2 = 0$  become prominent and isolated.

As  $N$  is set to progressively larger values, the stationary-phase points near the shadow boundary become increasingly complex. Figure 3-18(c) shows  $\partial\Omega^{(S)}/\partial\nu$  with  $Nx_o = 830\pi$ , ten times larger than the magnitude used in Figs. 3-18(a) and 3-18(b). When  $N$  is large and when  $\theta - \theta_o = 0$ , or when it is sufficiently close to zero, the stationary-phase intervals for  $\Psi^{(S)}$  will be numerous and extensive, as Fig. 3-18(c) suggests. For larger values of  $N$ , these may cause convergence problems for both the stationary-phase and numerical integration techniques when the LEO is at or very near the shadow boundary of the sphere.

From Eq. (3.9-2), it follows that these spikes [and the resulting stair-step pattern they create in  $\Omega^{(S)}$ , see Fig. 3-11(b)] arise because of near-zero crossings in the imaginary part of  $\mathcal{W}_l^+ + \mathcal{W}_l$  when the real part is already of diminished value [see Eqs. (3.8-7), (3.8-8), (3.8-12), and (3.8-13)]. When  $N$  is sufficiently large, there is a significant transition zone in spectral number, roughly defined by  $x_o < \nu < nx_o$ . Here the argument  $y = \nu^{2/3}\zeta[\nu/x_o]$  in the Airy functions is positive and the Airy functions have become exponential-like as a function of real  $\nu$ , but the Airy functions with their argument  $\hat{y} = \nu^{2/3}\zeta[\nu/nx_o]$ , which is negative in this zone, are still oscillatory. It is easily shown that  $\hat{y} \doteq y - Nx_o K_{x_o}^{-1}$ . For sufficiently large  $N$ , these near-singular points occur within the transition zone where  $\nu$  satisfies the condition

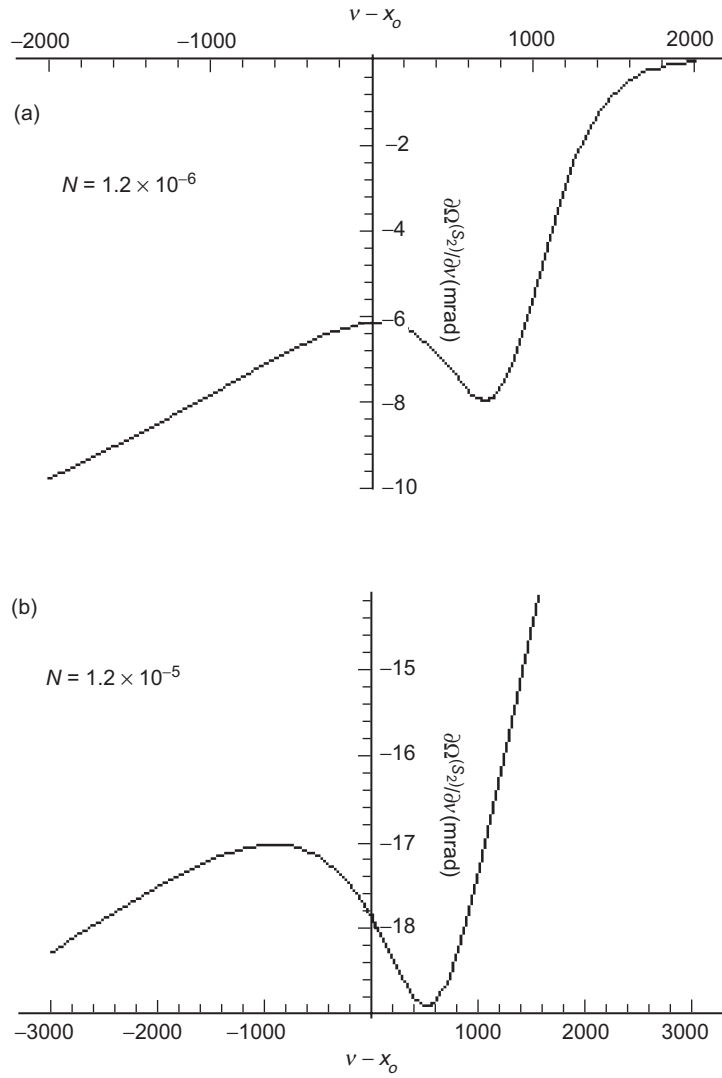


**Fig. 3-19.**  $\partial\Omega^{(j)}/\partial\nu$  for the degree  $j = 2$  scattering coefficient: (a)  $N = 1.2 \times 10^{-6}$  and (b)  $N = 12 \times 10^{-6}$ . Stationary points in spectral number are caustic points. Geometric optics predicts  $\theta - \theta_o = -3.5 \sqrt{2N}$  as the angular position of the caustic ray.

$$\tan X \cong -n^{-2} \sqrt{\frac{\hat{y}}{y}}, \quad x_o < \nu < nx_o \quad (3.13-19)$$

and whose spacing on the  $\nu$  axis becomes quite regular until  $\nu > \sim nx_o$ .

We can estimate the threshold of  $N$  above which the staircase features in  $\Omega^{(S)}$  begin to appear. From Fig. 3-10, we note that when the argument  $y$  ( $y$  real) of the Airy functions is less than  $-2$ , the Airy functions are decidedly sinusoidal, and when  $y > +2$ , they are exponential. A value of  $|y| = 2$  corresponds to a spectral number separation of  $|\nu - x_o| = 2K_{x_o}$ . Equating twice this separation to  $Nx_o$  yields a threshold  $N \geq 2K_{x_o}^{-2} \approx 1 \times 10^{-5}$ . The larger value  $Nx_o = 830\pi$  used in Figs. 3-17 and 3-18 is at that threshold.

### 3.13.5 Asymptotic Solutions for a Transparent Refracting Sphere

When the LEO is in the immediate vicinity of the shadow boundary,  $\theta \cong \theta_o$ , a numerical solution to the scattering problem for the refracting sphere is necessary because of the multiple stationary-phase points for  $\nu$  in the vicinity of  $x_o$  (see Figs. 3-17 and 3-18) and because the Airy functions are not well-represented by their asymptotic forms in this neighborhood. As the LEO descends deeper into the shadow, two stationary-phase points quickly emerge whose location in  $\nu$  space is well below  $x_o$ . Figure 3-17(b) shows the variation of  $\Psi^{(S)}$  with spectral number for a range of LEO angular coordinates and with  $Nx_o = 830\pi$ . The asymptotic stationary points are evident in this figure. We will show here that these stationary-phase points yield the phase delays and bending angles predicted by geometric optics, plus a diffraction pattern that agrees closely with the Fresnel diffraction predicted by the thin-screen model.

Let  $\nu^*$  denote a stationary-phase point. When  $\nu^* - x_o \ll -2K_{x_o}$ , the negative-argument asymptotic forms for the Airy functions grow increasingly more accurate. From Eqs. (3.8-3), (3.8-4), and (3.9-7), the asymptotic form  $\Omega_A$  for the aggregate scattering phase  $\Omega^{(S)}$  is given by

$$\left. \begin{aligned} 2\Omega^{(S)} &\rightarrow 2\Omega_A \doteq \frac{4}{3} \nu \left( (-\zeta(\mu/n))^{\frac{3}{2}} - (-\zeta(\mu))^{\frac{3}{2}} \right) \\ &= 2 \left( \sqrt{n^2 x_o^2 - \nu^2} - \nu \cos^{-1} \left( \frac{\nu}{nx_o} \right) - \sqrt{x_o^2 - \nu^2} + \nu \cos^{-1} \left( \frac{\nu}{x_o} \right) \right) \end{aligned} \right\} \quad (3.13-20)$$

where  $\mu = \nu / x_o < 1$ . We have already noted that this asymptotic form for the scattering phase also applies to the degree  $j=1$  scattered wave, which corresponds in geometric optics to the principal ray passing through the sphere without internal reflection. The stationary-phase condition (dropping the  $\Phi^+$  term) is given by

$$\frac{\partial \Psi^{(S)}}{\partial \nu} \rightarrow 2 \frac{\partial \Omega_A}{\partial \nu} + \frac{\partial \Phi^-}{\partial \nu} = 0 \quad (3.13-21)$$

Let  $\nu^*$  denote the value(s) for which Eq. (3.13-21) holds. From Eqs. (3.11-1) and (3.13-20), it follows that

$$\left. \begin{aligned} -2 \left( \cos^{-1} \left( \frac{\nu^*}{nx_o} \right) - \cos^{-1} \left( \frac{\nu^*}{x_o} \right) \right) + \theta_{\nu^*} - \theta = 0, \\ x_o \sin \theta_{\nu^*} = \nu^* \sin \theta_o \end{aligned} \right\} \quad (3.13-22)$$

To solve this expression for  $\nu^*$  explicitly in terms of  $\theta - \theta_o$ , we note that  $\nu^*$  is close in value to  $nx_o$ . Therefore, we write  $\nu^* / (nx_o)$  as

$$\frac{\nu^*}{nx_o} \doteq 1 + \frac{\hat{y}^*}{2K_{\rho_o}^2}, \quad K_{\rho_o} = \left( \frac{\rho_o}{2} \right)^{1/3}, \quad \rho_o = nx_o, \quad -\frac{\hat{y}^*}{2K_{\rho_o}^2} \ll 1, \quad (3.13-23)$$

Expanding Eq. (3.13-22) in powers of  $\hat{y}^* / K_{\rho_o}^2$  and also noting that  $\theta_{\nu^*} \doteq \theta_o + \hat{y}^* \tan \theta_o / (2K_{\rho_o}^2)$ , one obtains

$$2 \left\{ \sqrt{-\frac{\hat{y}^*}{K_{\rho_o}^2}} - \sqrt{2N - \frac{\hat{y}^*}{K_{\rho_o}^2}} \right\} + \theta - \theta_o - \frac{1}{2} \frac{\hat{y}^*}{K_{\rho_o}^2} \tan \theta_o \doteq 0 \quad (3.13-24)$$

This yields a quartic polynomial in  $(-\hat{y}^* / K_{\rho_o}^2)^{1/2}$ , the real roots of which provide the negative stationary-phase values of  $\hat{y}^*$ . Assuming that  $-\hat{y}^* \gg NK_{\rho_o}^2$ , one can expand Eq. (3.13-24) to obtain

$$\left. \begin{aligned}
 P[\xi] &= \xi^3 + K_{\rho_o}^{-1} D(\theta - \theta_o)\xi + 2DN + O[N^2] = 0, \\
 \hat{y} &= -\xi^2, \quad \hat{y}^* = (-\xi_1^2, -\xi_2^2), \quad \xi \geq 0, \\
 v^* &= nx_o \left( 1 + \frac{\hat{y}^*}{2K_{\rho_o}^2} + O\left[ \left( K_{\rho_o}^{-2} \hat{y}^* \right)^2 \right] \right), \quad K_{\rho_o} = \left( \frac{\rho_o}{2} \right)^{\frac{1}{3}}, \quad \rho_o = nx_o \\
 \xi_1 &= 2 \sqrt{D \frac{\theta_o - \theta}{3K_{\rho_o}}} \sin \Theta, \quad \xi_2 = 2 \sqrt{D \frac{\theta_o - \theta}{3K_{\rho_o}}} \cos(\pi/6 + \Theta), \\
 \Theta &= \frac{1}{3} \sin^{-1} \left( 3N \sqrt{\frac{3 \tan \theta_o}{2(\theta_o - \theta)^3}} \right), \quad D = nkr \cos \theta_o
 \end{aligned} \right\} \quad (3.13-25)$$

This cubic polynomial  $P[\xi]$  in Eq. (3.13-25) is the same as that given earlier in Eq. (3.13-18). The quantities  $\xi_1$  and  $\xi_2$  given by their expressions in Eq. (3.13-25) are the positive roots of  $P[\xi]$ .

Figure 3-17(b) shows that no real positive stationary-phase asymptotic solution exists in Mie scattering theory when  $\theta_o - \theta$  drops below a certain critical value, which corresponds to  $P[\xi]$  having no real positive roots. This critical value can be obtained by adjusting  $\theta_o - \theta$  so that the positive roots in Eq. (3.13-25) merge,  $P'[\xi] = P[\xi] = 0$ . One obtains

$$\theta^\dagger - \theta_o = -3 \left( \frac{nx_o}{2D} \right)^{1/3} N^{2/3} \quad (3.13-26)$$

which corresponds to a LEO angular position that is slightly inside of the shadow boundary. For the conditions shown in Fig. 3-17(b), Eq. (3.13-26) predicts that  $\theta^\dagger - \theta_o = -1.63$  mrad and the stationary-phase point in this case is given by  $y^\dagger = -(DN)^{2/3} \cong -112$ . Because  $\partial^2 \Psi^{(S)} / \partial v^2$  also equals zero at this stationary-phase point when  $\theta^\dagger - \theta_o = -1.63$  mrad, this value of  $\theta$  corresponds in geometric optics to the first contact with the caustic surface generated by the ray system associated with the system of stationary-phase points shown in Fig. 3-17(b) nearer to  $x_o$  (at  $y^* = -(\xi_1)^2$ ). When the scattering integrals for  $E_r^{(S)}$  and  $E_\theta^{(S)}$  in Eqs. (3.12-5) and (3.12-6) are evaluated, we should expect significant flaring for LEO angular coordinates near  $\theta^\dagger$  because of the broad band of spectral numbers about the stationary-phase point that constructively contributes to the scattering integral when  $\partial^2 \Psi^{(S)} / \partial v^2$  is near zero at the stationary-phase point. The range of angular coordinates  $\theta_o \geq \theta \geq \theta^\dagger$  corresponds in geometric optics to the LEO lying in a shadow zone where no

stationary-phase points exist in impact parameter space. This is a super-refractivity effect. In Mie scattering theory, we see that this zone yields a situation where there are no stationary-phase points in spectral number space (except for the vestigial effects of higher-degree scattering); so, we should expect considerable darkening in this region. For  $\theta \leq \theta^\dagger$ , the scattering integral supports two stationary-phase points based on asymptotic theory, plus the effects of higher-degree scattering nearer to  $y = 0$  if  $N$  is sufficiently large. The contributions from this pair of asymptotic points  $\xi_1$  and  $\xi_2$  will interfere with each other just as in geometric optics, where the branching and anomalous rays interfere with each other [see Chapter 2, Fig. 2-2(b)].

Equation (3.13-26) can be compared with the point of maximum signal amplitude predicted by the thin-screen model. From Chapter 2, Eq. (2.8-2), we have from Snell's law the refractive bending angle  $\alpha_S(h)$  from a sphere of radius  $r_o$  with a uniform refractivity  $N = n - 1$ :

$$\left. \begin{aligned} \alpha_S &= 2 \left( \sin^{-1} \left( \frac{nx_o + h}{x_o} \right) - \sin^{-1} \left( \frac{x_o + h}{x_o} \right) \right) \\ &\doteq \sqrt{8} \left( \sqrt{\frac{-h}{x_o}} - \sqrt{\frac{-h}{x_o} - N} \right) \\ h \leq h^c &= -(n-1)r_o = -Nx_o, \quad x = kr, \quad n > 1 \end{aligned} \right\} \quad (3.13-27)$$

where  $h$  is the altitude of the impact parameter of the ray above the sphere (see Fig. 3-16) and, therefore, negative for Eq. (3.13-27) to apply. Here  $h^c$  is the altitude of critical refraction. In geometric optics, no rays occur with turning points in the interval  $x_o(1-N) < x_* < x_o$ . From the thin-screen model (see Fig. 2-3),

$$h \doteq h_{LG} + D\alpha_S(h) \quad (3.13-28)$$

We know that a point where  $dh_{LG}/dh = 0$  marks the first contact with a caustic and also the point where both the first and second derivatives of the Fresnel phase in the scalar diffraction integral [Eq. (2.5-1)] are zero. Using Eq. (3.13-27) to find  $h^\dagger$ , which is the value of  $h$  at the point where  $dh_{LG}/dh = 0$ , and assuming that  $|h^\dagger| \gg Nx_o$ , one obtains

$$h^\dagger = -K_{\rho_o} (ND)^{2/3} \quad (3.13-29)$$

where  $\rho_o = nx_o$ . It follows, using Eq. (3.13-28), that



normal vector as it continues on to the LEO. This particular path incurs a total bending angle of  $2\varepsilon$ . In Fig. 3-20, the two radius vectors of length  $v$  are drawn perpendicular to the straight-line extensions of the incident and departing rays, respectively. From the geometry in Fig. 3-20, it follows that

$$v = nx_o \sin \varphi = nx \sin(\theta + 2\varepsilon) \quad \text{or} \quad \sin \varphi = \frac{\sin(\theta + 2\varepsilon)}{\sin \theta_o} \quad \left. \vphantom{\sin \varphi} \right\} \quad (3.13-32)$$

Here  $x_o = x \sin \theta_o$ . From Eqs. (3.13-31) and (3.13-32), when we set  $v = v^* = nx_o \sin(\theta + \delta) / \sin \theta_o$ , it follows that  $\varepsilon$  must assume the value  $\varepsilon = \delta / 2 = \alpha / 2$ . Snell's law is also satisfied when  $\varepsilon = \alpha / 2$ :  $n \sin(\varphi - \alpha / 2) = \sin \varphi$ . Moreover, upon noting in Fig. 3-20 that  $nx_o \sin(\varphi - \alpha / 2) = nx_o + h$ , it follows through first order in  $N$  that

$$v^* = nx_o + h, \quad y^* \doteq K_{\rho_o}^{-1}(h + Nx_o), \quad \rho_o = nx_o \quad \left. \vphantom{v^*} \right\} \quad (3.13-33)$$

Therefore, to at least first order in  $N$ , the value of  $v^*$  is identified as equivalent to the value of the impact parameter  $ka$  in geometric optics, which is a constant along the ray path (Bouguer's law) when spherical symmetry applies.

In summary, when the LEO is well inside the shadow boundary (so that the asymptotic forms for the Airy functions apply), Mie scattering theory at the stationary-phase point(s) in spectral number space  $v^*$  yields values for the bending angle of the total wave after scattering (incident plus scattered wave) that to at least first order in  $N$  are the same as those given by geometric optics. This should not be too surprising. The stationary-phase point  $v^*$  itself corresponds to the impact parameter in geometric optics, at least to first order in  $N$ . We will now show that  $v^*$  also yields the geometric-optics-predicted values for the LEO-observed phase and amplitude when  $v^*$  is well isolated in spectral number space so that the stationary-phase technique is valid. When the LEO is on or near the shadow boundary, where the asymptotic forms for the Airy functions do not apply with sufficient accuracy, then a numerical solution of the spectral integrals in Eqs. (3.12-5) and (3.12-6), or their equivalent, is required to obtain the amplitude and phase of the field.

### 3.13.7 Stationary Value for the Scattering Phase

The stationary value of the asymptotic form for the scattering phase  $\Psi^{(S)} \rightarrow \Psi_A^{(S)} = 2\Omega_A^{(S)} + \Phi^-$  can be obtained by expanding  $2\Omega_A^{(S)}$  in fractional powers of  $(v^2 - x_o^2) / x_o^2$ . From Eqs. (3.8-5), (3.9-8), (3.11-1), (3.13-20), and (3.13-21), we have

$$\begin{aligned} \Psi_A^{(S)}(\nu) = & \frac{2}{3\nu^2} \left( (n^2 x_o^2 - \nu^2)^{3/2} - (x_o^2 - \nu^2)^{3/2} \right) \\ & + D_\nu + \nu(\theta_\nu - \theta) + \mathcal{O} \left[ \left( (x_o^2 - \nu^2) x_o^{-2} \right)^{5/2} \right] \end{aligned} \quad (3.13-34)$$

where  $D_\nu = x \cos \theta_\nu = x_o \cos \theta_\nu / \sin \theta_o$ , which is the geometric phase delay term from the tangent point on a sphere of radius  $\nu$  to the LEO if it were located at  $\theta_\nu$ , and  $\nu(\theta_\nu - \theta)$  is the extra geometric phase delay because of the small offset  $\theta_\nu - \theta$  to account for the actual location of the LEO at  $\theta$ . We note that at the stationary-phase value  $\nu^*$  the geometric delay term becomes

$$\begin{aligned} D_{\nu^*} + \nu^*(\theta_{\nu^*} - \theta) &= x \left( \cos(\theta + \alpha_S) + \alpha_S \sin(\theta + \alpha_S) \right) \\ &= D_{\theta + \alpha_S} + a\alpha_S \end{aligned} \quad (3.13-35)$$

where  $D_{\theta + \alpha_S} = kr \cos(\theta + \alpha_S)$  and  $a = nx_o + h$  is the impact parameter. These terms account for the extra delay from the refractive bending; they give the geometric delay between the LEO and the intersection point of the line  $\theta = \pi/2$  with the co-centered sphere of radius  $a$ .

Evaluating  $\Psi_A^{(S)}$  at its stationary-phase point and expressing it in terms of the thin-screen variables using Eq. (3.13-33), we obtain

$$\Psi_A^{(S)} \Big|_{\nu^*} = \frac{2^{5/2}}{3} x_o \left( \left( \frac{-h}{nx_o} \right)^{3/2} - \left( \frac{-h}{nx_o} - N \right)^{3/2} \right) + D_{\theta + \alpha_S} + ka\alpha_S \quad (3.13-36)$$

For comparison with the Fresnel phase  $\Phi(h_S(h_{LG}), h_{LG})$  from scalar diffraction theory applied to the thin-screen model used in Chapter 2, Eq. (2.5-1), we write that expression here with the geometric phase delay  $D$  from the phase screen to the LEO added:

$$\Phi + D = \frac{2^{5/2}}{3} x_o \left( \left( \frac{-h}{nx_o} \right)^{3/2} - \left( \frac{-h}{nx_o} - N \right)^{3/2} - N^{3/2} \right) + D \left( 1 + \frac{\alpha_S^2}{2} \right) \quad (3.13-37)$$

where  $h(h_{LG})$  is the stationary-phase altitude of the ray at its turning point, which is a function of the thin-screen coordinate of the LEO,  $h_{LG} = nkr(\sin \theta - \sin \theta_o)$ . In the thin-screen model discussed in Chapter 2,  $D$  was only specified as the distance from the LEO to the thin screen, which was mounted perpendicular to the LEO–GPS line. Since  $D_{\theta + \alpha_S} + a\alpha_S = D_\theta \left( 1 + \alpha_S^2/2 + \mathcal{O}[\alpha_S^3] \right)$ , it is clear that to achieve correspondence between Eqs. (3.13-36) and (3.13-37) we should set  $D = D_\theta$ . Except for this arbitrariness

in  $D$  and the very small zero-point constant  $N^{3/2}$  introduced to null the thin-screen phase at the critical refraction altitude, the phase profiles predicted by Eqs. (3.13-36) and (3.13-37) agree closely, differing by terms of the order  $x_o \alpha_S^3$ .

The second derivative of  $\Psi^{(S)}$  is given by

$$\frac{\partial^2 \Psi^{(S)}}{\partial v^2} = 2 \left( \frac{1}{\sqrt{n^2 x_o^2 - v^2}} - \frac{1}{\sqrt{x_o^2 - v^2}} \right) + \frac{1}{D_v} \quad (3.13-38)$$

and, when it is expanded in powers of  $N$  and evaluated at  $v^* = nx_o + h$ , it becomes

$$\left. \frac{\partial^2 \Psi^{(S)}}{\partial v^2} \right|_{v=v^*} = \frac{1}{D_{v^*}} \left( 1 - D_{v^*} \left( \frac{2N}{x_o} \right) \left( \frac{nx_o}{-2h} \right)^{3/2} \right) \quad (3.13-39)$$

We see that  $\partial^2 \Psi^{(S)} / \partial v^2 \rightarrow 0$  when  $h = h^\dagger \doteq -(N^2 D_\theta^2 x_o / 2)^{1/3}$ , which is identical with the condition given in Eq. (3.13-29) with  $D = D_\theta$ , which was obtained from the thin-screen model, and also when  $\xi_1 = \xi_2$  in Eq. (3.13-25), which is based on Mie scattering.

In the stationary-phase technique, the term  $|\partial^2 \Psi^{(S)} / \partial v^2|^{-1/2}$  appears in the expression for the amplitude of the scattered field. Its minimum, which enables the broadest range of spectral numbers around the stationary-phase point to contribute to the scattering integrals, should closely correspond to the maximum amplitude for the scattered wave and, therefore, to maximum interference with the direct wave or to maximum darkening (and brightening) while the LEO is in the shadow. Appendix D discusses darkening in terms of Airy functions by expanding about the value of  $v$  where  $\partial^2 \Psi^{(S)} / \partial v^2 = 0$ .

From Eq. (3.13-39), we note from differentiating Eq. (3.13-27) and expanding that

$$\left. \frac{\partial^2 \Psi^{(S)}}{\partial v^2} \right|_{v=v^*} = \frac{1}{D_{v^*}} \left( 1 - D_{v^*} \frac{d\alpha_S}{dh} \right) = \frac{1}{D_{v^*}} \zeta_{v^*}^{-1} \quad (3.13-40)$$

where  $\zeta$  is the defocusing factor. This is the same factor that appears in scalar diffraction theory applied to the thin-screen model, or in geometric optics applied to a medium with a gradient in its refraction profile. There the second derivative of the Fresnel phase with respect to impact parameter also carries the factor  $\zeta^{-1}$  [see Section 2.6, Eq. (2.6-3)].

### 3.13.8 Evaluating the Scattering Integrals Using the Stationary-Phase Technique

When  $\theta - \theta_o < 0$  and it is sufficiently negative ( $\theta_o - \theta \gg \alpha_S + 2K_{x_o} / D_{x_o}$ ) so that the asymptotic forms for the Airy functions are applicable, the stationary-phase technique may yield accurate values for the scattering integrals. The total field is given by

$$\left. \begin{aligned} E_r^{(t)} &= E_r^{(S)} + E_r^{(i)} \\ E_\theta^{(t)} &= E_\theta^{(S)} + E_\theta^{(i)} \end{aligned} \right\} \quad (3.13-41)$$

From Eq. (3.13-5), we have

$$E_r^{(t)} = E_o \sqrt{\frac{\sin \theta_o}{2\pi i x_o \sin \theta}} \int_0^\infty \left( \frac{\sin^3 \theta_v}{\cos \theta_v} \right)^{1/2} e^{i\Psi^{(S)}} dv \quad (3.13-42)$$

When  $\theta$  lies well into the shadow regime [where a *single* stationary phase is dominant, i.e., the one at  $\xi_2$  in Eq. (3.13-25)] and, therefore, where the stationary-phase point is well isolated, then we can use the stationary-phase technique to evaluate Eq. (3.13-42). Expanding  $\Psi^{(S)}$  in powers of  $v - v^*$  about its stationary point, Eq. (3.13-42) becomes

$$E_r^{(t)} \doteq E_o \sqrt{\frac{\sin \theta_o \sin^3 \theta_{v^*}}{2\pi i x_o \sin \theta \cos \theta_{v^*}}} e^{i\Psi^{(S)}(v^*)} \int_0^\infty e^{i\left((v-v^*)^2 \frac{1}{2} \left( \frac{\partial^2 \Psi^{(S)}}{\partial v^2} \right)_{v^*} \right)} dv \quad (3.13-43)$$

Similarly, the  $\theta$  component of the total field is given by

$$E_\theta^{(t)} \doteq E_o \sqrt{\frac{\sin \theta_o \sin \theta_{v^*} \cos \theta_{v^*}}{2\pi i x_o \sin \theta}} e^{i\Psi^{(S)}(v^*)} \int_0^\infty e^{i\left((v-v^*)^2 \frac{1}{2} \left( \frac{\partial^2 \Psi^{(S)}}{\partial v^2} \right)_{v^*} \right)} dv \quad (3.13-44)$$

Here  $v^* \doteq \rho_o (1 - (\xi_2 / K_{\rho_o})^2 / 2)$ , where  $\xi_2$ ,  $\rho_o$ , and  $K_{\rho_o}$  are given in Eq. (3.13-25). When  $N$  is sufficiently small so that polarization effects from scattering are negligible, then it follows from Eqs. (3.13-43) and (3.13-44) that

$$\frac{E_r^{(t)}(r, \theta)}{E_\theta^{(t)}(r, \theta)} \doteq \tan[\theta_{v^*}(\theta)] = \tan(\theta + \alpha_S) \quad (3.13-45)$$

Thus, the total field observed by the LEO, when it is well inside the shadow boundary, is characterized to first order in  $N$  by plane waves propagating in a

direction that is inclined at an angle  $\alpha_s$  below the positive z-axis and in the plane of polarization. In this case,  $\alpha_s$  is to be evaluated on the main branch as given by Eq. (3.13-27).

Figure 3-21 shows the profiles of the main branch and the anomalous branch of  $\alpha_s$  versus  $\theta - \theta_o$  as predicted by geometric optics. The main branch is associated with the more negative value of  $y$  providing a stationary value for  $\Psi_A^{(S)}$  ( $y^* = -(\xi_2)^2$ ); the anomalous branch is associated with the stationary-phase value nearer to  $y = 0$  ( $y^* = -(\xi_1)^2$ ). The ray systems associated with the main branch and with the anomalous branch are discussed in Chapter 2, Fig. 2-2. Although the anomalous branch causes some interference, it is a weak contributor because of defocusing, or in Mie scattering parlance, because of the relatively large magnitude of  $\partial^2\Psi^{(S)}/\partial v^2$  in the vicinity of  $y^* = -(\xi_1)^2$  (see Fig. 3-17). This weakness continues until  $\theta$  nears first contact with the caustic,  $\theta - \theta_o = -3(r_o N^2 / 2D)^{1/3}$ , which in Fig. 3-21 is near  $-0.35$  mrad. There  $\partial^2\Psi^{(S)}/\partial v^2 = 0$ .

If one evaluates the Fresnel integral appearing in Eqs. (3.13-43) and (3.13-44) using Eq. (3.13-40) for  $(\partial^2\Psi^{(S)}/\partial v^2)_{v^*}$ , and assumes that the stationary-phase point is well-isolated, dominant, and located well into the Airy function asymptotic regime ( $y^* \ll -2$ ), then one obtains

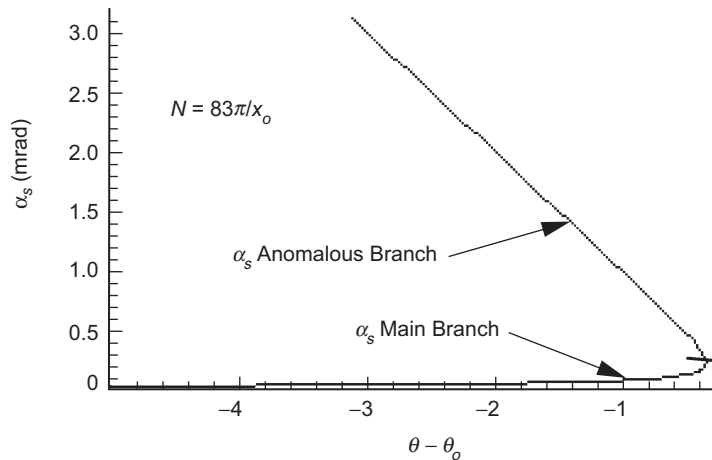


Fig. 3-21. Refractive bending angle based on geometric optics from the main and anomalous branches. The turning point is near the first contact with the caustic surface,  $\partial^2\Psi^{(S)}/\partial v^2 = 0$ .

$$\left. \begin{aligned} E_r^{(t)} &\doteq E_o \sin(\theta + \alpha_S) \sqrt{\frac{\sin(\theta + \alpha_S) \xi_{v^*}}{\sin \theta}} e^{i\Psi^{(s)}(v^*)} \\ E_\theta^{(t)} &\doteq E_o \cos(\theta + \alpha_S) \sqrt{\frac{\sin(\theta + \alpha_S) \xi_{v^*}}{\sin \theta}} e^{i\Psi^{(s)}(v^*)} \end{aligned} \right\} \quad (3.13-46)$$

One can use the stationary-phase technique to calculate the contribution to the scattering integrals from the minor stationary-phase point in spectral number space [see Fig. 3-17 and Eq. (3.13-25)] at  $y^* = -(\xi_1)^2$ . So long as this stationary-phase point exists, lies in the asymptotic regime, and is well separated from the dominant stationary-phase point so that sufficient phase accumulation occurs between stationary points and, in particular, so that the stationary-phase points are well away from inflection points [which holds, for example, when  $\theta_o - \theta = 2.0, 2.25, \dots$ , in Fig. 3-19(b)], then the evaluation of the scattering integrals for this point using the stationary-phase technique may be sufficiently accurate. In this case, Eq. (3.13-46) would be modified to

$$\left. \begin{aligned} E_r^{(t)} &\doteq E_r^{(t)} \Big|_{v=v_1^*} + E_r^{(t)} \Big|_{v=v_2^*}, \quad v_k^* \doteq \rho_o (1 - (\xi_k / K_{\rho_o})^2 / 2) \\ E_\theta^{(t)} &\doteq E_\theta^{(t)} \Big|_{v=v_1^*} + E_\theta^{(t)} \Big|_{v=v_2^*} \quad k = 1, 2, \dots \end{aligned} \right\} \quad (3.13-47)$$

On the other hand, if the phasor of the main contribution and/or the phasor of the secondary contribution have inaccuracies from application of the stationary-phase technique, then the error in the vector addition of these two contributions shown in Eq. (3.13-47) can be greatly exacerbated by these offsets. This especially holds when they interfere destructively. Moreover, we have noted that for  $\theta > \theta^\dagger$  there are no stationary-phase points, so the application of the stationary-phase technique to this regime is somewhat moot. For a regime (for example, when the LEO is well into the geometric shadow) where the computations of the scattering from the farther and nearer stationary-phase points using the stationary-phase technique are sufficiently accurate, then they can be combined through vector addition to calculate the interference pattern in that regime from a transparent refracting sphere. However, we will present instead the numerical integration solutions (in spectral number space) for a range of angular positions of the LEO inside and outside of the shadow boundary. Chapter 5 discusses further the conditions for validity of geometric optics in calculating interference between rays.

### 3.14 Duality Between Stationary-Phase Concepts in Electrodynamics and in Geometric Optics

In summary, when asymptotic conditions apply, that is, when the LEO is sufficiently inside the shadow boundary so that asymptotic forms for the Airy functions apply, or, equivalently, when  $\Omega^{(S)} \rightarrow \Omega_A$  asymptotically, then we have a kind of duality between the stationary-phase processes on one hand over spectral number space in electromagnetic theory and on the other hand in geometric optics over impact parameter space. For electromagnetic theory applied to a uniform refracting sphere in a vacuum on one hand, and for the scalar diffraction theory applied to the thin-screen proxy for the sphere on the other hand, the correspondence between these systems shown in Table 3-1 holds asymptotically at least to first order in  $N$  when stationary-phase values are assigned in each system.

### 3.15 Diffraction from a Large, Transparent, Refracting Sphere Using Mie Scattering Theory

#### 3.15.1 Numerical Integrations

When “thin-atmosphere” conditions hold, a straight numerical integration of the scattering integrals in Eq. (3.13-5) performs well, although some caution is needed in dealing with the oscillatory nature of the kernels in these integrals to avoid aliasing effects and inaccuracies from under-sampling. For larger values of  $N$ , for example, such as found in a raindrop, the increasing number of episodes of high acceleration in phase with spectral number makes the numerical integration technique onerous. In this case, evaluating the scattering integrals in complex spectral number space using the Sommerfeld–Watson transformation is probably a better approach for angular positions in the geometric shadow of the refracting sphere.

Here our values of  $N$  are relatively small, and so the numerical integrations in Eq. (3.13-5) are used to obtain the scattered field  $E^{(S)}(r, \theta)$  from a transparent refracting sphere; the integrations are aided by stationary-phase theory to define practical limits and limiting forms. In Eq. (3.13-5), we use the definition for  $\Omega^{(S)}$  given in Eqs. (3.5-15) and (3.9-2), and we omit the  $\Phi^+$  term because it has a negligible effect on the integrals for large  $x_o$  and near-grazing conditions. Figures 3-22 and 3-23 display the results of this computation. Figure 3-22 shows the amplitude of the total field or vector sum of the incident wave and the scattered waves,  $E^{(S)}(r, \theta) + E^{(i)}(r, \theta)$ , at the LEO position, where  $E^{(i)}(r, \theta) = \hat{x}E_o \exp(ix \cos \theta)$ . Here  $\hat{x}$  is a unit vector in the up direction;

Table 3-1. Duality between systems.

Variational Parameter	Electrodynamics		Geometric Optics	
	Spectral Number	Impact Parameter	Spectral Number	Impact Parameter
Stationary Point	$v^*$	$nx_0 + h^*$	$\Leftrightarrow$	
Stationarity Condition	$\frac{\partial \Psi^{(S)}}{\partial v} = \frac{\partial(2\Omega_A + \Phi^-)}{\partial v} = 0$	$\frac{\partial}{\partial h} \left( \int_h^\infty \alpha dh + \frac{(h - h_{LG})^2}{2D} \right) = \frac{\partial \Phi}{\partial h} = 0$	$\Leftrightarrow$	
Gradient	$-\frac{\partial 2\Omega_A}{\partial v} \Big _{v^*} = \theta_{v^*} - \theta$	$\alpha$ Bending Angle	$\Leftrightarrow$	
Limb Distance	$D_{v^*} = \sqrt{x^2 - v^{*2}}$	$D = \sqrt{x^2 - n^2 x_0^2}$	$\Leftrightarrow$	
Stationary Phase	$\Psi^{(S)} \Big _{v^*} = \left[ 2 \left( (n^2 x_0^2 - v^2)^{1/2} - (x_0^2 - v^2)^{1/2} \right) + D_{v^*} \right]_{v^*}$	$\Phi(h^*(h_{LG}, h_{LG})) + D$	$\Leftrightarrow$	
Reflection Coefficient	$ \rho^{(0)} _{v^*} = \frac{n(x_0^2 - v^2)^{1/2} - (n^2 x_0^2 - v^2)^{1/2}}{n(x_0^2 - v^2)^{1/2} + (n^2 x_0^2 - v^2)^{1/2}} \Big _{v^*}$	$R_{\parallel}$	$\Leftrightarrow$	
Defocusing $\zeta$ :	$\left( D_{v^*} \frac{\partial^2 \Psi^{(S)}}{\partial v^2} \right)_{v^*}^{-1} = \left( 1 + D_{v^*} \frac{\partial^2 2\Omega_A}{\partial v^2} \right)_{v^*}^{-1}$	$\left( 1 - D \frac{d\alpha}{dh} \right)_{h^*}^{-1} = \left( D \frac{\partial^2 \Phi}{\partial h^2} \right)_{h^*}^{-1}$	$\Leftrightarrow$	
Caustic Contact	$\zeta \rightarrow \infty$ $\left( 1 + D_{v^*} \frac{\partial^2 2\Omega_A}{\partial v^2} \right)_{v^*} \rightarrow 0$	$\left( 1 - D \frac{d\alpha}{dh} \right)_{h^*} \rightarrow 0$	$\Leftrightarrow$	

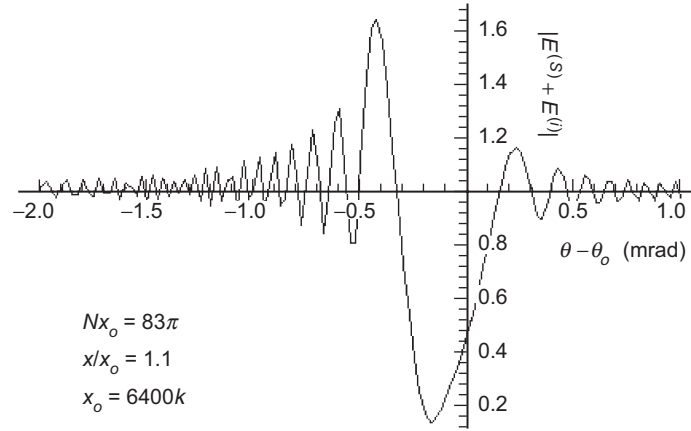


Fig. 3-22. Amplitude of the total field at the LEO (incident wave plus scattered wave from a refracting sphere); based on a numerical integration using Mie scattering theory.

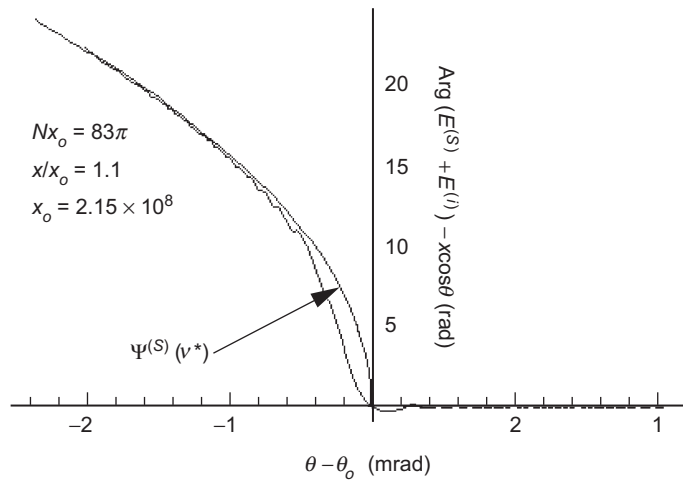


Fig. 3-23. Phase of the total field at the LEO (incident plus scattered wave from a refracting sphere) minus  $x \cos \theta$ ; from Mie scattering theory.

it is the in-plane vector perpendicular to  $\hat{z}$ , which points along the direction of propagation (see Fig. 3-1). Similarly,  $\mathbf{E}^{(S)} = \hat{r}E_r^{(S)} + \hat{\theta}E_\theta^{(S)}$ . The refractivity used in this figure is  $N = 83\pi / x_0$ .

The phase of the total field is shown in Fig. 3-23 for  $N = 83\pi / x_0$ . The phase has been stopped, i.e., multiplied by the geometric phase delay phasor  $\exp(-ix \cos \theta)$  to eliminate the phase rate from changing geometric delay with

changing  $\theta$ ; but for  $\theta < \theta_o$ , there is an additional phase rate because of the “lens” effect due to the refracting sphere. These Mie scattering solutions in Figs. 3-22 and 3-23 are in close agreement with the results from the thin-screen/scalar diffraction model for a refracting sphere, as presented in Chapter 2, Figs. 2-17 through 2-20 for  $N = 83\pi / x_o$ .

### 3.15.2 Comparison with Thin-Screen/Scalar Diffraction Results

Figures 3-24 and 3-25 compare Mie scattering results with the scalar diffraction thin-screen results for  $N = 83\pi / x_o$  and  $N = 830\pi / x_o$ , respectively. In the thin-screen computation,  $D$  has been set equal to  $D_\theta$ . The noise in these figures because of limited computational precision is about 0.001 in amplitude and about 0.01 rad in phase. The amplitude profiles [of  $E^{(S)}(r, \theta) + E^{(i)}(r, \theta)$ ] are in virtual agreement with Mie scattering producing perhaps 1 to 2 percent deeper fringes. We see the very deep shadow zone but no rainbow effects; they are to be seen faintly at larger values of  $\theta_o - \theta$ , near  $-6$  mrad for Fig. 3-24(a) and near  $-18$  mrad for Fig. 3-25(a).

Figures 3-24(b) and 3-24(c) and Figs. 3-25(b) and 3-25(c) show the differences between these two systems in amplitude and in phase for  $Nx_o = 83\pi$  and  $Nx_o = 830\pi$ , respectively. These figures show good agreement except in the midst of the shadow zone, which would be the most likely region for differences to arise because of the super-refracting conditions here. Geometric optics, which provides the basis for the thin-screen phase profile, denies the existence of rays in the shadow zone, but electromagnetic waves do pass through this region, albeit faintly, having already interacted with the bound charges of the dielectric medium in the sphere. Also, this is the region where no significant stationary-phase points exist in either spectral number space in electromagnetic theory or in impact parameter space in geometric optics, which might accentuate whatever differences exist between the two systems. Moreover, the main contributions to the Mie scattering integrals in this region partly come from spectral numbers where the asymptotic forms for the Airy functions do not apply. It would be surprising if these two systems did not disagree to some extent deep in the shadow zone.

The phase differences accumulate primarily in the shadow zone. The “bow-tie” pattern in the amplitude difference shown in Fig. 3-25(b) is a result of phase runoff between the two systems. A discontinuity in refractivity provides a relatively severe test of the fidelity of the thin-screen model. “Smoother” discontinuities, such as in the gradient of the refractivity, are less severe. This is discussed further in Chapter 5.

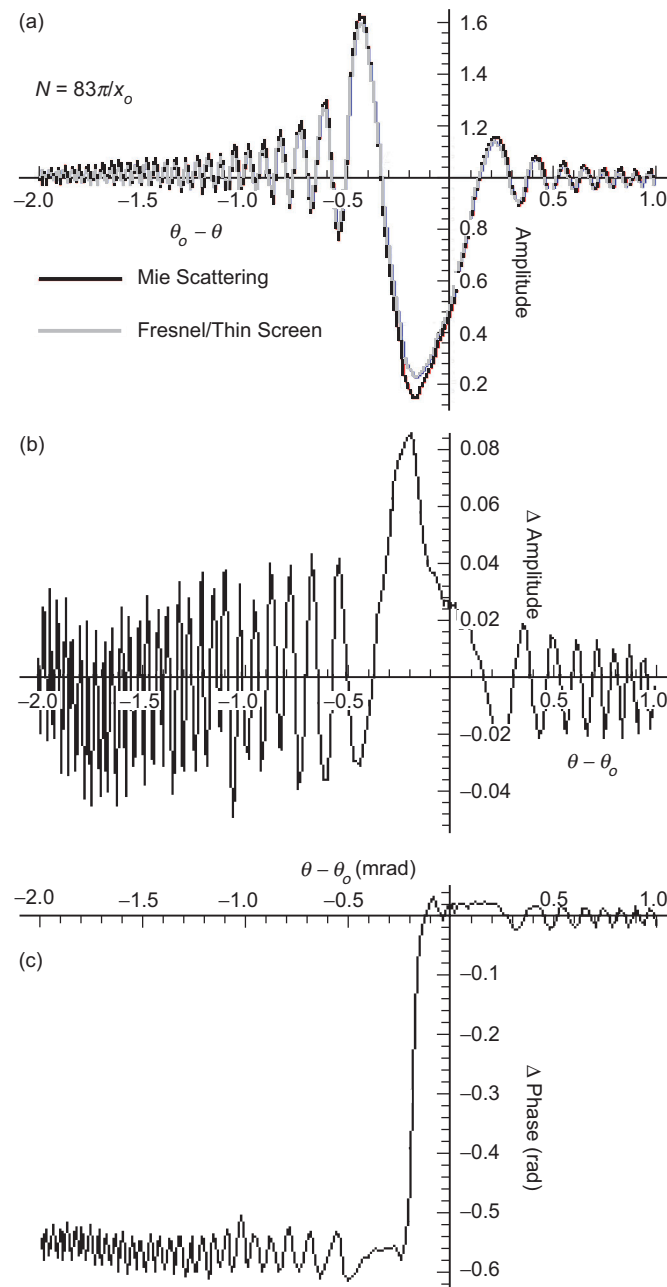


**Fig. 3-24.** Comparison of the total field at the LEO based on Mie scattering with a scalar diffraction/thin-screen model: (a) amplitude, (b) amplitude difference, and (c) phase difference.  $N = 83\pi/x_0$ ,  $x = 1.1x_0$ ,  $x_0 = kr_0 \approx 2.15 \times 10^8$ , and  $r_0 = 6478$  km.

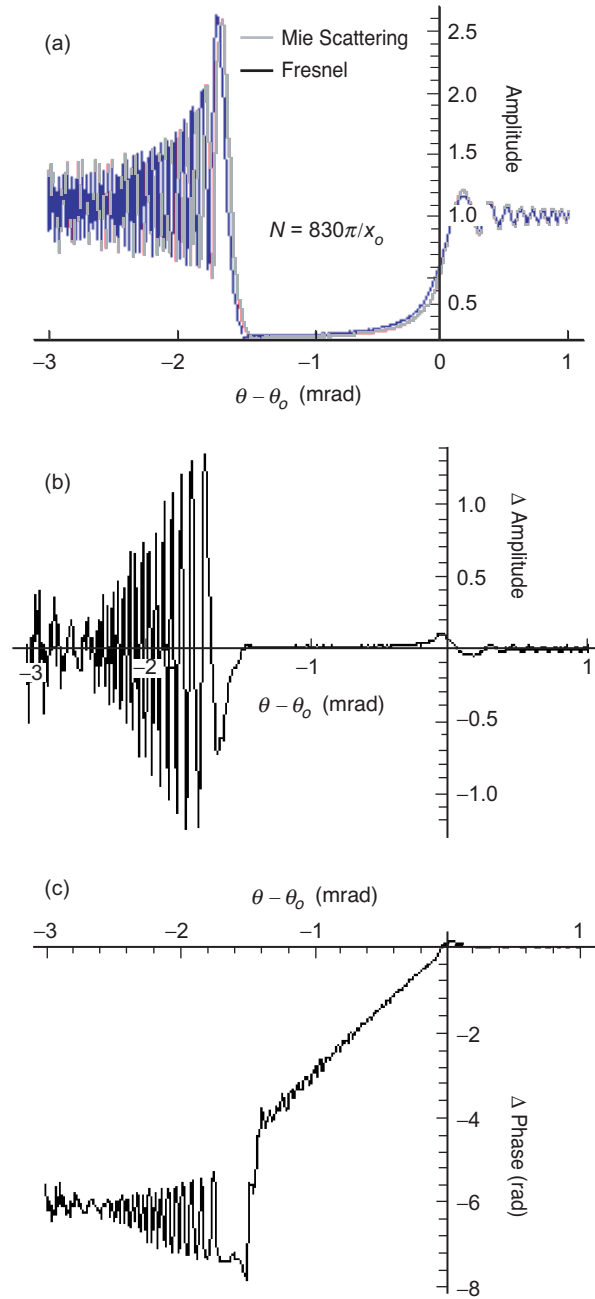


Fig. 3-25. Mie Scattering versus scalar diffraction/thin-screen model: (a) amplitudes, (b) amplitude difference, and (c) phase difference. The same conditions as used in Fig. 3-24, except  $N = 830\pi/x_o$ .

The thin-screen methodology is much less complex and computationally less intensive than Mie scattering theory; the ratio of the computational times to obtain the equivalent results shown in Figs. 3-24 and 3-25 is about 1:3.

### 3.16 Looking for Rainbows

#### 3.16.1 Rainbow Effects on the Refracting Sphere

We can evaluate the scattered field on the surface of the sphere,  $r = r_o$ , to see if the  $j=2$  rainbow effects appear in the neighborhood of  $\theta = \sim \theta_o - 2(6N)^{1/2}$ ,  $\theta_o = \pi/2$ . However, in this case where  $r = r_o$ , we cannot use the asymptotic forms for the Hankel functions given in Eq. (3.10-1) for the LEO radial position because the argument  $Y$  of the Airy functions will be small or even positive when  $\nu \approx x_o$ . Instead, we may use the Airy function forms for the spherical Hankel functions given in Eq. (3.8-9) with the understanding that when  $\nu < x_o - 3K$  (for better than 0.1 percent accuracy), we can continue to use the asymptotic forms given by Eq. (3.10-1). If this form in Eq. (3.8-9) is substituted into the scattering series given in Eq. (3.12-3) for  $E_r^{(S)}(r_o, \theta)$  and a conversion from the sums into integrals with  $y$  as the independent variable is made, one obtains the expressions for the scattering for an observer located on the surface of the refracting sphere. Retaining only the relevant terms, we obtain

$$\left. \begin{aligned} E_r^{(S)} &= \frac{E_o}{\sqrt{\sin \theta}} \exp(ix_o \tilde{\theta}) \int_{-\infty}^{\infty} S_l \left( \frac{\nu}{nx_o} \right)^{\frac{3}{2}} \text{Ai}[\hat{y}] \exp(i\hat{y} K_{\rho_o} \tilde{\theta}) d\hat{y} \\ \frac{\nu}{\rho_o} &= 1 + \frac{\hat{y}}{2K_{\rho_o}^2} + O\left[ \frac{\hat{y}}{2K_{\rho_o}^2} \right]^2, \quad \tilde{\theta} = \frac{\pi}{2} - \theta, \quad \rho_o = nx_o = nkr_o \end{aligned} \right\} \quad (3.16-1)$$

$E_{\theta}^{(S)}$  will be very small because  $\theta \approx \pi/2$ . The scattering term  $S_l$  is given by Eqs. (3.5-11) and (3.5-15). It can be replaced by higher-degree scattering coefficients if one wishes to do so. Of particular interest is the degree  $j=2$  term, which provides the scattered field for the primary rainbow.

Figure 3-26 shows the amplitude of the total field (aggregate scattered plus incident) for the two cases:  $N = 83\pi/x_o$  and  $N = 830\pi/x_o$ . These are obtained from a numerical integration of Eq. (3.16-1). Even for positions located on the surface of the scattering sphere a shadow zone develops, but it has a different shape and location than shown in Figs. 3-24 and 3-25. The appearance of ringing in Fig. 3-26(b) in the Fresnel fringe amplitude near  $\theta - \theta_o \approx -20$  mrad presages the growth of rainbow resonances at certain

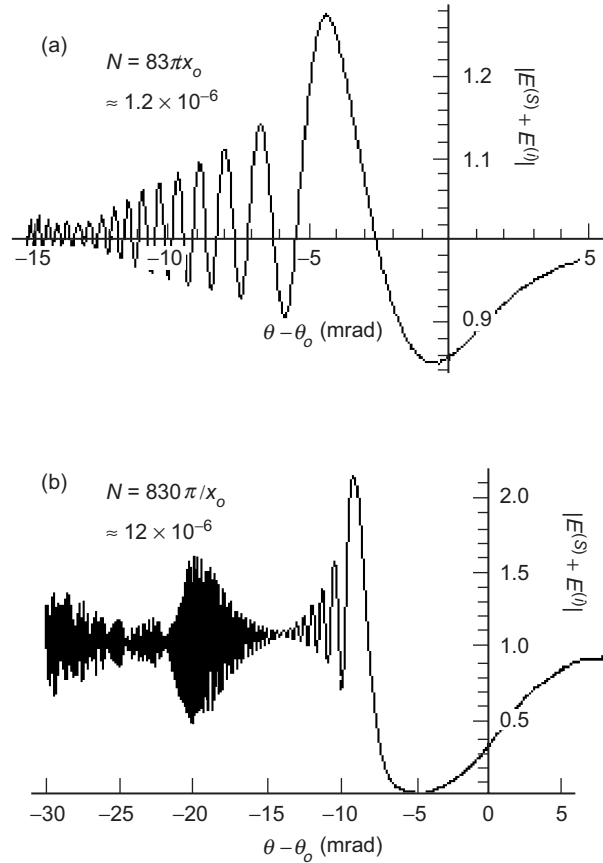


**Fig. 3-26. Amplitude of the total field from a refracting sphere for an observer located on its surface:**  
 (a)  $N = 83\pi/x_o$  and (b)  $N = 830\pi/x_o$ .

angular positions that would result from using larger values of the refractivity. Some under-sampling effects are evident in Fig. 3-26(b), particularly for  $\theta - \theta_o < -15$  mrad.

One can apply the stationary-phase technique to Eq. (3.16-1). It can be shown that stationary-phase points exist near  $\hat{y} = 0$ , and when  $\pi/2 - \theta > \sim 8N$ , a point also exists at

$$\hat{y}^* \doteq -\frac{K_{\rho_o}^2}{4} \left( \tilde{\theta} + \sqrt{\tilde{\theta}^2 - 8N} \right)^2 \quad (3.16-2)$$

Figure 3-27 shows the amplitude of the scattered field on the refracting sphere for only the degree  $j=2$  term, i.e.,  $|\mathbf{E}^{(S_2)}(r_o, \theta)|$ . The scattering

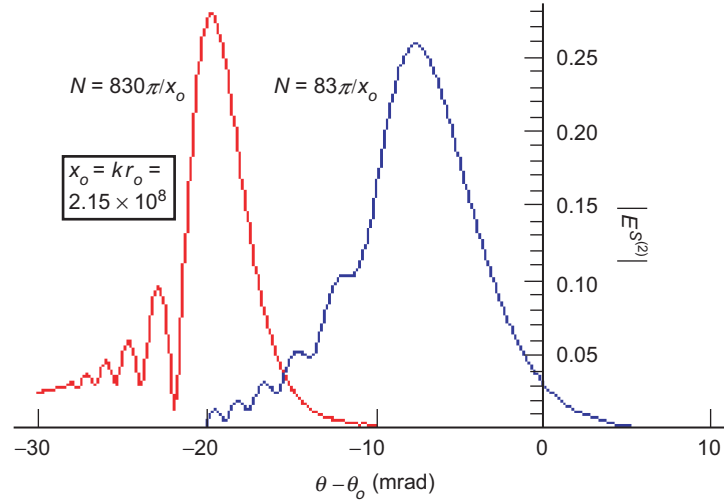


Fig. 3-27. Amplitude of the degree  $j = 2$  scattered wave for an observer located on the surface of the refracting sphere.

coefficient  $S_l^{(2)}$  replaces  $S_l$  in Eq. (3.16-1); it is obtained from Eqs. (3.5-11) and (3.9-3) and it is given by

$$S_l^{(2)} = 2n \frac{\mathcal{W}_l^+}{(\mathcal{W}_l^-)^3} \quad (3.16-3)$$

The locations of the peaks of the distributions in Fig. 3-27 agree moderately well with the degree  $j = 2$  scattering angles predicted by geometric optics in Eq. (3.4-9). For the case  $N = 830\pi/x_0$ , the peak at  $-20$  mrad falls in a relatively quiescent fringe region in Fig. 3-26(b); therefore, the interference of the  $j = 2$  scattered wave with the aggregate scattered wave is quite noticeable in the form of expanded fringe amplitude in that neighborhood. On the other hand, for the case  $N = 83\pi/x_0$ , its peak lies near the location of the maximum power from the aggregate scattering in Fig. 3-26(a); its effect is scarcely noticeable. The angular location of the peaks in these amplitude distributions in Fig. 3-27 correspond to the scattering angle of the rainbow in geometric optics, which results from a ray undergoing a single internal reflection.

### 3.16.2 Rainbow Effects at LEO Distances

Figure 3-28 shows the amplitude of the scattered field for only the  $j = 2$  term at the location of the LEO, namely, at  $r = 1.1r_0$  for the case  $N = 830\pi/x_0$ . Here the peak amplitude is diminished by a factor of 6 relative to that shown in

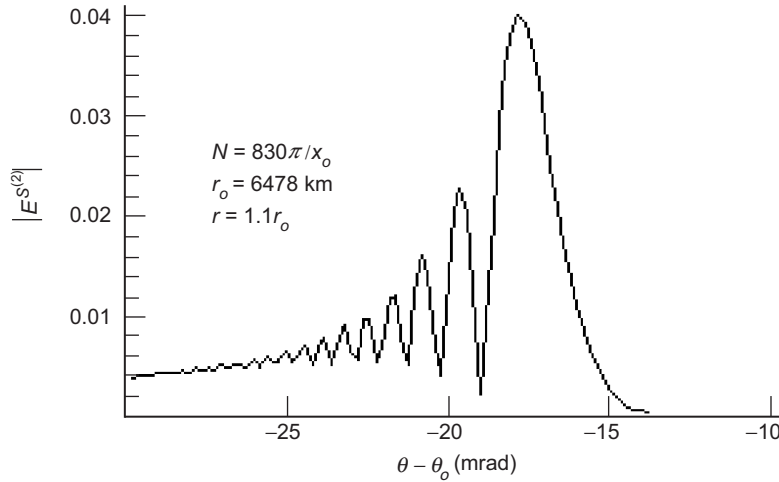


Fig. 3-28. Amplitude of the degree  $j = 2$  scattered wave at the LEO.

Fig. 3-27 (for  $N = 83\pi / x_0$ , it is diminished by a factor of 25). The location of the peak amplitude in Fig. 3-28 agrees closely with the prediction from geometric optics given in Eq. (3.4-9), but the contribution of the degree  $j = 2$  scattered wave to the aggregate scattering shown in Fig. 3-26(a) is very faint (a maximum of  $\sim 4$  percent). For this case,  $Nr_0 \ll (\lambda D_S)^{1/2}$ , the radius of the first Fresnel zone, which is about 750 m. In contrast, for the observer located on the sphere (to which Fig. 3-27 applies), the effective “Fresnel radius” is only about 20 m at the angular location where the caustic is dominant ( $\sim -20$  mrad); which is comparable to the altitude of the turning point of the ray at the caustic point.

In terms of stationary-phase concepts, the difference in amplitude peaks shown in Figs. 3-27 and 3-28 can be explained in terms of the magnitude of the quadratic term  $\partial^2 \Psi^{(S^{(2)})} / \partial y^2$  for the two scenarios. The location of the stationary-phase points in spectral number space for the  $j = 2$  scattering coefficient corresponds for the  $r = 1.1r_0$  case to a situation where  $\partial^2 \Psi^{(S^{(2)})} / \partial y^2$  is relatively large, which restricts the breadth of spectral number contributions to the scattering integrals (see Fig. 3-18). When the observer is located on the refracting sphere  $r = r_0$ , it can be shown that  $\partial^2 \Psi^{(S^{(2)})} / \partial y^2$  is relatively smaller.

### 3.16.3 Assessing Rainbow Effects Using the Third-Order Stationary-Phase Technique

One can use third-order stationary-phase theory to solve for the angular location of the peak amplitude for the degree  $j = 2$  scattered wave, such as that shown in Fig. 3-28, and also its magnitude. Using Eqs. (3.8-12), (3.8-14), (3.9-3), and (3.16-3), one obtains the asymptotic form of the scattering coefficient for negative values of  $\hat{y}$  and  $y$ :

$$\left. \begin{aligned} S_l^{(2)} &\rightarrow -|S_A^{(2)}| \exp(i(4\hat{X} - 2X)), \quad y < 0 \\ |S_A^{(2)}| &= 2\sqrt{y\hat{y}} \frac{(-\hat{y})^{1/2} - (-y)^{1/2}}{\left((-y)^{1/2} + (-y)^{1/2}\right)^3} \end{aligned} \right\} \quad (3.16-4)$$

where  $\hat{X}$ ,  $X$ ,  $\hat{y}$ , and  $y$  are defined in Eq. (3.8-14). The degree  $j = 2$  scattering phase  $\Psi^{(2)}$  in the scattering integrals of Eqs. (3.12-5) and (3.12-6) has the asymptotic form for negative  $y$  that is given by

$$\Psi^{(2)} = 4\hat{X} - 2X + \Phi^- \quad (3.16-5)$$

To locate the peak amplitude, we set  $\partial^2 \Psi^{(2)} / \partial y^2 = 0$ , which yields

$$2(-\hat{y})^{-1/2} - (-y)^{-1/2} + \frac{K_{x_o}^2}{D_v} = 0 \quad (3.16-6)$$

This condition defines the point  $y^\dagger$ , and thus the neighborhood in spectral number space providing the maximum contribution to the degree  $j = 2$  scattered wave. The condition in Eq. (3.16-6) yields the single relevant root

$$y^\dagger \doteq -\frac{Nx_o}{3K_{x_o}} \left[ 1 - \frac{8}{3} \left( \frac{Nx_o}{3K_{x_o}} \right)^{1/2} \frac{K_{x_o}^2}{D_{x_o}} \right] \quad (3.16-7)$$

which for the case  $N = 830\pi / x_o$  shown in Fig. 3-28 yields a value of  $y^\dagger = -1.81$ , just barely outside of the asymptotic range. From Eqs. (3.13-33) and (3.16-7), it follows that the altitude of the turning point of the corresponding ray is given by  $h_S \doteq K_{x_o} y^\dagger \doteq -Nx_o / 3$ , which agrees exactly with the prediction of geometric optics made in Eq. (3.4-10) and shown in Fig. 3-8.

From Eq. (3.16-5), it follows that

$$\frac{\partial \Psi^{(2)}}{\partial y} \doteq -4(-\hat{y})^{1/2} + 2(-y)^{1/2} + K_{x_o}(\theta_v - \theta) \quad (3.16-8)$$

If we also adjust  $\theta$  so that  $\partial \Psi^{(2)} / \partial y = 0$  at the flexure point  $y^\dagger$  given in Eq. (3.16-7), we obtain a stationary-phase refractive bending angle  $\alpha^\dagger$  that corresponds closely to the direction of maximum scattering for the degree  $j=2$  wave. From Eqs. (3.16-7) and (3.16-8),  $\alpha^\dagger$  is given by

$$\alpha^\dagger = 2\sqrt{6N} + O[N^{3/2}] \quad (3.16-9)$$

Using the thin-screen approximation (see Fig. 3-16)  $\theta - \theta_o \doteq h_S / D_S - \alpha$ ,  $h_S^\dagger / D_S \doteq K_{x_o} y^\dagger / D_{x_o}$ , which is very small compared to  $\alpha^\dagger$ , it follows that

$$\theta^\dagger - \theta_o \doteq -\alpha^\dagger = -2\sqrt{6N} \quad (3.16-10)$$

which for the case  $N = 830\pi / x_o$  yields a value of  $-17.1$  mrad; this is near the location of the peak in Fig. 3-28 ( $-17.9$  mrad), and it agrees exactly (to first order in  $N$ ) with the stationary scattering angle predicted by geometric optics in Eq. (3.4-9) for the degree  $j = 2$  scattered ray.

To estimate the magnitude of the peak in Fig. 3-28 and to refine the estimate of its angular direction given by Eq. (3.16-10), we can use the third-order stationary-phase technique on the scattering integral, which is discussed in Appendix D in connection with its application to the scalar diffraction integral for the thin screen. The treatments are formally identical for the two systems, i.e., for the Mie scattering integrals and for the scalar diffraction integral. So, without derivation, we use those results given in Appendix D on the Mie scattering integrals. From Eqs. (3.12-5) and (3.12-6) with  $S_l$  replaced by  $S_l^{(2)}$ , upon changing the integration variable from  $v$  to  $y$ , and upon expanding  $\Psi^{(2)}$  through third degree in  $y$  about the point of flexure  $y^\dagger$  where  $\partial^2 \Psi^{(2)} / \partial y^2 = 0$ , the third-order stationary-phase technique yields for the amplitude of the degree  $j = 2$  scattered wave

$$\left. \begin{aligned} |E^{S^{(2)}}| &\doteq 2E_o K_{x_o} \sqrt{\frac{2\pi}{D_{x_o}}} |S_A^{(2)}|_{y^\dagger} \left( 2 \left| \frac{\partial^3 \Psi^{(2)}}{\partial y^3} \right|_{y^\dagger}^{-1} \right)^{1/3} \text{Ai}[z], \\ z &= \left( \frac{\partial \Psi^{(2)}}{\partial y} \right)_{y^\dagger} \left( 2 \left| \frac{\partial^3 \Psi^{(2)}}{\partial y^3} \right|_{y^\dagger}^{-1} \right)^{1/3} \end{aligned} \right\} \quad (3.16-11)$$

The Airy function reaches a local maximum  $\text{Ai}[z] = 0.5356$  at  $z = -1.02$  (see Appendix D, Fig. D-1). From Eq. (3.16-8), if we adopt a value for  $\theta$  so that  $z = -1.02$  in Eq. (3.16-11), we should obtain the peak amplitude for the scattered wave. From Eqs. (3.16-4) and 3.16-6), it follows that  $\left|S_A^{(2)}\right|_{y^\dagger} \doteq 4/27$ , independent of the value of  $N$ . When Eqs. (3.16-4) through (3.16-8) are used to evaluate Eq. (3.16-11), one obtains a peak amplitude and location that are given by

$$\left. \begin{aligned} \left|E_{\text{MAX}}^{S(2)}\right| &= 0.402E_o \sqrt{NK_{x_o} \tan \theta_o}, \\ \theta_{\text{MAX}} - \theta_o &= -2\sqrt{6N} - \frac{0.715}{N^{1/2}K_{x_o}^2} - \frac{1}{3}N \tan \theta_o \end{aligned} \right\} \quad (3.16-12)$$

Equation (3.16-12) predicts a peak amplitude,  $0.045E_o$ , which agrees well with the peak (0.04) shown in Fig. 3-28. It predicts a location for the peak at  $\theta_{\text{MAX}} - \theta_o = -17.97$  mrad; the actual location of the peak in Fig. 3-28 is  $-17.9$ . The offset between the predictions of Mie scattering and geometric optics, which for the case shown in Fig. 3-28 is about 0.9 mrad, was first discovered by Airy in his investigation of rainbow caustics. He used essentially a third-order ray-optics approach, which results in a formalism that is similar to that described<sup>4</sup> in Appendix-D. Equation (3.16-12) predicts that the peak amplitude of the degree  $j = 2$  scattered wave at the location of the LEO grows as  $N^{1/2}$ . For the case of  $N = 83\pi/x_o$ , this peak is located at about  $\theta - \theta_o = -6$  mrad with an amplitude at the LEO that is about 1 percent of the total amplitude.

Incidentally, determination of the peak amplitude and location of the higher-degree scattered waves follows in an analogous way to that used for the degree  $j = 2$  scattering. However, the stationary-phase points for the higher degrees are even closer to zero (see Fig. 3-18) and, therefore, recede further from the region of validity of the asymptotic forms for the Airy functions. With this caveat in mind, it is easily shown using the third-order stationary-phase

---

<sup>4</sup> In geometric optics, the scattering angles for the rainbow caustics are independent of the size of the scattering sphere [see Eq. (3.4-9)]. The third-order Mie scattering results in Eq. (3.16-11) show a dependence on the radius-to-wavelength ratio. This theory can be used to calculate the sensitivity of the scattering angle to a change in wavelength of the incident wave for a dispersive refractive medium. For water in the visual spectrum, Mie third-order theory (retaining higher powers of  $N$  to maintain sufficient accuracy) can be used to show that the scattering-angle sensitivity to wavelength change is greater for large raindrops than it is for small drops. This can be used to explain the brilliance and sharpness of the color separation in rainbows observed from large raindrops and the almost washed out colors from a fine mist. The size of a raindrop tends to increase during its descent.

technique and the negative argument asymptotic forms for the Airy functions that the peak amplitude and its location are given by

$$\left. \begin{aligned} |E_{\text{MAX}}^{S_j}| &= 0.536E_o \left[ \frac{4j^2}{j^2-1} \right]^{1/3} \frac{4(j^2-1)j^{j-1}}{(j+1)^{2j}} \sqrt{\frac{2\pi N K_{x_o} \tan \theta_o}{3}}, \\ \theta_{\text{MAX}} - \theta_o &= -N \frac{\tan \theta_o}{j^2-1} - 2\sqrt{2(j^2-1)N} \\ &\quad - \left( \frac{1.47}{N^{1/2} K_{x_o}^2} \right) \left( \frac{j^2-1}{12j^2} \right)^{1/3} \left( \frac{j^2-1}{2} \right)^{1/2} \end{aligned} \right\} \quad (3.16-13)$$

This equation shows that the peak amplitude of the rainbow caustics attenuates rapidly with increasing degree.

It is remarkable how well Eqs. (3.16-6) through (3.16-12) predict the angular location and peak amplitude of the degree  $j=2$  scattered wave, considering the borderline validity of the asymptotic assumption used to derive them.

Figure 3-29 shows the Mie scattering and Fresnel diffraction extensions of Fig. 3-25(a) to the neighborhood of  $\theta = \theta_{\text{MAX}}$ , or from  $-5$  mrad out to  $-30$  mrad. The expanded Mie scattering fringe amplitude near  $\theta = \theta_{\text{MAX}} = \theta_o - 18$  mrad and its banding between  $-19$  and  $-25$  mrad reflects significant interference of the degree  $j=2$  scattered wave near its peak amplitude with itself for  $\theta < \theta_{\text{MAX}}$  [see Fig. 3-5(b)]. This banding is the analog

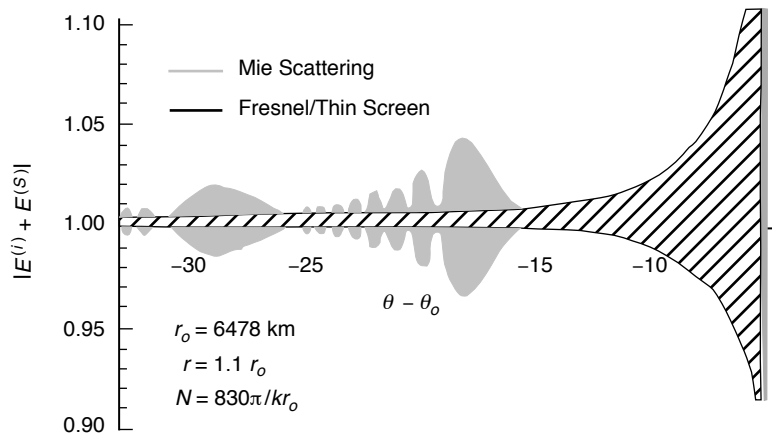


**Fig. 3-29.** Extension of the amplitude profile shown in Fig. 3-25(a) into the rainbow caustic region. Degrees  $j = 2, 3$  rainbow features occur at  $-25 \leq \theta - \theta_o \leq -15$  and  $-35 \leq \theta - \theta_o \leq -25$ , respectively. See Fig. 3-28 for the  $j = 2$  wave.

of the supernumerary arcs in rainbows. The degree  $j = 3$  scattered wave, which peaks at 0.007, becomes visible near  $\theta - \theta_o = -29$  mrad. The noise in these figures due to computational precision is about 0.001.

In summary, except for very small discontinuities in refractivity, one should account for rainbow effects at least in the neighborhoods of their maximum amplitude. With very precise and clean data, it may be possible to see  $j = 2$  rainbow effects below a super-refracting marine layer. The thin-screen model will not show these effects without further tinkering with the thin-screen phase profile per the suggestion outlined earlier in Footnote 2. On the other hand, in the vicinity of shadow zones and first contact with the caustic associated with the aggregate scattering, rainbow effects tend to be rather feeble, at least for the limited range of discontinuities in refractivity that has been considered here. For boundary layer studies, shadow zones, caustics, and the concomitant multipath effects in those regions will be the primary features of interest; rainbows should play a minor role, especially with softer discontinuities. However, for refractivity discontinuities 4 to 5 orders of magnitude larger than those considered here, for example, a raindrop, Eq. (3.16-12) shows that the peak amplitudes of these rainbow features will be 2 to 3 orders of magnitude larger. They will beam like searchlights at their peaks.

### 3.17 Limiting Cases

#### 3.17.1 The Perfectly Reflecting Sphere

When  $N \rightarrow \infty$ , considerable simplification in the scattering coefficients results. In this case, the distinction between the “electric” and “magnetic” coefficients is maintained; but, we see from Eq. (3.5-11) that the only non-zero scattering coefficients are those for the zeroth-degree scattered waves,  ${}^e b_l^{(0)}$  and  ${}^m b_l^{(0)}$ , which are the scattering coefficients for the external reflected wave. The electric coefficients reduce to

$$\left. \begin{aligned} {}^e b_l^{(0)} &= -\frac{1}{2} i^{l-1} \frac{2l+1}{l(l+1)} \left( 1 + \frac{\xi_l'^-}{\xi_l'^+} \right) \rightarrow -\frac{1}{2} i^{l-1} \frac{2l+1}{l(l+1)} \left( 1 + \frac{\text{Ai}'[y] + i \text{Bi}'[y]}{\text{Ai}'[y] - i \text{Bi}'[y]} \right) \\ y &= \nu^{2/3} \zeta[\nu/x_o], \quad \nu = l + 1/2 \end{aligned} \right\} \quad (3.17-1)$$

where  $y$  and  $\zeta[\nu/x_o]$  are defined in Eqs. (3.8-3) and (3.8-4). The magnetic coefficients reduce to

$${}^m b_l^{(0)} = -i^{l-1} \frac{2l+1}{l(l+1)} \left( \frac{\text{Ai}[y]}{\text{Ai}[y] - i \text{Bi}[y]} \right) \quad (3.17-2)$$

However, it can easily be shown from Eq. (3.2-2) that the contributions from the magnetic coefficients to the scattered wave arise only in the  $E_\theta^{(s)}$  component where they are multiplied by the factor  $P_l^1(\cos\theta)$ ; on the other hand, the electric coefficients are multiplied by  $dP_l^1/d\theta$ . Because  $P_l^1/P_l^1 \sim x_o$  for  $\nu$  in the vicinity of  $x_o$ , the relative contribution from the magnetic coefficients is diminished by  $O[x_o^{-1}]$  compared to the contribution from the electric coefficient. So, for in-plane observations, we ignore the magnetic case and drop the superscript “e” on the electric scattering coefficients.

The problem of computing the diffraction from a reflecting sphere was first worked in its entirety by G. N. Watson [3] using the Sommerfeld–Watson summation technique discussed earlier, which uses the poles of  $(\text{Ai}'[y] - i \text{Bi}'[y])$  in the upper complex plane to evaluate the scattering series.

Here we look at the problem from a stationary-phase point of view. Now  $[(\text{Ai}'[y] + i \text{Bi}'[y]) / (\text{Ai}'[y] - i \text{Bi}'[y])] = 1$  for all real values of  $y$ . It follows from Eq. (3.9-3) that the phase  $\Omega^{(0)}$  for the zeroth-degree scattered wave is given by

$$\left. \begin{aligned} b_l^{(0)} &= \frac{1}{2} i^{l-1} \frac{2l+1}{l(l+1)} \left( e^{i2\Omega^{(0)}} - 1 \right), \\ \Omega^{(0)}(y) &= \tan^{-1} \left( \frac{\text{Bi}'[y]}{\text{Ai}'[y]} \right) + \frac{\pi}{2} \end{aligned} \right\} \quad (3.17-3)$$

The phase in Eq. (3.13-5) for the total field,  $\Psi^{(0)} = 2\Omega^{(0)} + \Phi^-$ , can be written in the form

$$\Psi^{(0)} = 2\Omega^{(0)} + D_\nu + \nu(\theta_\nu - \theta) \quad (3.17-4)$$

Setting  $\partial\Psi^{(0)} / \partial\nu = 0$  to obtain the stationary-phase points in  $\nu$  yields

$$\left. \begin{aligned} 2 \frac{\partial\Omega^{(0)}}{\partial\nu} + \frac{\partial\Phi^-}{\partial\nu} &\doteq \frac{-2y}{\pi M^2[y]} \frac{\partial y}{\partial\nu} + \theta_\nu - \theta = 0 \\ M^2[y] &= \text{Ai}'^2[y] + \text{Bi}'^2[y] \end{aligned} \right\} \quad (3.17-5)$$

When  $\nu^* \ll x_o - 2K_{x_o}$ , we can use the asymptotic forms for the Airy functions. Here the stationary-phase condition in Eq. (3.17-5) can be rewritten in alternate forms. From Eqs. (3.8-3) through (3.8-5), we have for this condition

$$\begin{aligned} \left(2 \frac{\partial \Omega^{(0)}}{\partial \nu} + \frac{\partial \Phi^-}{\partial \nu}\right)_{\nu^*} &\doteq \left(-2 \frac{\partial}{\partial \nu} \left(\frac{2}{3}(-y)^{3/2}\right) + \theta_{\nu} - \theta\right)_{\nu^*} \\ &= -2 \cos^{-1}(\nu^* / x_o) + \theta_{\nu^*} - \theta = 0, \quad \nu^* < x_o - 2K_{x_o} \end{aligned} \quad (3.17-6a)$$

or

$$y^* \doteq -\frac{1}{4} K_{x_o}^2 (\theta - \theta_{\nu^*})^2 \quad (3.17-6b)$$

Noting that  $|\nu^* - x_o|/x_o \ll 1$ , we can expand these expressions about  $\nu^* = x_o$  to obtain

$$\nu^* = x_o \left(1 - \frac{1}{8} (\theta - \theta_o)^2\right) \left(1 + O[(\theta - \theta_o)^2]\right) \quad (3.17-7a)$$

or

$$y^* \doteq -\frac{1}{4} \left(K_{x_o}^2 (\theta - \theta_o)^2\right) \left(1 + O[\theta - \theta_o]\right) \quad (3.17-7b)$$

It follows from Eq. (3.17-6b) for the perfectly reflecting sphere that diffraction effects as a function of angular position  $\theta - \theta_o$  of the LEO relative to the geometric shadow boundary scale as  $K_{x_o}^{-1}$ . Providing that  $x_o$  is sufficiently large so that the Airy function asymptotic forms for the Hankel functions are valid, we need only solve the scattering integrals once and then scale the result by  $K_{x_o}^{-1}$  in both amplitude and in the angular coordinate to obtain results for an arbitrary ratio  $r_o / \lambda$ .

Figure 3-30 shows  $2\partial\Omega^{(0)}/\partial y$  in the vicinity of  $y=0$ . It has a global minimum of  $-0.964$  at  $y=+0.630$ . Stationary-phase points occur at the intersections of the  $2\partial\Omega^{(0)}/\partial y$  curve with the curve  $\partial\Phi^-/\partial y \doteq K_{x_o}(\theta - \theta_o) = \text{constant}$ . For  $-0.964 \text{ rad} \leq K_{x_o}(\theta - \theta_o) < 0$ , two stationary-phase points exist, which will result in pronounced interference effects. For the scaling applicable here,  $K_{x_o} \approx 475$ ; therefore, the range of  $(\theta - \theta_o)$  values over which interference occurs is only a few milliradians; the elapsed time would be a few seconds. We see that these effects will attenuate rapidly for  $K_{x_o}(\theta - \theta_o) < -0.964 \text{ rad}$ . For  $\theta - \theta_o > 0$ , only one stationary-phase point exists but diffraction effects will persist for awhile as a result of the interference between the convolution integrals involving the phasors  $\exp(i\Psi^{(0)})$  and  $\exp(i\Phi^-)$ . A caustic occurs at  $K_{x_o}(\theta - \theta_o) = -0.964 \text{ rad}$ .

Figure 3-31 shows the variation of  $\Psi^{(0)}$  with  $y$  parametrically in  $(\theta - \theta_o)$ . We can evaluate the scattering integrals in Eq. (3.13-5) for the extreme cases:  $\theta - \theta_o \gg 0$  and  $\theta - \theta_o \ll 0$ . In the latter case, the LEO is well into the shadow of the reflecting sphere and so the expressions for the scattered wave after the transition through the shadow boundary should approach the negative of the expression for incident plane wave. Figure 3-30 shows that no stationary-phase points exist for  $\theta - \theta_o < -964K_{x_o}^{-1}$  mrad and that the phase rate in the phasor

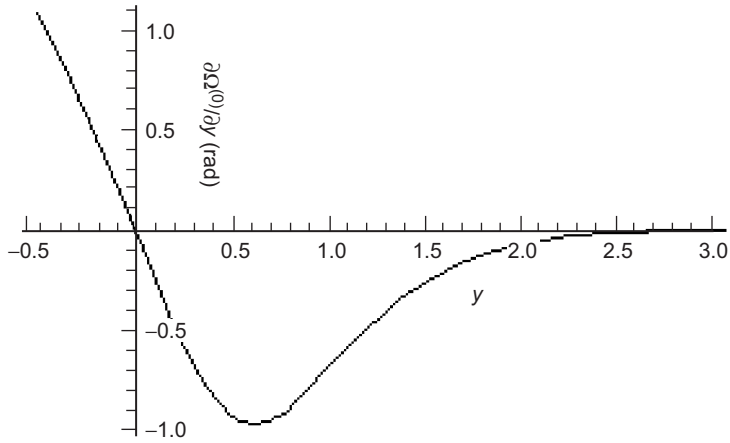


Fig. 3-30. Stationary points for the phase delay  $\Psi^{(0)}$  for the reflected wave are defined by the intersections of the  $2\partial\Omega^{(0)}/\partial y$  curve with a near-horizontal line (not shown); the latter is given by  $\partial\Omega/\partial y \doteq K_{x_o}(\theta - \theta_o) = \text{constant}$ .

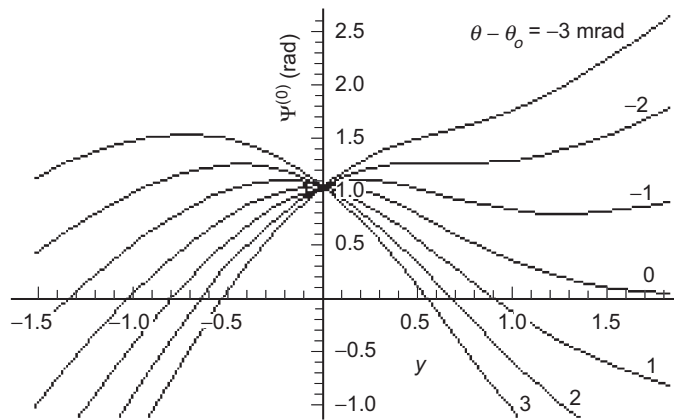


Fig. 3-31. Variation of  $\Psi^{(0)}$  with spectral number.

$\exp(i\Psi^{(0)})$  increases rapidly with decreasing  $\theta - \theta_o$  below this threshold. Thus, we expect negligible contribution from the  $I$  integrals in Eq. (3.13-7) for  $\theta - \theta_o$  in this region; the main contribution comes from  $J$  integrals in Eq. (3.13-8), which involve simple Fresnel integrals that are easily shown to approach the negative of the expression for the incident wave.

For  $(\theta - \theta_o) > 0$ , the scattering results from near-grazing reflection of the incident wave from the sphere, and we will see that the scattering intensity increases as  $\theta - \theta_o$  increases, that is, as the stationary point in  $y$ -space (see Fig. 3-31) becomes more negative. For this regime, the  $J$  integrals will contribute negligibly to the scattering (that is, scattering from a knife-edge is negligible for altitudes well above the altitude of the edge); we are concerned only with the  $I$  integrals for this limiting case. From Eq. (3.13-7), we have

$$\begin{aligned} \begin{Bmatrix} I_r \\ I_\theta \end{Bmatrix} &\doteq E_o \sqrt{\frac{1}{2\pi i x \sin \theta}} \left[ \int_{-\infty}^{x_o} \left\{ \frac{(\sin^2 \theta_v \tan \theta_v)^{1/2}}{(\sin \theta_v \cos \theta_v)^{1/2}} \right\} e^{i\Psi^{(0)}} dv \right. \\ &\quad \left. + \int_{x_o}^{\infty} \left\{ \frac{(\sin^2 \theta_v \tan \theta_v)^{1/2}}{(\sin \theta_v \cos \theta_v)^{1/2}} \right\} (e^{i\Psi^{(0)}} - e^{i\Phi^-}) dv \right] \end{aligned} \quad (3.17-8)$$

We note that the phasor in the second integral may be written as  $(\exp(i2\Omega^{(0)}) - 1)\exp(i\Phi^-)$ , which decays to zero rapidly for  $v > x_o$ . We have already shown in Eqs. (3.17-6) and (3.17-7) for  $(\theta - \theta_o) > 0$  that the stationary-phase point in spectral number is located at  $v^* < x_o$ . Therefore, only the upper integral in Eq. (3.17-8) contributes significantly to the calculation of  $I$  for  $\theta$  well above the shadow boundary.

To evaluate this upper integral using the stationary-phase technique, we expand  $\Psi^{(0)} = 2\Omega^{(0)} + \Phi^-$  about  $v^*$  to obtain

$$\begin{aligned} \Psi^{(0)} &\doteq \Psi_{v^*}^{(0)} + \frac{1}{2} \left( \frac{\partial^2 \Psi^{(0)}}{\partial v^2} \right)_{v^*} (v - v^*)^2 \\ &= \Psi_{v^*}^{(0)} + \frac{1}{2} \left( -\frac{2}{(x_o^2 - v^{*2})^{1/2}} - \frac{1}{(x^2 - v^{*2})^{1/2}} \right) (v - v^*)^2 \quad (3.17-9) \\ &\doteq \Psi_{v^*}^{(0)} - \frac{2}{x_o(\theta - \theta_o)} (v - v^*)^2 \end{aligned}$$

Here the last line is obtained from Eq. (3.17-7a), noting that  $(x_o^2 - v^{*2})^{-1/2} \gg (x^2 - v^{*2})^{-1/2}$  for near-grazing reflections with  $(\theta - \theta_o) > 0$ . The upper integral in Eq. (3.17-8) becomes

$$\left. \begin{aligned} \left\{ \begin{array}{l} I_\theta \\ I_r \end{array} \right\} &= \frac{E_o}{2} e^{i\Psi_{v^*}^{(0)}} \sqrt{(\theta - \theta_o) \tan \theta_o} \left\{ \begin{array}{l} \cos \theta \\ \sin \theta \end{array} \right\} \frac{1}{1+i} \int_{-\infty}^w e^{-i\frac{\pi}{2} w'^2} dw', \\ w &= \sqrt{K_{x_o}^3 \frac{(\theta - \theta_o)^3}{8\pi}}, \quad \Psi_{v^*}^{(0)} = (2\Omega^{(0)} + D_v + v(\theta_v - \theta))_{v=v^*} \end{aligned} \right\} \quad (3.17-10)$$

Figure 3-32 shows the amplitude of the scattered wave versus  $(\theta - \theta_o)$  from a perfectly reflecting sphere; a numerical integration of Eqs. (3.13-7) and (3.13-8) was used. Figure 3-33 is the amplitude of the scattering from a knife-edge pattern, that is,  $\sqrt{J_r^2 + J_\theta^2}$  from Eq. (3.13-8). Figure 3-34 shows the amplitude of the difference between the scattering from the sphere and from a knife-edge, that is, the amplitude  $\sqrt{I_r^2 + I_\theta^2}$  from Eq. (3.17-8). For  $\theta - \theta_o > 0$ , the Fresnel modulation is evident in Fig. 3-34 as a result of interference between wavelets with  $v$  values above and below  $v^*$ . The incomplete Fresnel integral in Eq. (3.17-10) provides this modulation. Also, the secular dependence

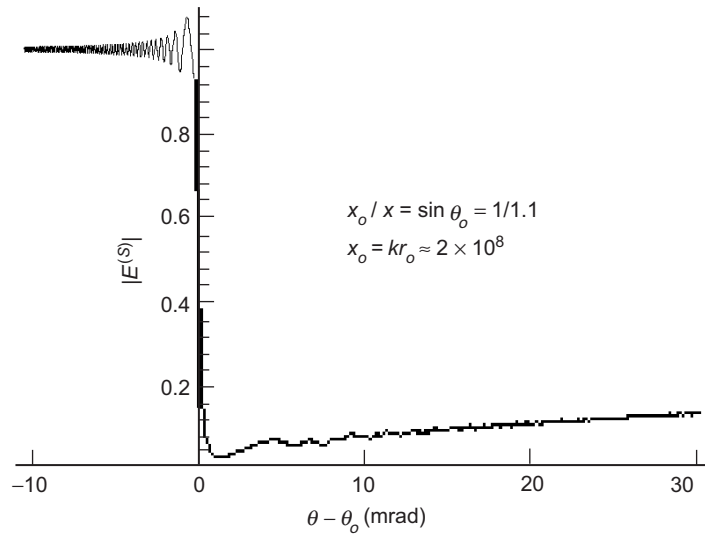


Fig. 3-32. Amplitude of the total scattering by a perfectly reflecting sphere.

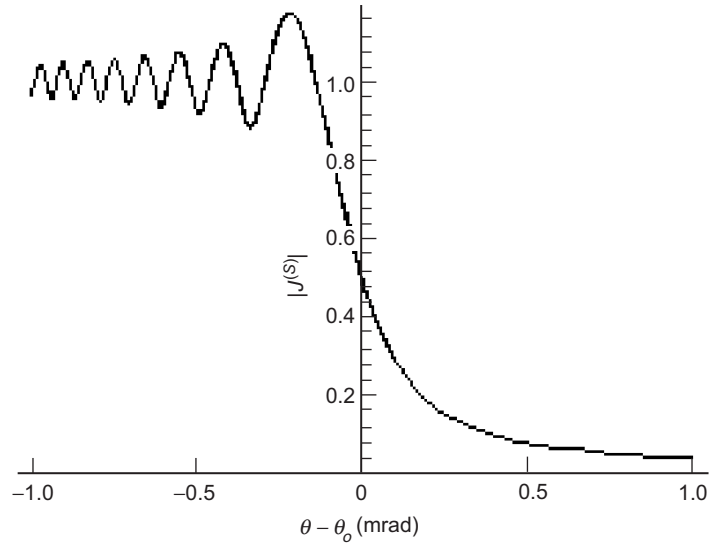


Fig. 3-33. Knife-edge component of scattering from a perfectly reflecting sphere. The same conditions as used in Fig. 3-32.

of the amplitude of the scattering on  $\sqrt{(\theta - \theta_o) \tan \theta_o} / 2$ , which is predicted by Eq. (3.17-10), is clearly evident in this figure when  $\theta - \theta_o > 0$ , indicative of a near-grazing reflection from the surface of the sphere. We see from these figures that the diffraction from a shiny sphere is accurately represented by the knife-edge diffraction pattern for  $(\theta - \theta_o) < 0$ . Even for  $\theta - \theta_o > 0$ , where near-grazing reflections occur, the knife-edge approximation is good to better than 10 percent for  $K_{x_o} (\theta - \theta_o) < 10$ , or in our case for a LEO located at less than  $\sim 60$  km, above the shadow boundary, or, equivalently, within about 20 to 30 s of elapsed time. We should expect better agreement for an opaque sphere, which should damp the scattering for  $\theta - \theta_o > 0$ , except at near grazing conditions.

### 3.17.2 Geometric Optics Interpretation

The stationary-phase condition for  $y^*$  in Eq. (3.17-9) has a geometric optics interpretation in terms of the angle of incidence of the ray at the subreflection on the sphere. Referring to Fig. 3-14, let us define a new angular measure:

$$\theta_v^o = \sin^{-1}(v / x_o) \quad (3.17-11)$$

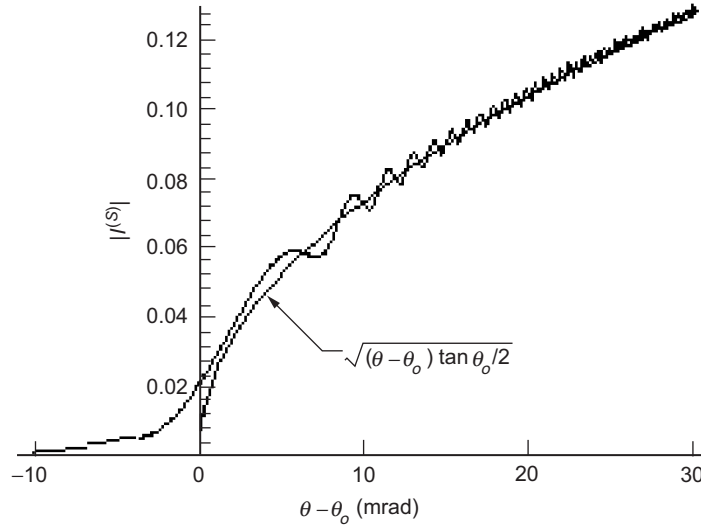
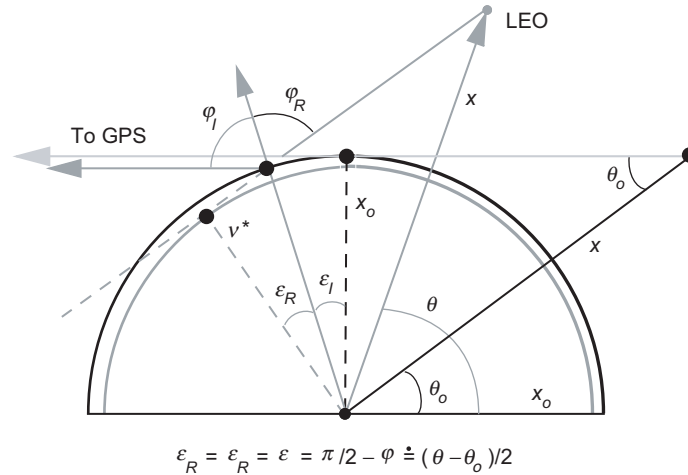


Fig. 3-34. Amplitude of the vector difference between scattering from a perfectly reflecting sphere and from a knife-edge. The same conditions as used in Fig. 3-32.

Hence  $\sin \theta_v = v/x = \sin \theta_o \sin \theta_v^o$ ;  $\theta_v^o$  provides a measure of the spherical surface of radius  $v$  relative to the reflecting sphere of radius  $x_o$ . When  $(\theta - \theta_o) \gg 2K_{x_o}^{-1} \approx 0.004$ , so that  $\Psi^{(0)} \rightarrow \pi/2 - 4(-y)^{3/2}/3 + \Phi^-$  with good accuracy, it follows from Eqs. (3.8-3) and (3.8-4) that the stationary-phase condition  $\partial \Psi^{(0)} / \partial v = 0$  given in Eq. (3.17-6a) is achieved when  $v$  assumes a value  $v^*$ , which satisfies the expression

$$\left. \begin{aligned} 2\theta_{v^*}^o + \theta - \theta_{v^*} &= \pi \\ \text{or} \\ \sin(2\theta_{v^*}^o + \theta) &= -\sin \theta_o \sin \theta_{v^*}^o \end{aligned} \right\} \quad (3.17-12)$$

However, referring to the geometry shown by Fig. 3-35, the ray from the GPS satellite that reflects from the surface of the sphere of radius  $x_o$  and continues to the LEO makes an angle of incidence  $\varphi_I$  with the normal to the sphere and reflects at an angle  $\varphi_R$ . When  $\varphi_I = \varphi_R = \varphi$  and we replace  $\theta_v^o$  with  $\varphi$  in Eq. (3.17-12), we see from the geometry that this same condition holds for  $\varphi$ ; hence,  $\theta_{v^*}^o = \varphi = \pi/2 - (\theta - \theta_o)/2 + O[(\theta - \theta_o)^2]$ . For the LEO located at an angular distance  $(\theta - \theta_o)$  above the shadow boundary of the sphere, the ray from the tangent point on the caustic spherical surface of radius  $v^* = x_o \sin \theta_{v^*}^o$



**Fig. 3-35. Stationary phase geometry and the law of reflection.** When the spectral number  $\nu = \nu^*$  in wave theory,  $\varphi_I = \varphi_R$  in geometric optics.

continues along a straight line to the LEO at a slope angle of  $\pi - 2\varphi$  with respect to the LEO–GPS line. It intersects the reflecting sphere of radius  $x_0$  and makes an angle  $\varphi$  with respect to the radius vector; hence, this value  $\nu^*$ , which provides a stationary value for  $\Psi^{(0)}$ , also yields the ray in geometric optics that satisfies the law of reflection  $\varphi_I = \varphi_R$ . The location  $\tilde{\theta}$  of this new tangent point on the sphere of radius  $\nu^*$  is given by  $\tilde{\theta} \doteq \pi/2 + (\theta - \theta_0) + \tan \theta_0 (\theta - \theta_0)^2 / 8$ .

**3.17.3 Limiting Cases: The Strongly Absorbing Sphere**

In the case of a strongly absorbing sphere, the index of refraction  $\hat{n}$  for the sphere contains an imaginary component giving rise to an extinction coefficient for waves penetrating its boundary [8]. We write this in the form  $\hat{n} = n(1 + i\kappa)$ , where  $n$  is the real component and  $n\kappa$  is the imaginary component, and where  $\kappa$  is called the extinction coefficient and is real. Because  $x_0 \gg 1$ , the slightest hint of an extinction coefficient will result in the penetrating waves being completely damped before escaping from the sphere. It is easily shown from Maxwell’s equations that the energy density of a penetrating wave falls to  $1/e$  of its incident value after having traveled a distance  $d = 1/2k\kappa n$  in a medium with a complex index of refraction  $\hat{n}$ . We want this distance to be much smaller than the radius of the sphere  $d \ll r_0$ . This inequality implies that  $\kappa n \gg 1/2x_0$ , which is exceedingly small, and in this case the penetrating waves essentially are completely absorbed within the sphere for virtually all incident angles except very close to grazing. More precisely, to attain a “sharp” edge for the

limb of the sphere, we will want the distance  $d$  to be much less than the chord length of a sphere of radius  $r_o$  transected by the incident ray with an impact distance that is some specified small fraction of the first Fresnel zone; therefore, we want  $\kappa \gg x_o^{-3/4} / 5 \sim 10^{-7}$ . On the other hand, we want the sphere to reflect as little as possible if it is to emulate a knife-edge; therefore,  $|\hat{n}|$  should be very close to unity in order to minimize reflection from the surface of the sphere at near-grazing angles of incidence. We may again take guidance from the Fresnel formulas in Eq. (3.4-1) and the reflection and transmission ratios shown in Fig. 3-4, where in this case the transmitted angle  $\varphi'$  will be complex, which gives rise to phase shifts in the reflected and transmitted waves. To avoid "glint" from near-grazing incident angles (that is, to optimize the agreement with the knife-edge results), we wish to keep  $\kappa$  as small as possible. We must do this consistent with maintaining essentially total absorption of the penetrating waves except within a very narrow range of impact parameter values that is a small fraction of the first Fresnel zone. We will see that there is a broad range for  $\kappa$  over which the diffraction results are nearly invariant and could be said to correspond to an "opaque" sphere.

The boundary conditions that have been applied to obtain the scattering coefficients in Eq. (3.5-11) are still valid for a complex index of refraction, but the arguments of the spherical Hankel functions  $\xi_l^\pm(nx_o)$  are now complex and, therefore, involve in part the modified Bessel functions. The asymptotic forms for the Airy functions also hold in the complex plane, but certain restrictions apply to the argument of their complex variable  $\hat{y}$  [see in Eq. (3.8-7)]. From Eq. (3.13-21), we have  $\hat{y}(v) \doteq (2/\hat{n}x_o)^{2/3}(v - \hat{n}x_o)$ ; whenever  $n\kappa$  is sufficiently large so that  $\text{Im}[\hat{y}(x_o)] \doteq -2\kappa(x_o/2)^{2/3} \ll -2$ , the Airy functions  $\text{Ai}[\hat{y}]$  and  $\text{Bi}[\hat{y}]$  assume their respective asymptotic exponential forms to good accuracy even when  $v = x_o$ ; it is easily shown in this case that when  $\kappa \gg (x_o/2)^{-2/3} \approx 4 \times 10^{-6}$ ,  $\xi_l^+(\hat{n}x_o) \rightarrow 0$ ,  $\xi_l^-(\hat{n}x_o) \rightarrow \infty$ . However, the ratio  $(\xi_l^-(\hat{n}x_o)/\xi_l^+(\hat{n}x_o))$  is still finite and well-behaved, and is obtained from Eq. (3.8-10) when  $\kappa n \gg (2/x_o)^{2/3}$  and  $v \sim x_o$ .

From Eq. (3.5-11), we see that the only surviving scattering coefficients when  $\kappa n \gg (2/x_o)^{2/3}$  are  $b_l^{(0)}$ . From Eq. (3.9-3), these coefficients are given by

$$b_l^{(0)} = \frac{1}{2} i^{l-1} \frac{2l+1}{l(l+1)} \left( \rho^{(0)} \exp(i2\Omega^{(0)} - 1) \right) \quad (3.17-13)$$

where  $\rho^{(0)}$  and  $2\Omega^{(0)}$  are given by Eq. (3.9-5).

From Eq. (3.9-5), we have the asymptotic form for  $2\Omega^{(0)}$ , and it follows that  $2\Omega^{(0)} \rightarrow \pi/2 - 4(-y(\nu))^{3/2}/3$  for  $\nu < x_o$ , just as it does for the perfectly reflecting case. Here,  $y$  is real; the relationship between  $y$  and  $\hat{y}$  when  $n = 1$  and  $\kappa \ll 1$  is given by  $\hat{y} \doteq y - 2i\kappa(x_o/2)^{2/3}$ . Therefore, the variation of  $\Psi^{(0)}$  with  $y$  is very similar to that shown in Fig. 3-31 for the perfectly reflecting case, and in particular, when  $\theta - \theta_o > 0$ ,  $\Psi^{(0)}$  will have one stationary value, which is located in  $y$ -space at  $y^*$ , which in its asymptotic form is given by Eq. (3.17-8). However, unlike the case of the perfectly reflecting sphere where  $|\rho^{(0)}(y)| \equiv 1$ , in this case the modulus, which is the Mie analog of the Fresnel formula for the reflection coefficient, is a strong function of  $y$  and given by

$$|\rho^{(0)}(y)| \rightarrow \left\{ \begin{array}{l} \left| \frac{(2i\kappa K_{x_o}^2 - y)^{1/2} - (-y)^{1/2}}{(2i\kappa K_{x_o}^2 - y)^{1/2} + (-y)^{1/2}} \right|, y < 0 \\ 1, y > 0 \end{array} \right\} \quad (3.17-14)$$

$$\hat{n} = 1 + i\kappa, \kappa \ll 1, K_{x_o} = \left(\frac{x_o}{2}\right)^{1/3}$$

Figure 3-36 shows the behavior of  $|\rho^{(0)}(y)|$  parametrically with different values of  $\kappa$ . For good absorption characteristics, we want  $|\rho^{(0)}(y^*)| \approx 0$  whenever  $\theta - \theta_o > 0$ . This can be achieved by making  $\kappa$  sufficiently small so that  $|\rho^{(0)}(y)|$  assumes a “Heaviside” functional form with a transition at  $y = 0$ , but not too small so that the sphere becomes partially transparent at near-grazing incidence angles. We see from Fig. 3-32 that this form is approached for  $\kappa < (2/x_o)^{2/3} \sim 10^{-6}$ .

Figure 3-37 shows the amplitude of the  $I$  integrals based on numerical integrations of Eq. (3.13-7); it shows the amplitude of  $I$  versus  $\theta - \theta_o$  for different extinction coefficients. For the larger extinction coefficient, we would expect stronger scattering (and deeper interference) fringes for  $\theta - \theta_o > 0$  and weaker scattering for  $\theta - \theta_o < 0$ .

For  $\theta - \theta_o > 0$ , the fringes in Fig. 3-37 can be largely recovered from the corresponding curve for the perfectly reflecting case (see Fig. 3-34) merely by multiplying the amplitudes for this case by  $\rho^{(0)}(y^*[\theta - \theta_o])$ . Figure 3-37 shows the amplitude of the vector difference between scattering from a strongly absorbing sphere and from a knife-edge; the difference is very slight for this

range of extinction values. For the scattering effects from an absorbing sphere, it is this close agreement between Mie scattering theory and scalar diffraction theory applied to a knife-edge that justifies the use of the latter to take advantage of its far simpler computational burden.

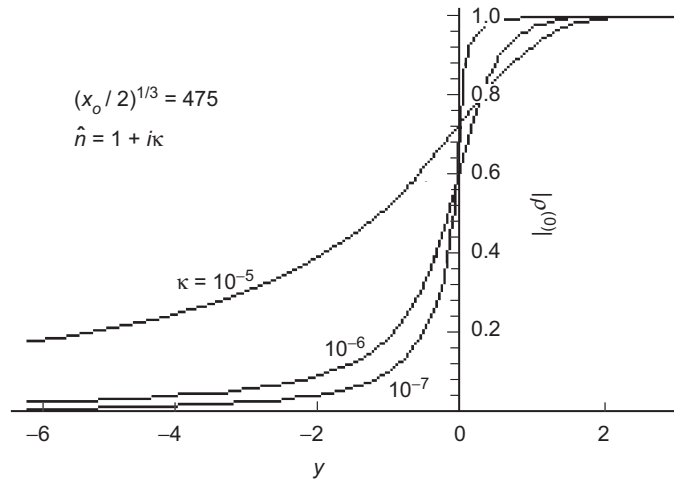


Fig. 3-36. Mie "reflection" coefficient for different extinction coefficients.

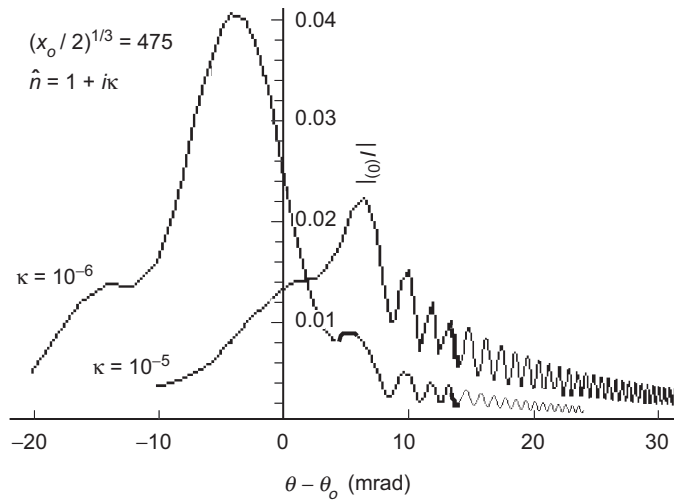


Fig. 3-37. Amplitude of the vector difference between the scattering from an opaque sphere with extinction coefficient  $\kappa$  and from a knife-edge.

### 3.17.4 Limiting Cases: Reflections from a Sphere of Infinite Radius

As the radius of the refracting sphere grows arbitrarily large relative to the wavelength of the incident wave, one can show that the stationary-phase conditions on the spectral number for the scattering series approach a simpler limiting form [16]. These become the Fresnel formulas for an infinite plane plus a phase offset to account for the location of the LEO.

### References

- [1] G. Mie, "Beiträge zur Optik Trüber Medien Speziell Kolloidaler Metallösungen," *Annalen der Physik*, vol. 25, pp. 377–445, 1908.
- [2] P. Debye, "Der Lichtdruck auf Kugeln von Beliebigen Material," *Annalen der Physik*, vol. 30, pp. 57–136, 1909.
- [3] G. Watson, "The Diffraction of Electric Waves by the Earth," *Proceedings of the Royal Society*, vol. A95, pp. 83–99, London, United Kingdom, 1918.
- [4] B. Van der Pol and H. Bremmer, "The Diffraction of Electro-Magnetic Waves from an Electric Point Source Round a Finitely Conducting Sphere, with Applications to Radiotelegraphy and the Theory of the Rainbow, Part II," *Philosophical Magazine*, vol. 24, no. 164, *Supplement*, pp. 825–864, 1937.
- [5] H. Buerieus, "Theorie des Regenbogens und der Glorie," *Optik*, vol. 1, pp. 188–212, 1946.
- [6] J. Stratton, *Electromagnetic Theory*, New York: McGraw-Hill, 1941.
- [7] J. Jackson, *Classical Electrodynamics*, 2nd ed., New York: John Wiley & Sons, Inc., 1975.
- [8] M. Born and E. Wolf, *Principles of Optics*, 6th ed., Oxford, United Kingdom: Pergamon Press, 1980.
- [9] G. Watson, *A Treatise on the Theory of Bessel Functions*, 2nd ed., Cambridge, United Kingdom: Cambridge University Press, 1944.
- [10] M. Abramowitz and I. Stegun, eds., *Handbook of Mathematical Functions With Formulas, Graphs, and Mathematical Tables*, National Bureau of Standards Series 55, Washington, DC, 1964.
- [11] J. Mathews and R. Walker, *Mathematical Methods of Physics*, Menlo Park, California: Benjamin/Cummings Publishing Co., 1970.
- [12] A. Sommerfeld, *Partial Differential Equations in Physics*, New York: Academic Press, 1967.
- [13] H. Bremmer, *Terrestrial Radio Waves*, Amsterdam: Elsevier Publishing Co., 1949.

- [14] J. Keller, “Geometric Theory of Diffraction,” *The Journal of the Optical Society of America*, vol. 52, no. 2, pp. 116–130, 1962.
- [15] A. Sommerfeld, “Mathematische Theorie der Diffraction,” *Math. Ann.* vol. 47, S319, pp. 317–374, 1896.
- [16] J. Melbourne, *Sensing Atmospheric and Ionospheric Boundaries in GPS Radio Occultation Observations From a Low Earth Orbiter, Part 2*, JPL Publication 99-5, Jet Propulsion Laboratory, Pasadena, California, April 1999.